Naval Research Laboratory
Washington, DC 20375-5320

NRL/6130/MR—2021/9

Plasmon-Induced Chemical Bond Cleavage by Refractory Transition Metal Nitrides

OLGA A. BATURINA

Corrosion Science Section
Chemistry Division

ALBERT EPSHTEYN

ANDREW PURDY

Materials Synthesis and Processing Section
Chemistry Division

SPENCER GILES

Applied Concepts in Materials Section
Chemistry Division

BLAKE SIMPKINS

Nanomaterials, Interfaces, and Devices Section
Chemistry Division

December 3, 2021

REPORT DOCUMENTATION PAGE

Form Approved
OMB No. 0704-0188

1. REPORT DATE *(DD-MM-YYYY)*	**2. REPORT TYPE**	**3. DATES COVERED** *(From - To)*
03-12-2021	NRL Memorandum Report	10-01-2016 – 10-01-2021

4. TITLE AND SUBTITLE

Plasmon-Induced Chemical Bond Cleavage by Refractory Transition Metal Nitrides

5a. CONTRACT NUMBER

5b. GRANT NUMBER

5c. PROGRAM ELEMENT NUMBER
61153N

6. AUTHOR(S)

Olga A. Baturina, Albert Epshteyn, Spencer Giles, Andrew Purdy, and Blake Simpkins

5d. PROJECT NUMBER

5e. TASK NUMBER

5f. WORK UNIT NUMBER
1G40

7. PERFORMING ORGANIZATION NAME(S) AND ADDRESS(ES)

Naval Research Laboratory
4555 Overlook Avenue, SW
Washington, DC 20375-5320

8. PERFORMING ORGANIZATION REPORT NUMBER

NRL/6130/MR--2021/9

9. SPONSORING / MONITORING AGENCY NAME(S) AND ADDRESS(ES)

Naval Research Laboratory
4555 Overlook Avenue, SW
Washington, DC 20375-532

10. SPONSOR / MONITOR'S ACRONYM(S)

NRL Base Program

11. SPONSOR / MONITOR'S REPORT NUMBER(S)

12. DISTRIBUTION / AVAILABILITY STATEMENT

DISTRIBUTION STATEMENT A: Approved for public release; distribution is unlimited.

13. SUPPLEMENTARY NOTES

14. ABSTRACT

This report presents research conducted by NRL Chemistry Division on plasmon-mediated photocatalysis by refractory transition metal nitrides (RTMNs). RTMN materials are synthesized, characterized by a variety of physico-chemical methods and utilized for evaluation of their photocatalytic activity in two reactions: (1) methanol photoelectrochemical oxidation at the electrode/solution interface and (2) oxidation of 2-chloro ethyl sulfide at the photocatalyst/air interface. The mechanisms of promotions are proposed.

15. SUBJECT TERMS

Refractory transition metal nitride
Localized surface plasmon resonance
Photocatalytic activity
Methanol photoelectrochemical oxidation
2-chloro ethyl ethyl sulfide

16. SECURITY CLASSIFICATION OF:			**17. LIMITATION OF ABSTRACT**	**18. NUMBER OF PAGES**	**19a. NAME OF RESPONSIBLE PERSON**
					Olga Baturina
a. REPORT	**b. ABSTRACT**	**c. THIS PAGE**	U	58	**19b. TELEPHONE NUMBER** *(include area code)*
U	U	U			(202) 767-6345

This page intentionally left blank.

CONTENTS

This page intentionally left blank.

EXECUTIVE SUMMARY

This report presents research conducted by the NRL Chemistry Division on plasmon-mediated photocatalysis by refractory transition metal nitrides (RTMNs). Plasmonic photocatalysis is promising way to harvest energy of visible light and drive chemical reactions on the surface of photocatalysts. The interaction of plasmonic nanostructures with light at certain frequencies leads to the generation of hot electrons that can directly or indirectly break chemical bonds on the surface of the photocatalysts. The current state-of-the-art material used in the majority of plasmonic systems, and in particular in photocatalysis is gold, typically supported on a semiconductor support. Although gold is one of the best plasmonic materials, its real-life application is hindered by its high cost. RTMNs represent an attractive low-cost alternative to gold (Au). Because of large concentrations of free carriers in some of these materials ($\sim 10^{22}$ cm^{-3}), they establish metallic optical properties which support localized surface plasmon resonances (LSPRs) in the visible and near-infrared (IR) regions. Unlike Au, the optical properties of RTMN can be tuned by changing their processing conditions and composition thus making them more versatile than metals in terms of system design. Furthermore, the high-temperature stability of RTMN materials suit them well for catalytic processes, which are often carried out at higher temperatures due to reaction acceleration. While the photocatalytic activity of Au/TiO_2 NPs has been demonstrated before, very little work exists on plasmon-induced photocatalytic reactions by RTMN nanoparticles. The objective of this program was (1) to demonstrate that gold nanoparticles can be replaced by low-cost groups IV-VI refractory RTMN nanoparticles that possess similar plasmonic, but different catalytic, adsorptive and structural properties and (2) elucidate the mechanisms of photo-induced bond cleavage by RTMN-based nanoparticles for two Navy-relevant reactions: methanol (CH_3OH) oxidation and the decomposition of 2-chloroethyl ethyl sulfide (2-CEES, chemical warfare agent simulant). Our hypothesis is that for photocatalytic reactions in which the Au surface character (i.e. its chemical, adsorptive, and structural properties) is not essential, RTMN NPs can successfully replace Au NPs providing inexpensive, tunable, chemically robust plasmonic activation. For photocatalytic reactions, in which the gold surface structure is essential, the amount of gold in NPs can be minimized by implementing core-shell nanostructures. Core-shell NPs with RTMN cores and Au shells are expected to combine catalytic activity of gold with plasmonic properties of refractory metal nitride core.

Prior to utilizing RTMN nanoparticles in plasmon-mediated photocatalytic reactions, they were synthesized, characterized by a variety of physical and microscopic techniques, and compared to commercially available materials. RTMN nanoparticles were synthesized by ammonolysis of $MCl_3(THF)_3$ (M=Ti, V, Cr) and $Zr(NMe_2)_4$ precursors [1]. A novel method has been developed for growing well-dispersed TiN nanoparticles inside a non-reactive porous Al_2O_3 (TiN/Al_2O_3). In-house made TiN, VN and CrN nanoparticles exhibited weak LSPR in comparison to commercial TiN (Plasma Chem) most likely due to NPs' oxidation and agglomeration. On the contrary, in-house made ZrN nanoparticles outperformed commercial material produced by American Elements. A method has been proposed for synthesis of TiN-Au core-shell nanoparticles with an ultra-thin (monolayer or less) Au shell.

Comparison of optical response of the best performing TiN nanoparticles to that of Au showed that TiN NPs exhibited a broader red-shifted LSPR in comparison to Au which was assigned mostly to quasi-metallic character of TiN NPs. Comparison of activity of TiN/TiO_2 photocatalyst towards photocatalytic methanol oxidation to that of Au/TiO_2 demonstrated that both TiN and Au nanoparticles acted as photo-sensitizers extending TiO_2 activity into the visible spectral region. Further analysis highlighted two major differences between the TiN/TiO_2 and Au/TiO_2 photocatalysts. First, potential bias was required to initiate visible light-induced CH_3OH oxidation at the TiN/TiO_2 interface since it formed an Ohmic junction. Second, the reaction at the TiN/TiO_2 interface was most likely driven by the highly reactive holes generated by interband transitions in TiN NPs at wavelengths shorter than 630 nm, while the plasmonic effect, peaking at 580 nm was thought to be a major driving force for the CH_3OH oxidation on the Au/TiO_2 material. The differences between the effects of TiN and Au NPs were assigned to the differences in their electronic

structure, morphology, plasmonic nanoparticle/TiO_2 interface, optical properties, and electrocatalytic activity [2].

In a separate effort, we embedded commercial and in-house synthesized TiN nanoparticles into matrixes of TiO_2 and compared their ability to enhance electrochemical oxidation reactions to that of conventional Au nanoparticles. Although the photon-to-carrier conversion efficiencies were low (~10^{-4} %), the reaction rates were enhanced by a factor of 4 in the visible and near-infrared for both Au and TiN compared to a pure TiO_2 control, with TiN showing an order of magnitude improvement over Au in the near IR region. The spectral dependence of reaction rate enhancement followed the nanoparticle extinction spectra, and a linear power-dependence identifies a photo-excited carrier mechanism (i.e., decaying plasmons excite carriers that participate in chemistry rather than heating of the system). Lastly, photo-induced transients of the electrochemical signal are consistent with interfacial defect charging in these heterosystems. Consistent with our previous results, the TiN/TiO_2 system, which has no Schottky barriers, exhibited a bias-dependent and transient photoelectrochemical response, while the Au/TiO_2 system, which naturally forms a Schottky barrier that immediately separates charged carriers, exhibited a near-instantaneous response [3].

ZrN is expected to have a sharper blue-shifted LSPR response in comparison to TiN. However, ZrN NPs appear to be less chemically inert than TiN, owing to zirconium's strong affinity for oxygen. A layer of dielectric ZrO_2 readily forms on the surface of ZrN NPs even in the presence of only trace oxygen. The oxide layer has a detrimental effect on the LSPR, leading to its broadening and red-shifting. Photocatalytic activities of TiO_2-supported ZrN NPs were compared to those of TiN/TiO_2 in a series of experiments utilizing in-house made ZrN NPs. Our results indicate that optical properties and photocatalytic activity of ZrN/TiO_2 are strongly affected by ZrN surface oxidation and agglomeration. We found that under visible illumination, both in-house synthesized 17 nm ZrN and commercial 30 nm TiN NPs promote TiO_2 activity for CH_3OH oxidation, but the mechanism of enhancement appears to be different for the two nitrides. The photocurrent enhancement observed for ZrN NP is assigned to a photothermal effect, since charge transport from the NPs is expected to be drastically inhibited due to the dielectric ZrO_2 shell, while interband transitions in TiN NPs are likely the major contributor to an increase in photocurrent at the TiN/TiO_2 interface [4].

In spite of the promising plasmonic properties of TiN NPs, application of TiN/TiO_2 photocatalyst is limited to electrochemical interfaces (i.e. photocatalyst/electrolyte interface) due to the absence of Schottky barrier. In order to be utilized at the interface with air, the TiN/TiO_2 interface needs to be re-designed. Two strategies were explored in order to create a Schottky barrier: (1) modification of plasmonic TiN NPs by decorating them with the gold shell, and (2) using semiconductor with the different band alignment in comparison to TiO_2. To implement the second strategy, GaN was selected as an alternative to TiO_2. Measurements of a Schottky barrier at the interface of TiN and *n*- and *p*-type GaN films demonstarted that only *p*-type GaN formed an electronic barrier with TiN.

Unlike TiN, Au forms a Schottky barrier with TiO_2, and Au/TiO_2 photocatalyst is capable of promoting photocatalytic reactions at the photocatalyst/air interface. This material was used to determine the mechanism of the effect of visible light on photooxidation of the Navy-relevant organic molecule 2-CEES. We (in collaboration with co-authors from US Army DEVCOM CBC) demonstrated that under anaerobic conditions, 2-CEES partially desorbs from the Au/TiO_2 surface likely due to a photothermal effect, induced by photo-excited plasmonic Au nanoparticles [5].

To optimize photocatalytic activity of the semiconducting TiO_2 support, materials with different morphology have been synthesized and investigated [6, 7]. Addition of long-chain alkyl phosphonic acids to the synthesis led to formation of hierarchical TiO_2 structures, comprising (1) assemblies of nanorods, and (2) nanoflowers that appear roughly spherical and made up of fine 8-10 nm diameter nanowires radiating out from a central point. These materials exhibited high photocatalytic activity towards 2-CEES photooxidation which was assigned to (1) better light absorption by assemblies of nanowires and nanorods

in comparison to individual nanorods, (2) improved separation of photogenerated carriers in thinner nanorods and nanowires and at Anatase/Rutile junctions, (3) high surface area, and (4) the exclusion of surface OH groups due to the formation surface functionalization with alkyl phosphonic acids via Ti-O-P bonds on the TiO_2. These materials can be used as a platform for modification by plasmonic nanoparticles in the future.

This page intentionally left blank.

INTRODUCTION

Plasmonic photocatalysis is promising way to harvest energy of visible light to drive chemical reactions on the surface of photocatalysts. Interaction of plasmonic nanostructures with light at certain frequencies leads to the generation of hot electrons that can directly or indirectly break chemical bonds on the surface of the photocatalysts. The current state-of-the-art material used in the majority of plasmonic systems, and in particular in photocatalysis is gold (Au), typically supported on a semiconductor support. Although gold is one of the best plasmonic materials, its real-life application is hindered by its high cost. RTMNs represent an attractive low-cost alternative to gold. Because of large concentrations of free carriers in some of these materials ($\sim 10^{22}$ cm^{-3}), they establish metallic optical properties which support LSPRs in the visible and near-infrared (IR) regions. Unlike Au, the optical properties of RTMN can be tuned by changing their processing conditions and composition thus making them more versatile than metals in terms of system design. Furthermore, the high-temperature stability of RTMN materials suit them well for catalytic processes, which are often carried out at higher temperatures due to reaction acceleration. While the photocatalytic activity of Au/TiO_2 NPs has been demonstrated before, very little work exists on plasmon-induced photocatalytic reactions by RTMN nanoparticles.

In one of the pioneering works on the TiN-driven plasmonic photocatalysis, it was shown that 50 nm TiN cubes supported on TiO_2 nanowires provide greater photocurrent enhancement for photoelectrochemical water splitting as compared to spherical Au NPs, when potential bias of 1.23 V vs reversible hydrogen electrode (RHE) is applied [8]. This was attributed to three major factors. First, the TiN NPs establish a broader plasmonic resonance that covers nearly the entire solar spectrum (500-1200 nm). Second, they demonstrate stronger field enhancement due to their natural cubic morphology, which enhances field strengths at the edges. And finally, third, they don't form a Schottky barrier with TiO_2. TiN and TiO_2 instead form an ohmic junction that allows charge to flow freely across the interface. An advantage of not having a Schottky barrier is greater hot electrons collection efficiency, if potential bias is applied. In such a case, not only the majority of hot electrons (not only the ones with the energy exceeding the Schottky barrier), but also cold electrons generated by interband transitions in TiN NPs can be injected into the semiconducting support [8]. A potential bias is required to accelerate the separation of photogenerated electrons and holes, thus suppressing their recombination.

ZrN NPs is another member of refractory plasmonic materials that exhibits optical appearance of gold. Previous theoretical and experimental research has shown that the LSPR of TiN is somewhat broader than that of gold and can exhibit significant sample to sample variability [2, 9]. ZrN is expected to have a sharper blue-shifted LSPR response in comparison to TiN [9]. Indeed, this theoretical prediction was verified for ZrN NPs decorated by a thin layer of SiN [10]. However, ZrN NPs appear to be less chemically inert than TiN, owing to zirconium's strong affinity for oxygen. A layer of dielectric ZrO_2 readily forms on the surface of ZrN NPs even in the presence of trace oxygen. The oxide layer has a detrimental effect on the LSPR, leading to its broadening and red-shifting [4].

Herein, both experimental and computational approaches are used in order to optimize the performance of TiO_2-supported TiN and ZrN NPs towards photoelectrochemical CH_3OH oxidation under visible excitation. Methanol photoelectrochemical oxidation was selected as a model reaction in this work. Prior to moving to more sophisticated reactions of plasmon-driven oxidation of large organic molecules, we attempted to confirm the feasibility of plasmon-driven photocatalysis by TiO_2-supported ZrN and TiN nanoparticles in a simple, well-characterized system. The choice of this redox reaction stems from its well-studied mechanism, the simplicity of identification of the three reaction products, and the fact that methanol is more easily oxidized than water.

After confirming feasibility of plasmon-driven photoelectrocatalysis by TiN/TiO_2 and ZrN/TiO_2 at the photocatalyst/solution interface, we attempted to re-design the plasmonic NP/semiconductor interface in order to create a Schottky barrier between the two interfaces. The absence of an electronic barrier between

Manuscript approved December 2, 2021.

the two interfaces limits their application to electrochemical interfaces (i.e. photocatalyst/electrolyte interface), at which potential bias can be applied. As such, such photocatalysts cannot be utilized at the interface with air. Two strategies had been explored in order to create a Schottky barrier between the TiN and semiconductor: (1) modification of plasmonic TiN NPs by decorating them with a gold shell, and (2) using semiconductor with a different band alignment in comparison to TiO_2. To implement the second strategy, GaN was selected as an alternative to TiO_2.

Unlike TiN NPs, Au NPs form a Schottky barrier with TiO_2, and therefore they are expected to demonstrate plasmon-mediated activity at the Au/TiO_2 interface with air. As such, the same Au/TiO_2 photocatalyst that demonstrated plasmon-mediated activity towards CH_3OH electrooxidation, was assessed as a model photocatalyst at the interface with air. 2-CEES (sulfur (HD) mustard simulant) served as a model organic molecule in this work. Plasmon-induced photocatalysis has been previously demonstrated for photooxidation of other organic molecules, including thiols [11, 12], alcohols [13-16], benzene [17, 18], phenolic compounds [19], etc. Neatu et al. [20] reported complete photooxidation of sarin, sulfur mustard and VX to innocuous products by Au/TiO_2 photocatalyst under visible excitation. However, the role of molecular oxygen in the photooxidation process was not very clear.

In this program, we elucidate the effect of oxygen on reaction mechanism by comparing 2-CEES reactivity in anaerobic (under He purge) and aerobic conditions. *In-situ* DRIFTS is utilized to follow dynamics of 2-CEES interaction with Au/TiO_2 photocatalyst under visible light excitation. We find that 2-CEES undergoes hydrolysis to 2-ethylthio ethanol in the dark, prior to visible light excitation both in anaerobic and aerobic conditions. However, in aerobic experiment, oxygen activates water molecules and accelerates hydrolysis in the dark. Visible light excitation in inert environment causes 2-CEES to partially desorb from the Au/TiO_2 surface likely due to photothermal effect, induced by photo-excited plasmonic Au nanoparticles. However, no photocatalytic reaction has been induced by visible light.

Low photocatalytic activity of the Au/TiO_2 photocatalyst towards 2-CEES oxidation in air was partially due to a low activity of the commercial P25 TiO_2 support utilized in our photocatalytic experiments. This observation motivated us to explore the TiO_2 materials with other morphologies, such as small (5 nm) spherical NPs, nanosheets, nanorods and hierarchical architectures comprised TiO_2 nanowires assembled in nanoflowers. The first promising results were obtained with 5 nm TiO_2 NPs and nanosheets immobilized on monodisperse SiO_2 Stöber spheres. 2-CEES was oxidized mostly to the corresponding sulfoxide (2-CEES-O). The photocatalytic reaction rates (in μmol/g/h) towards 2-CEES oxidation on SiO_2-supported 5 nm TiO_2 NPs and nanosheets exceeded that of P25 TiO_2 by *ca*. 28X-8X, respectively. However, even better results were demonstrated by TiO_2 hierarchical architectures modified by long-chain alkyl phosphonic acids. Photooxidation reaction rates of 99 and 168 μmol/g/h (quantum yields of 5.07×10^{-4} and 8.58×10^{-4} molecules/photon) were observed, which were more than on order of magnitude (*ca*. 50X-80X, respectively) higher than that of P25 TiO_2.

This work has benefited from multiple informal collaborations that had been developed in the course of the program. All electromagnetic and quantum modeling in this work was performed by Prof. Govorov's group from Ohio University. In-situ DRIFTS experiments on Au/TiO_2 photocatalysts exposed to 2-chloroethyl ethyl sulfide (2-CEES) under visible excitation were carried out by Drs. W. Gordon, A. Bolboa and M.McEntee (US Army DEVCOM Chemical Biological Center). Thin TiN films were deposited on n- and p-type GaN for Schottky barrier measurements by magnetron sputtering by Prof. V. Shalaev's group from Purdue University, IN. 5 nm TiO_2 NPs and nanosheets supported on SiO_2 Stöber spheres had been synthesized by Prof. M. Correa-Duarte's group (University of Vigo, Spain)

EXPERIMENTAL

Materials

Commercially Available Materials

20 and 50 nm TiN NPs were purchased from PlasmaChem. Nominally 50 nm ZrN NPs were acquired from American Elements, Inc. 50 nm citrate-capped Au NPs dispersed in water were purchased custom-made by HQ-Nano, Inc. P25 TiO_2 (Aeroxide® P25, 21 nm primary particle size) was acquired from Sigma Aldrich. All solvents for organometallic synthesis were dried and distilled from either sodium (toluene), sodium benzophenone ketyl (THF) or P_2O_5 (CH_2Cl_2) and distilled before use. Solvents for Demeton-S decontamination experiments were not dried.

Synthesis of in-house made materials

$MCl_3[THF]_3$ complexes that served as pre-cursors for synthesis of first row early transition metal nitride powders and nanomaterials were prepared in a similar manner to Refs [21-23]. Solid solutions of these isomorphous complexes $M_xM'_{1-x}Cl_3(THF)_3$ were prepared by co-crystallization. Heating the precursor under NH_3 flow from 800-950 °C produced powders of the nitride MN, and solid solutions of these precursors produced alloys of the nitrides. Nanomaterials were synthesized by two methods: (1) reaction of a $MCl_3(THF)_3$ solution with 3 eq of KNH_2 in THF in the presence (or absence) of oleylamine (OA), followed by nitridation under NH_3 flow at 650-950 °C and (2) loading a porous catalyst support such as pelletized Al_2O_3 with the $MCl_3(THF)_3$ complex, followed by similar heat treatment. The details of the synthesis can be found in Ref. [1]

ZrN NPs were synthesized by ammonolysis of $Zr(NMe_2)_4$ All manipulations were carried out in a drybox in an Ar atmosphere or on a vacuum line. Clean $Zr(NMe_2)_4$ was prepared following a protocol from the literature [24]. A portion of the $Zr(NMe_2)_4$ (1.28 g, 4.78 mmol) was introduced into a reaction bulb charged with heptane and 21.6 mmol NH_3 was condensed into the bulb at 77K. The mixture was stirred at room temperature for 24 h and then at 80 °C for another 24 h period. Solids were isolated by filtration. The solid was loaded into an alumina boat, inserted into a furnace, and heated under NH_3 flow first at 250 °C for 15 min, and then at 900 °C for 2.5 h. It was then cooled under N_2 flow once the temperature dropped to 500 °C. A mostly black powder was isolated. Crystallite size was 11 nm, as determined by analysis of PXRD peaks. Larger 17 nm ZrN NPs were obtained by heat-treatment of the same precursor at 1050 °C.

Methods

UV-Vis spectroscopy

Visible light absorption of plasmonic NPs, and their TiO_2-supported powders were characterized by UV-Vis spectra, which were collected in transmission and diffuse reflectance mode for liquid and powdered samples, respectively. Powdered samples were diluted to 3 wt% with KBr prior to collecting spectra. Perkin-Elmer UV/VIS/NIR λ 1050 spectrometer, equipped with integrated sphere was used.

XPS

XPS was performed on a Thermo Scientific K-Alpha instrument (Al Kα radiation). The samples were prepared by pressing the ZrN and TiN powders onto indium foil (thickness 1 mm, Sigma Aldrich). Flood gun was used to avoid charging of insulating powders. Survey and high resolution core level Zr3d, Ti2p, N1s, O1s and C1s spectra were collected. All peaks were referenced to the C1s peak at 285 eV. Peak fitting was performed with CASA software, after background correction by Tougaard [25] and Shirley methods for ZrN and TiN nanoparticles, respectively. The line shapes of core level spectra were constructed using Gaussian/Lorentzian profiles.

PXRD

Powder XRD patterns were recorded on a Rigaku SmartLab 2080B212 3kW powder X-ray diffractometer with Cu Kα radiation. Crystallite size was determined by Rigaku PDXL-2 software v 2.0.3.0 using the Halder-Wagner method.

TEM

Samples for TEM imaging were prepared by drop casting a suspension of TiN and ZrN samples dispersed in isopropanol onto a lacey carbon film-coated copper mesh TEM grid. The TEM (models JEOL JEM2200FS and JEOL ARM200F) was operated at 200 kV and used to obtain bright-field images and selected area electron diffraction patterns. The images were recorded with a Gatan OneView camera, with camera constants calibrated using a conventional TEM standard (Mag*I*CAL) based on molecular beam epitaxial Si/SiGe layers. The images taken over the course of 100s of seconds of continuous irradiation (while any given image only takes ~0.1-1 s to acquire) showed no compositional or morphological change of the sample, confirming that extended irradiation did not cause sample beam damage.

DRIFTS

Prior to DRIFTS experiments, approximately 5 mg of the TiO_2 or Au/TiO_2 powders were placed in a porous ceramic cup and the sample was calcined at 425°C in air for 4 hours. The sample cup was then placed in the Pike Technologies DiffuseIR reactor cell and purged with a flow of 1 mL/min of ultrazero grade air (ZA, Airgas, ~20% O_2 with a balance of N_2 and trace impurities) or 1.45 mL/min of helium (Airgas, 99.999% purity) for aerobic and anaerobic conditions, respectively for approximately 18 hours. The DRIFTS cell was thermostatted at 25 °C. CEES was delivered to the sample via diverting the feed gas through a glass saturator (Glassblowers) that was thermostatted by a water bath set to 20 °C. Visible light illumination was performed using a 200 W mercury-xenon broadspectrum lamp (Newport Model 67005) equipped with a long pass filter to exclude all transmission <480 nm (Newport 20-CGA-495). Light was directed to the sample cup via a custom bundled fiber optic with the light emitting end being ~ 6 mm above the sample. Light intensity at the sample was estimated to be ~40 mW cm^{-2} as measured by a Newport m1918R power meter coupled with a 918D-ST-UV probe. DRIFTS IR spectra were recorded with a Thermo Fisher Scientific 6700 FTIR by collecting 125 spectra averaged over 58.85 s with a 2 cm^{-1} resolution at a gain of 2.

Photoelectrochemical Characterization

Photoelectrochemical experiments were conducted in a three-electrode photoelectrochemical cell, filled with aqueous solutions of 0.5M CH_3OH+0.1M NaOH. The TiN/TiO_2, Au/TiO_2, and TiO_2 films deposited on FTO-coated glass substrates served as working electrodes (WEs), while platinum foil and Ag/AgCl in 3 M NaCl (BioLogic, Inc) were used as counter and reference electrodes (RE), respectively. To ensure that potential of the RE is not affected by the presence of OH^- ions in electrolyte solution, its potential was measured against a new Ag/AgCl RE after concluding each set of photoelectrochemical experiments. Discrepancies within 4 mV have been observed. This is an expected result, as the minimal allowable chloride to hydroxyl ratio of $1.25 \bullet 10^{-2}$ (i.e. the ratio above which the effect of interfering species on the RE potential is not expected to be observed) [26] exceeded at least by 3 orders of magnitude in our work ([Cl-]/[OH-] = 3 M/0.1 M = 30). The diameter of the optical window coated with the thin film of the photocatalyst and exposed to visible light was 7 mm. A μAutolab type III potentiostat (Metrohm) was used for electrochemical measurements. Prior to collecting CVs, the WEs were held at open circuit potential (OCP) for ~1h until the stable OCP is observed. The films were then probed under broadband white light excitation. In this set of experiments, cyclic voltammetry (CV) curves were collected at 10 mV/s in the dark under visible light excitation (with and without 425 nm cut off filter) in the potential range between -0.6 and 0.5 V. The wavelength dependence of the photocurrent of methanol oxidation was studied at potential equal to OCP, 0.2 V, and 0.4 V. Incident photon-to-electron conversion efficiency (IPCE) was calculated according to the following equation:

$$IPCE\ (\%) = (J_{photo} \bullet 1240 \bullet 100)/(J_0 \bullet S \bullet \lambda), \quad (1)$$

where J_{photo} (A) is a photocurrent, J_0 (W/cm^2) is the power density of light source at a specific wavelength λ (nm), and S (cm^2) is an electrode surface area.

Illumination sources consisted of LED lights (ThorLabs, 470-950 nm range) or a broadband white light source (Lumina FO-150, 150W halogen illuminator, 360-1000 nm, Chiu Technical Corporation). A 425 nm cut off filter was mounted between the broadband light source and the cell to observe effect of visible light. In a similar manner, 10 nm band pass filters (centered at 490, 520, 550, 580, 640, 670 and 750 nm) were placed in front of the LED sources when studying wavelength dependence of a photocurrent. The power of the light sources was measured by optical power and energy meter (842 PE, Newport), coupled with high performance photodiode sensor (918D, Newport). All the wavelength dependence measurements were carried out in the Faraday cage, to reduce noise caused by electrical equipment.

Materials Decontamination Challenge

Reactivity challenges were performed on powdered samples in the bottom of the 2 mL clear GC-MS vials to enable the use of visible light excitation [7, 20]. A stock solution of 2-CEES (19.25 µL, 1.65x10^{-4} mol) was prepared in 2 mL of CH_2Cl_2. Materials were challenged with 2-CEES via deposition of 25 µL of the 2-CEES stock solution followed by evaporation of the solvent CH_2Cl_2 for 10 minutes after which the vials were sealed and exposed to light or stored in the dark. A calibration curve for 2-CEES concentration assessment was constructed from gas chromatography coupled with a mass spectrometer (GC-MS) analysis of solutions with known volumes of the contaminant stock solution (1 µL to 30 µL) measured with a 50-µL syringe. The known volumes of the 2-CEES stock solution were diluted with acetonitrile to 1 mL total volume prior to GC-MS analysis. The chromatographic peak areas were determined by integration and a peak area vs. concentration plot was generated.

The visible light source used was a broadband Lumina FO-150 (Chiu Technical Corporation, Kings Park, NY, USA) utilized at full power with a 3-74 UV cut-off filter to eliminate wavelengths below 400 nm. Initial challenges were performed over a 24-hour period to test the viability of the materials for their reactivity toward 2-CEES. Subsequent time trials were performed for the highly active materials to assess reactivity with exposure times of 1, 4 and 8 hours. Samples for each simulant challenge were extracted with 1 mL of acetonitrile and analyzed by GC-MS for residual 2-CEES and reaction byproducts. All challenges were run in duplicate in order to assess variability and to conserve materials.

GC-MS analysis was performed using an Agilent 7890B gas chromatograph coupled with an Agilent 5977B mass spectrometer (MS) detector operating in electron ionization mode and an Agilent 7693A autoinjector (Agilent Technologies, Santa Clara, CA, USA). The column was a Restek Rxi®-5HT with a Crossbond® 5% diphenyl 95% dimethylpolysiloxane film (Restek Corporation, Bellefonte, PA, USA). The carrier gas was helium, with a constant flow rate of 1.636 mL min^{-1}. The injection volume was 1 µL, with a split injection ratio of 10:1. The temperature program has an initial temperature of 65 °C for two minutes, then 10 °C·min^{-1} ramp to 130 °C, followed by a 20 °C·min^{-1} ramp to 280 °C, with a two minute post-run hold at 300 °C. The injection inlet temperature, auxiliary temperature, MS quad temperature, and MS source temperature were 275, 280, 150 and 230 °C, respectively. The solvent delay was set at 2.00 minutes and the detector scanned from 34 to 350 m/z.

RESULTS AND DISCUSSION

Synthesis, Plasmonic Properties, and CWA decontamination Activity of First Row Early Transition Metal Nitride Powders and Nanomaterials

Synthesis conditions, BET surface area and crystallite size of the synthesied MN (M=Ti, V, Cr or their mixtures) materials are summarized in Table 1.

Table 1. Synthesis conditions, BET surface area and crystallite size of MN nanomaterials

Method A					
Precursor $[MCl_3(THF)_3]$, g	**Intermediate temps, °C**	**Final temp**	**Yield, g**	**BET, m^2/g**	**XRD**
A1 Ti (0.54)	250, 400, 650	850 16h	0.074 (82%)	20.73	30 nm TiN
A2 V (2.04)	200, 450	900 1h	0.34 (96%)	7.16	42 nm VN
A3 V (0.76)	200. 450	900 2h	0.13 (98%)	0.29	60 nm VN
A4 Cr (1.035)	250, 450	850 2h	0.17 (93%)	0.33	60 nm CrN, 53 nm Cr_2N
A5 Ti-V (1.34)	250, 450	850 1h	0.19 (83%)	34.42	15 nm MN
A6 Ti-Cr (0.99)	200, 450	850 2h	0.12 (71%)	0.67	19 nm MN, M_2N
A7 Ti-V-Cr (1.50)	200, 450	850 2h	0.22 (85%)	7.67	25 nm MN
Method B					
$[TiCl_3(THF)_3]$, KNH2	**Intermediate temps**	**Final temp**	**Yield, g**	**BET, m^2/g**	**XRD**
B1 1.01 g, 0.465 g KNH_2	150, 250 °C	850 °C 16h	0.106 (50% of precursor)	45.40	15 nm TiN
Method C					
$MCl_3(THF)_3$; KNH_2; OA, g	**Intermediate temps**	**Final temp**	**Yield, g**	**BET, m^2/g**	**XRD**
C1 M=Ti 2.02; 0.92; 1.01	200, 350	850 1h	0.17 ~50% portion	201.72	TiN; 6 nm
C1a	200	650 1h	0.18 ~50% portion	183.55	TiN 4 nm
C2 (Ti-V-Cr) Ti 0.74 V 0.77 Cr 0.81 1.03 KNH2; 1.23 g OA	250, 350	850 1h	0.42	174.53	MN; 6 nm
C3 V 1.99; 0.89; 1.28 OA	250, 350	850 1h	0.31	101.68	VN; 18 nm
C4 Cr 1.57; 0.70; 1.28 OA	200, 450	850 ½ h	0.25	139.68	CrN; 11 nm, carbides, carbonitrides

The early transition metal trichloride tris-THF adducts $[MCl_3(THF)_3]$ [M= Ti, V, Cr] are excellent precursors to bulk nanostructured metal nitrides MN, simply by heating the precursor material in a tube furnace under flowing, anhydrous ammonia. Since the precursor has almost no vapor pressure, most of the produced nitride remains in the alumina boat in which the precursor was placed, and the yields range from 71-98%. With the Ti and V precursors, films that are presumably metal nitride did deposit on the quartz tube and the alumina boat containing the precursor. As a test of film growth, in one instance (**A3**), a quartz slide was placed with the boat and a film of VN was deposited on the slide. All of the nitride products are single phase except with Cr, where some powder XRD peaks for Cr_2N were evident (Fig. 1). Additionally, all of the trichloride precursors have similar crystal structures and solubilities in CH_2Cl_2, and crystals of mixed precursors were easily prepared by slowly evaporating a CH_2Cl_2 solution of the precursors under inert atmosphere conditions. Those crystals were converted into nitrides in the same manner, and produced single phase MN as determined by XRD, except in the case of **A6**, which had a high fraction of Cr. The XRD patterns are shown in Fig. 1. Typically, the linewidths of materials produced from a single metal were much narrower than those produced from a mixture of metals, indicating larger crystallite sizes in the single metal cases. However, the morphology of the metal nitrides produced in this manner was typically a porous network composed of nanoparticles fused together, as evidenced by the SEM images (Fig. 2). BET data (Table 1) shows higher surface areas that correlate to lower thermolysis temperatures and shorter heating times, as expected.

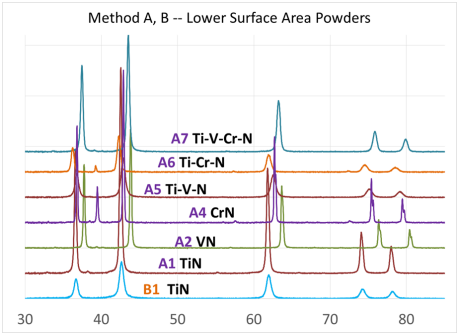

Fig. 1. X-ray powder patterns of the A and B series metal nitride materials

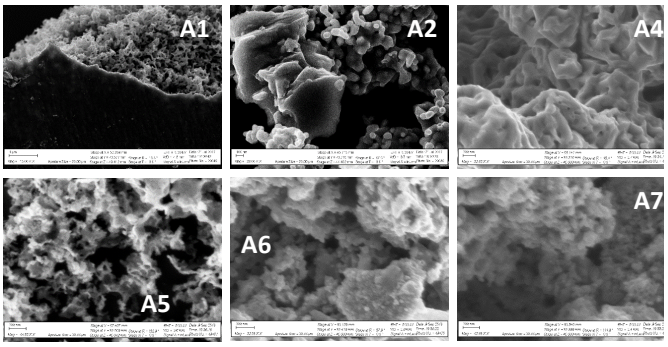

Fig. 2. SEM images of representative MN materials obtained by thermolysis of $MCl_3(THF)_3$ under flowing ammonia

Since the goal was to generate individual nanoparticles and not macroscopic, albeit porous, materials for plasmonic catalysis, the synthesis was modified. Reaction of the $TiCl_3(THF)_3$ precursor with 3 eq of KNH_2 prior to thermolysis also produced porous materials composed of nanoparticles (B1), but adding oleylamine to that reaction (series C) accomplished the goal of producing individual nanoparticles that were only moderately agglomerated. BET surface areas were high, ranging from 57-202 m^2/g, and the particle size calculated from BET was mostly consistent with the crystallite sizes determined by XRD, of which the powder patterns are shown in Fig. 3.

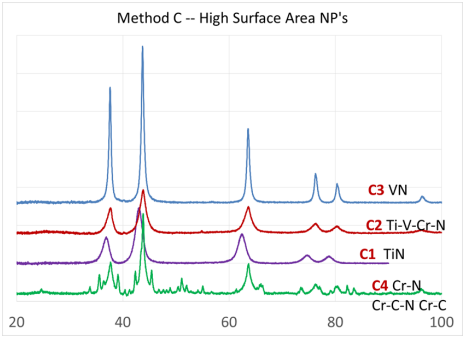

Fig. 3 XRD powder patterns of high surface area nanopowders, series C

In order to maximize the light absorption of small TiN nanoparticles by avoiding their agglomeration and oxidation, they were in-situ deposited on a porous support. Gold nanoparticles were deposited in the same manner to serve as a reference (series **D** nanomaterials). We used a nonreactive support, porous γ-alumina, due to the complications presented by porous TiO_2 (which is commercially available), but is reactive under a stream of flowing NH_3 and presents issues that will not be discussed here. In these examples, the TiN was loaded into the support at about a 7 wt % concentration which represented the maximum amount of $TiCl_3(THF)_3$ precursor that could be absorbed into the support. For the case of Au, the 2% loading achieved here is probably nowhere near the maximum achievable, since the concentration of the stock $HAuCl_4$ solution used was fairly low. While the XRD powder pattern of these materials shows evidence for the most prominent peaks of Au and TiN (Fig. 4a), those peaks are heavily obscured by reflections from the support and are not conclusive. Therefore, we obtained TEM images of these materials, which clearly show 3-4 nm cubic TiN and 20-30 nm spherical Au crystals present due to the Z contrast with the alumina support (Fig 5). Small TiN nanocrystals are not agglomerated and evenly dispersed on the support.

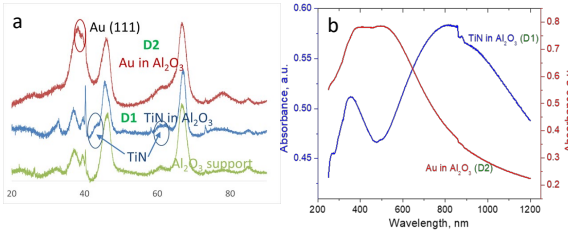

Fig. 4 (a) XRD powder patterns of the **D** series materials and the pure Al_2O_3 support for comparison. (b) Kubelka-Monk transformations of diffuse reflectance spectra of the D series materials recorded on KBr mixtures using an integrating sphere.

Optical properties of the synthesized materials were characterizaed by UV-Vis spectroscopy. Comparison of UV-Vis spectra displayed in Fig. 6 shows that our coarser VN (**A2**) and Ti-V-N (**A5**) nanoparticles dispersed in water exhibit a broad absorption maxima centered around 800 nm. TiN (**C1**) nanoparticles dispersed in H_2O demonstrate two rising branches extending to the left and right from 650 nm, with no clearly pronounced absorption maximum. On the contrary, **C1** particles dispersed in CH_3OH demonstrate a clearly pronounced LSPR at ~ 900 nm. The absence of LSPR in water is likely due to oxidation and agglomeration of the ca 6 nm TiN nanoparticles. The strongest LSPR is observed for aqueous suspensions of 30 nm commercial TiN nanoparticles (Fig. 6b, green curve). The maximum centered at 700 nm is blue-shifted vs. those of **C1** TiN NPs in CH_3OH, and VN and Ti-V-N in H_2O. The red-shift and broadening of plasmonic resonances of 6 nm TiN, and 15 nm Ti-V-N NPs vs 30 nm TiN NPs is likely due to their stronger oxidation [27]. Diffuse reflectance spectra measured on TiN/γ-Al_2O_3 and Au/γ-Al_2O_3 powders are depicted in Fig. 4b. A clearly pronounced absorption maximum at ~800 nm is observed for TiN/γ-Al_2O_3 (**D1**). The maximum is ~100 nm blue-shifted compared to its solution counterpart, probably due to the less pronounced agglomeration/oxidation of TiN nanoparticles. While less pronounced agglomeration of supported TiN nanoparticles is evident from Fig.5, (D1), their less pronounced oxidation can be confirmed by comparison of corresponding Ti2p and N1s XPS spectra [1]. The least oxidized TiN nanoparticles are 30 nm commercial nanoparticles. For Au/ γ-Al_2O_3 (**D2**), a broad maximum centered at 500 nm is observed. A close examination shows two overlapping maxima centered at ~520 and 390 nm. The first maximum is due to Au LSPR [2], while the second one is likely due to light absorption by the support.

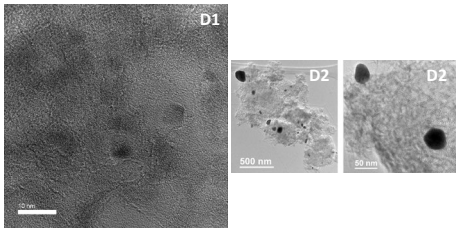

Fig. 5 TEM images of samples **D1** and **D2**

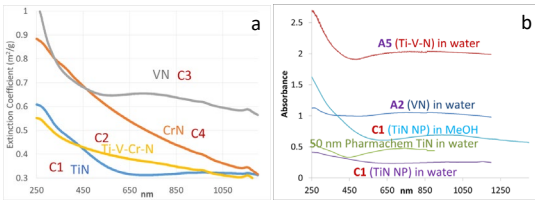

Fig. 6 (a) UV-VIS spectra of dispersions of C series nanomaterials in water, 0.1 mg/mL. (b) A comparison of various nanomaterials in water and methanol with commercially available TiN nanoparticles in water

Following optical and physico-chemical characterization, the materials that demonstrated enhanced visible light absorption (TiN-Al2O3) and high BET surface area were tested for their activity toward decomposition of nerve agent VX simulant Demeton-S.

Demeton-S shown in Figure 7 (b) is utilized as a simple CWA simulant with the potential to investigate the reactivity of new active materials for decontamination [28-30]. Hydrolysis and oxidation relevant for organophosphate nerve agent VX (Figure 7(a)) and/or vesicant sulfur mustard HD (Figure 7(c)) can be investigated due to the presence of both a P-S bond and the thioether linkage in demeton-S [31-35]. In addition to overall percent reduction of the simulant Demeton-S the analysis for and the identification of byproducts was also performed for understanding the chemical reactivity of these materials.

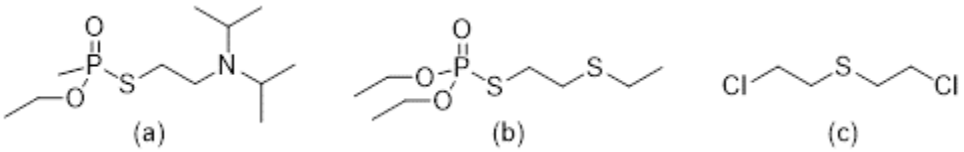

Fig. 7. Chemical agent simulant Demeton-S (b) has both the P-S linkage similar to nerve agent VX (a) and the thioether linkage similar to vesicant HD (c)

Preliminary screening experiments showed the TiN with the smallest nanoparticle sizes and highest surface area (**C1**) and the TiN impregnated in alumina (**D1**) to be the best materials to test for activity against Demeton-S. Percent reductions for the simulant challenges normalized to the mass of TiN and TiN-Al_2O_3 in addition to control challenges are shown in Table 2. The control challenges show consistent percent reductions between 4% and 8 % indicating minimal loss of simulant during the challenge protocol. Inclusion of the TiN and TiN-Al_2O_3 into the vial showed significant increases in the percent reduction for all challenge times including the 0 hour exposures indicating that some simulant is readily sequestered on to the surface of the materials. Based upon the chromatographs in Fig. 8 and the percent reductions presented in Table 2 the reaction appears to have reached completion within 6 hours. The observation of less than 100% reduction is indicative that reactive species on the surface are responsible for the decontamination of Demeton-S which are potentially consumed or blocked after the reaction [35, 36]. This hypothesis is supported by FTIR spectra of KBr pellets of the treated samples which show absorptions for phosphate on samples treated with Demeton-S (supporting information). The observed reactivity differences between the two materials challenges is believed to be a result of surface area differences between the two materials. The TiN having a greater surface area has more reactive sites available for hydrolysis of the deposited simulant.

Table 2. Percent reduction of demeton-S normalized to catalyst mass with respect to amount of simulant deposited

% Reduction from Concentration of Simulant Deposited	0 hours Exposure	6 hours Exposure	24 hours Exposure
Control-1	5.4 %	4.4 %	7.8 %
Control-2	5.3 %	17.6 %*	6.9 %
TiN-1	26.9 %	56.7 %	56.3 %
TiN-2	33.4 %	53.0 %	59.3 %
TiN-Al_2O_3-1	25.3 %	38.6 %	38.6 %
TiN-Al_2O_3-2	16.0%	37.0%	42.4 %

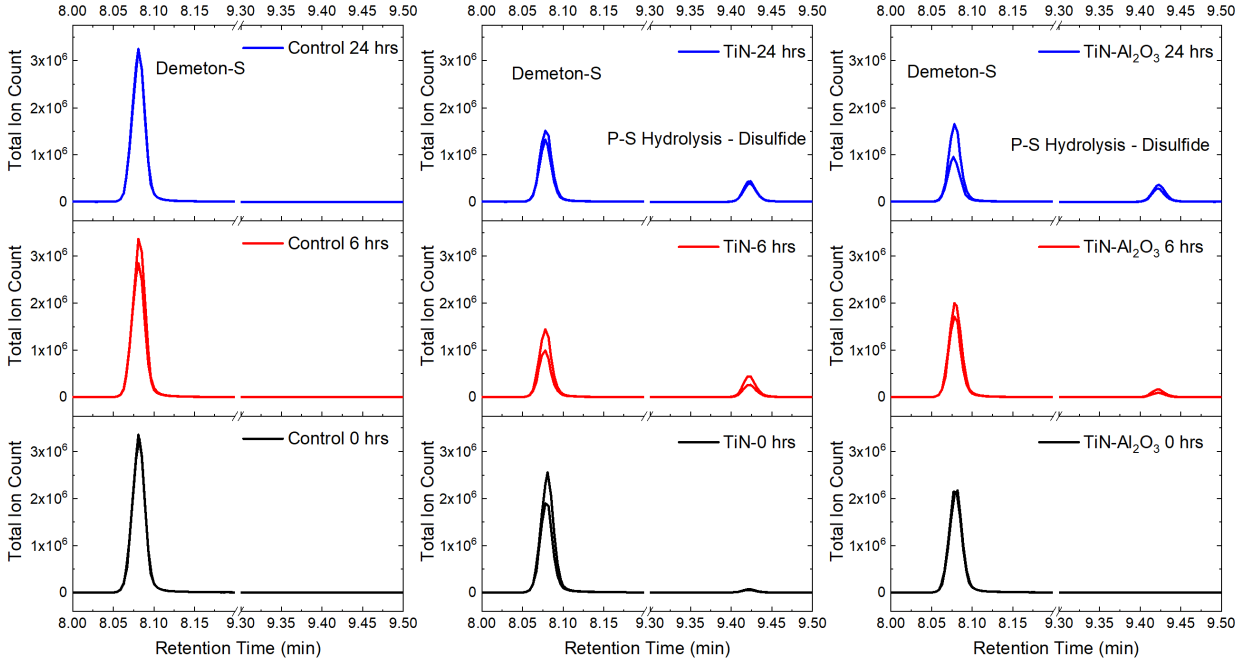

Fig. 8. Chromatograph stacks for control, TiN and TiN-Al_2O_3 challenges

In addition to percent reduction the chromatography results in Figure 8 show the presence of a byproduct at a retention time of 9.42 minutes. Analysis of the mass spectrum fragmentation pattern of the byproduct peak [1] indicates hydrolysis of the P-S linkage of demeton-S and formation of the disulfide shown in Figure 9. The disulfide byproduct is present for both TiN and TiN-Al_2O_3 materials and is consistent with the preferential reaction route for the decontamination of the organophosphate nerve agent VX [31-35]. Chromatographs for the TiN-Al_2O_3 also show the presence of minor quantities of the thiol hydrolysis product with a retention time of 2.62 minutes [1]. The phosphate byproduct was not detected and is believed to be sequestered on the surface of the materials consistent with previous literature reports [35, 36].

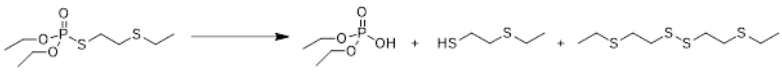

Fig. 9. Demeton-S hydrolysis reaction scheme via cleavage of the P-S bond

Synthesis of TiN-Au Core-shell Nanoparticles

The deposition of a relatively thin Au layer as a shell on ceramic nanoparticles is a significant technological challenge due to gold's great affinity for itself over other material surfaces and therefore propensity to produce separate Au NPs rather than ultra-thin films on surfaces. There are literature examples where thicker Au layers were reported (>10 nm) effected via the approach of first tethering seed particles to the core ceramic particle surfaces, followed by successive treatments to deposit Au via a reductive method [37-39]. This approach requires multiple successive Au deposition steps due to the initial growth of the Au seed particles, followed by the formation of surface Au islands, and eventually leading to a complete, filled-in Au shell that is quite thick.

In an attempt to conserve Au and produce a thin conformal Au coating on ceramic NPs we took the approach of directing the Au reduction to occur at the core particle surface via the partitioning of the Au precursor to the particle surface. The idea is that the wet Au-oleylamine complex in a hydrocarbon solvent should preferentially be associated with the more hydrophilic ceramic particle surface and excess oleylamine would serve as a soft reducing agent, thereby directing the deposition of reduced Au onto the ceramic particle surfaces and preventing the seeding and growth of separate Au nanoparticles.

To that end, the reaction was generally carried out in a 20 mL scintillation vial with a screw-type cap, with approximately 25 – 50 mg of TiN NPs, and a total reaction volume of ~ 5 mL. The formation of the Au-oleylamine complex was induced in situ via the mixing of $HAuCl_4$ with 10X excess oleylamine in hexanes. This step was carried out by using an aqueous solution of $HAuCl_4$, and for various samples the solution was introduced either intact, or after partial drying via the removal of the majority of the water in

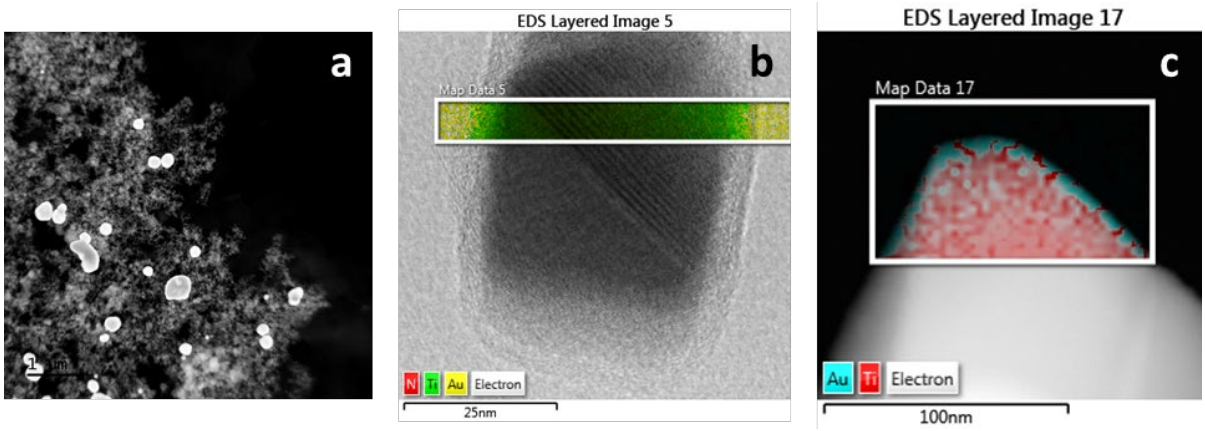

Fig. 10. (a) HAADF-STEM micrograph of a representative unsuccessful sample where large Au nanoparticles were produced. The high Z contrast Au appear white on the gray TiN particles. (b) EDS layered image exhibiting Au signal across the TiN particle, with greater Au signal intensity at the edges. (c) EDS layered image providing visualization of islands of Au on the surfaces of the TiN nanoparticle.

vacuum. It was observed that the $HAuCl_4$ reacted rapidly with the oleylamine, fully dissolving and producing a light yellow solution in hexanes. In the following step, 30 nm TiN NPs (Plasma Chem) were added and a benchtop sonication bath was used to disperse and suspend the TiN. This suspension was then set up on a low speed shaker and left to agitate. It was observed that the solution bleached from light yellow to clear within approximately 72 h.

The majority of the samples prepared in this manner exhibited strong, sharp Au peaks in the PXRD. The presence of relatively large Au NPs in these samples was also confirmed via HAADF-STEM (Figure 10a). For one specific sample the results appear to be more successful. In that particular instance the $HAuCl_4$ was dried manually, on a Schlenk, line at room temperature and the drying process was halted at the moment when the sample appeared to cease bubbling and formed a solid. The PXRD in this case showed extremely

faint and broad Au peaks. The HR-TEM/EDS analysis for this particular sample showed no Au nanoparticles, and the Au signal in the EDS mapping experiment showed a constant, but low, Au signal over all the TiN surfaces (Figure 10b&c). Unfortunately, successfully repeating this result has been challenging.

Comparing Photoelectrochemical Methanol Oxidation Mechanisms for Gold vs Titanium Nitride Nanoparticles Dispersed in TiO_2 Matrix

First, we compare the visible light absorption by 20 and 50 nm TiN and Au NPs in order to aid interpretation of the photocatalytic CH_3OH oxidation experiments. Figure 11 contains the absorption (extinction) spectra of aqueous colloid solutions of 20 and 50 nm Au and TiN NPs, measured at the same concentrations (expressed in wt.%) of the corresponding NPs. Broad absorption maxima centered at 650 and 665 nm are observed for 20 and 50 nm TiN NPs, respectively. For the Au NPs, the resonant absorption features are sharper and blue shifted (522 and 530 nm for 20 and 50 Au NPs, respectively). These absorption features are due to LSPR [8, 19]. As expected, an increase in concentration of both TiN and Au NPs in Fig. 11 leads to an increase in intensity of corresponding absorption maxima. With an increase in particle size from 20 to 50 nm, the intensity of absorption maxima of the TiN and Au NPs increases as well, but not as

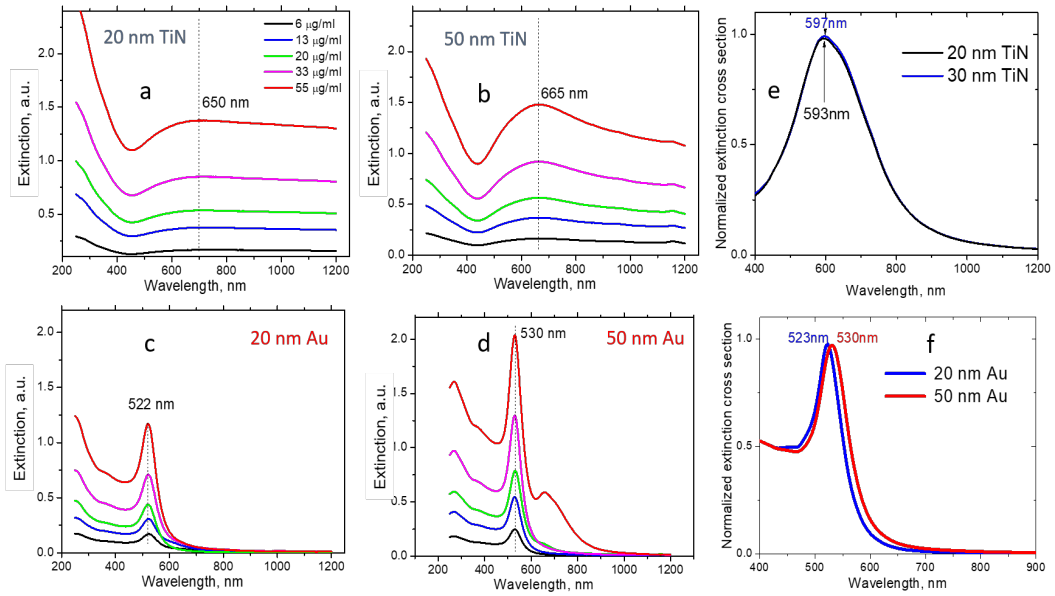

Fig. 11. Experimental UV-Vis spectra recorded in aqueous colloid solutions of (a, b) 20 and 50 nm TiN and (c, d) 20 and 50 nm Au NPs of different concentrations, and computed extinction cross sections for (e) 20 nm and 30 nm TiN nanocubes and (f) 20 nm and 50 nm Au spherical NPs.

significant for TiN NPs vs. Au NPs. A prominent feature of the absorption spectra, shown in Fig. 11, is a sharp onset in the region below *ca*. 450 nm. Light absorption in this region is due to interband transitions in the TiN (N(2p)→Ti(3d)) and Au (6d→5sp) NPs [8]. Note, that an additional interband transition is allowed for TiN material in the UV region, at photon energies above 5 eV (or below 247 nm) [40]. A detailed comparison of visible light absorption by Au and TiN NPs can be found elsewhere [8].

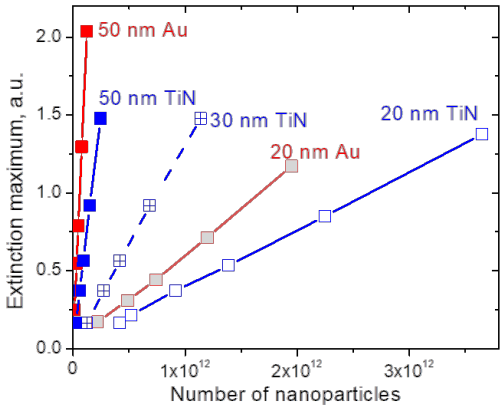

Fig. 12. Extinction maxima taken from Figure 1, as a function of number of 20 and nominally 50 nm TiN and Au NPs in 3 ml of corresponding colloid solutions. Dashed lines corresponds to extinctions of 30 nm TiN NPs

In order to compare the absorption of individual TiN and Au NPs, the extinction maxima from Fig. 11 were analyzed as a function of NP density, assuming a homogeneous size distribution. As such, the slope of each line shown in Fig. 12, represents the extinction per NP. A comparison of the slopes obtained for 20 and 50 nm Au and TiN NPs shows that, on average, 20 nm Au NPs absorb light 1.6X more efficiently compared to TiN NPs of the same size. The difference in extinction is significantly more pronounced for the 50 nm NPs, with the Au NPs absorbing light 2.7X more efficiently than TiN NPs. The increase in the extinction ratio with increased particle size may be due to (1) a larger optical cross-section of the Au vs TiN NPs and (2) an inhomogeneity in the particles size distribution for 50 nm TiN, as will be discussed later.

Further, we used the ratio of the extinctions for 50 nm and 20 nm NPs to evaluate the contribution of scattering to the maximum extinction. We expected to obtain a ratio of $(25\text{ nm}/10\text{ nm})^3=15.6$ when absorption dominates and $(25\text{ nm}/10\text{ nm})^6=244.1$ when scattering dominates the extinction process. In fact, the measured extinction ratio of 50 to 20 nm Au NPs of 27.7 lies in between these two bounds suggesting contributions from both scattering and absorption processes. For TiN NPs, this ratio of 16.2 falls close to the absorption defined lower bound (15.6). Such insignificant contribution of scattering into extinction with increase in particle size from 20 nm to 50 nm seems surprising. This may be due to either TiN intrinsic physical properties (not really metallic), or inhomogeneity of TiN NPs size distribution. To test the latter hypothesis, morphology of 20 and 50 nm TiN NPs was examined using TEM. The lower resolution images of 20 and 50 nm TiN NPs (Fig. 13a and c, respectively) show that these NPs have preferentially cubic morphology, although triangular and elongated shapes are also present. Regarding the particle size, the size of nominally 20 nm TiN NPs (Fig. 13b), as expected, is dominated by particles within 10-30 nm range. Surprisingly, not too many 50 nm NPs can be seen in the TEM image collected from nominally 50 nm TiN NPs (Fig. 13d). Analysis of the particle size distribution confirms that the size of majority of nominally 20 nm TiN NPs

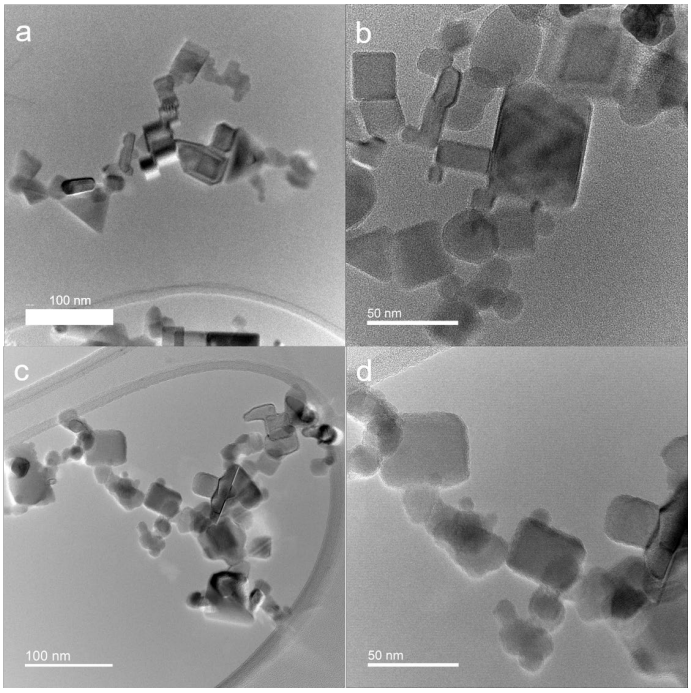

Fig. 13. TEM images of (a,b) 20 nm and (c,d) 50 nm TiN NPs (PlasmaChem) acquired with different resolution

falls within 20 nm range (Fig. 14a). The particle size distribution has an asymmetric shape, with a long tail towards the larger particle sizes, indicating non-uniform particles size distribution. The histogram of 50 nm NPs (Fig. 14b) has a more complicated shape, with one narrow maximum centered at 20 nm, and a broader one centered at 30 nm. Only ~2% of NPs have dimensions within the 50 nm range. Although the 20 nm NPs make up the largest fraction (28%) of nominally 50 nm NPs, the majority of NPs (57%) fall within 24-42 nm range. The results of particle size analysis by TEM was verified by a Scherrer analysis of the XRD patterns produced by 20 nm and 50 nm TiN NPs. Indeed, an average crystallite size of 20.3 and 27.4 nm, was obtained for 20 and 50 nm NPs, respectively. This explains why the ratio of the extinctions per NP for nominally 50 and 20 nm TiN NPs was lower than expected. Instead of comparing 20 and 30 nm TiN NPs, we mistakenly relied on the particle size provided by the manufacturer. The discrepancy between the nominal and actual particle size for 50 nm TiN NPs is likely due to a difficulty to control particle size while implementing physical methods, such as plasma arc discharge, for synthesis of NPs, compared to wet chemistry methods. Using correct NP size, the ratio of extinctions per NP is 3.5 which is close to 3.4 expected for absorption-defined extinction process. This suggests small contribution of scattering in TiN extinction.

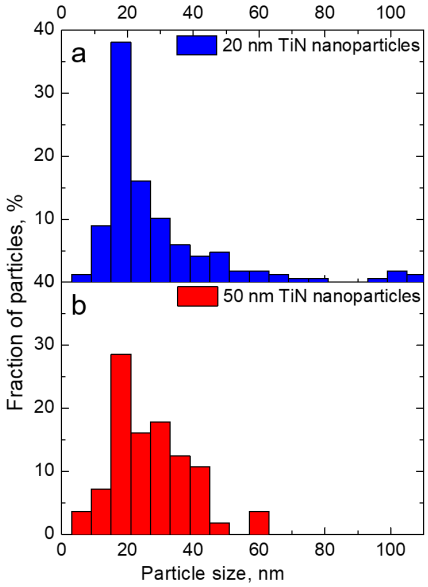

Fig. 14. Particle size distribution for (a) 20 nm and (b) 50 nm TiN (PlasmaChem) nanoparticles

Information on actual dimensions of TiN NPs (20 and 30 nm) was used for calculations of their extinction cross-sections and comparison to those of spherical Au NPs (20 and 50 nm in diameter). The results of modeling are displayed in Figures 11e, f. The TiN NPs were modelled as nanocubes with the rounded edges (5 nm and 8 nm rounding radii for the 20 nm and 30 nm TiN cubes). As expected, an excellent agreement is observed for the position of the Au plasmon. For TiN NPs, agreement is semi-quantitative. The theory predicts a well-defined plasmon peak at ~ 600 nm. The experimental position of the plasmon peak is at 665 nm. For the given, relatively small sizes of the NPs, the size-dependence of the positions of the plasmon resonance in theory is weak (Fig. 11 e,f), as expected. While this prediction is in quantitative agreement with the experimental results for the Au NPs (~8 nm vs 7 nm for experimental vs theoretical red shift with increase in NP diameter from 20 to 50 nm), it only qualitatively agrees with the experimental observations for TiN NPs (15 nm vs 4 nm red shift with increase in NP dimensions from 20 to 30 nm). The discrepancy can come from: (1) polydispersity of the size and shapes of commercial TiN NPs; (2) presence of a native oxide layer on the surface of TiN NPs, which causes broadening and red-shifting of plasmon peak [27], and (3) the bulk dielectric function of TiN, which was found to be sample dependent [41]. All this information points to the fact that TiN NPs deviate from ideal behavior in a greater extent than Au material.

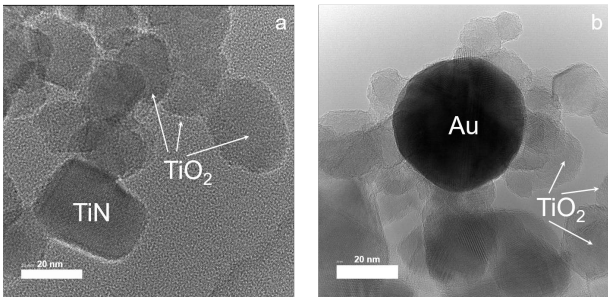

Fig. 15. TEM images of (a) TiN/TiO_2 and (b) Au/TiO_2 photocatalysts

Next, we probed the activities of the 30 nm TiN nanocubes incorporated into TiO_2 matrix for plasmon-mediated methanol oxidation reaction and compared them to the performance of the 50 nm Au spherical NPs.

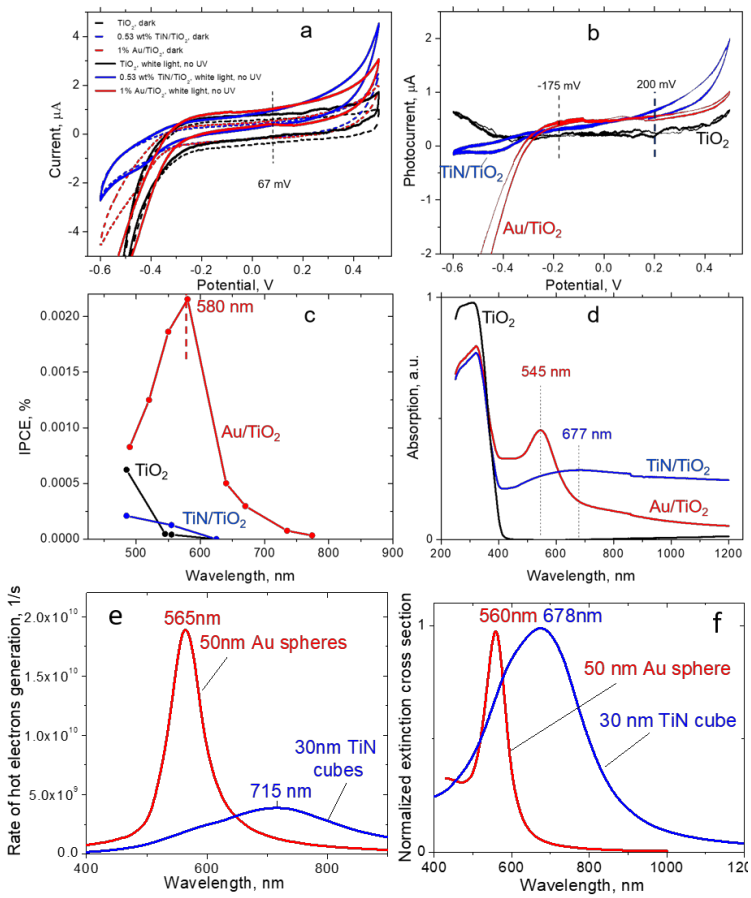

Fig. 16. (a) CV curves measured on thin films of 0.53 wt% TiN/TiO_2, 1 wt% Au/TiO_2 and TiO_2 in a solution of 0.5 M CH_3OH+0.1 M NaOH under exposure to broadband light with 425 nm cut off filter; 78 mW/cm^2; scan rate 10 mV/s; (b) Photocurrents vs potential (vs Ag/AgCl) derived from CV curves shown in Fig.5a; (c) IPCEs vs wavelength for methanol oxidation on thin films of 0.53 wt% TiN/TiO_2, 1 wt% Au/TiO_2, and TiO_2. (d) UV-Vis spectra of 0.53 wt% TiN/TiO_2, 1 wt% Au/TiO_2 and TiO_2 powders; (e) Computed rates of over-barrier hot electrons generation by 30 nm TiN cubes and 50 nm Au spheres; (f) Computed extinction cross sections for TiN/TiO_2 and Au/TiO_2 immersed in water.

First, the crystallography and distribution of metallic NPs within the semiconducting TiO_2 matrix for both photocatalysts (TiN/TiO_2 and Au/TiO_2) were analyzed using TEM. Figure 15 a shows a TEM micrograph of the TiN/TiO_2 NPs. The high resolution TEM (HRTEM) image shows that the interplanar spacing corresponds to the TiN and TiO_2 indicated by labels in Fig. 15 a. Similarly, a representative TEM micrograph corresponding to Au/TiO_2 is presented in Fig. 15 b. Individual TiN and Au NPs in these images are incorporated into the matrix of 10-30 nm TiO_2 support particles. Unlike TiN NPs, the Au NPs have a spherical shape, with diameters close to 50 nm. Analysis of multiple TEM images of Au/TiO2 powder suggests that the Au NPs are monodisperse with an average size of 50 ±2 nm. A close inspection of the TEM images in Fig. 15 b shows that the Au NP in this micrograph is in good contact with the TiO_2 support in multiple locations, which is essential for efficient injection of hot electrons into the TiO_2 support. In contrast, it appears that the TiN NP in Fig. 15a has fewer contact points with the TiO_2 support.

Cyclic voltammetry (CV) was used as a direct probe of TiN/TiO_2 and Au/TiO_2 activity for CH_3OH photoelectrochemical oxidation under exposure to broadband visible light (Figure 16a). Exposure to visible light (λ > 425 nm) leads to oxidative photocurrents for both photocatalysts as well as pure TiO_2 control (Fig. 16a). All of the CV curves, shown in Fig. 16a are rather featureless except for a small CH_3OH oxidation peak (*ca* 67 mV) observed on the Au/TiO_2 film during the cathodic sweep, which is due to the promotion of CH_3OH oxidation by Au NPs. The peak is small due to the low loading (1 wt%) of Au NPs on the TiO_2 support.

Photocurrents vs potential are compared for the three materials in Fig. 16b. Bare TiO_2 films produce a positive oxidation current in the entire potential region. The current remains constant in the potential region between -0.4 and 0.3 V, and slightly increases at potentials that exceed the equilibrium potential for water oxidation (0.25 V vs Ag/AgCl). Photocurrent enhancements vs. TiO_2 are observed for both TiN/TiO_2 and Au/TiO_2 films at potentials above *ca* -0.3 V; however, the photocurrent varies with potential in a different

manner for the two photocatalysts. While the shape of the photocurrent vs. potential curve of the Au/TiO_2 film mirrors that of TiO_2 (i.e. $I_{photo\_Au/TiO2} - I_{photo\_TiO2}$ does not depend on the potential at E > -0.2 V), it increases gradually with potential for the TiN/TiO_2 system from 0.25μA (-0.27 V) to 0.75 μA (0.25 V). The different behavior is likely due to a difference in the rate limiting steps for the overall photocatalytic reaction. For the TiN/TiO_2 interface, that forms an Ohmic junction[8], the reaction is likely limited by the separation of photogenerated charge carriers. Since there is no built-in barrier for separating electrons and holes, the applied bias aids in separating these carriers. A similar relationship between photocurrent and potential was reported for a slow electron-hole separation step in TiO_2 under UV excitation in the low potential region [42]. On the other hand, for the Au/TiO_2 interface, where hot electron-hole recombination is suppressed by a Schottky barrier, the rate-limiting step is likely the charge transfer at the photocatalyst/electrolyte interface. If CH_3OH oxidation under visible light proceeds via the same mechanism as when driven by UV light, the rate-limiting step should be the reaction of hydroxyl radicals from the TiO_2 surface with CH_3OH [42]. Due to a different trend in potential dependence of photocurrents, the photocurrent enhancement for TiN/TiO_2 vs Au/TiO_2 is also potential-dependent. TiN/TiO_2 outperforms Au/TiO_2 at potentials above 0.1 V. For instance, at 0.4 V, a 25% photocurrent enhancement is measured for TiN/TiO_2 vs Au/TiO_2. At this potential, CH_3OH oxidation occurs in parallel with oxygen evolution from water (OER, E^0=0.25 V). Superior performance of TiN/TiO_2 vs Au/TiO_2 for the OER (E>0.25V) has previously been reported [8].

To reveal the nature of photocurrent enhancement by plasmonic NPs, wavelength dependent photocurrents of CH_3OH oxidation were measured with and without applied bias on TiN/TiO_2, and Au/TiO_2 films. For measurements under applied bias, potentials of 0.2 and 0.4 V were selected because of superior performance of TiN/TiO_2 photocatalyst vs Au/TiO_2 (Fig. 16b) at these conditions. Fig. 16c shows IPCEs calculated from photocurrents measured on TiN/TiO_2, Au/TiO_2 and TiO_2 films when bias was not applied. The IPCE obtained for Au/TiO_2 films exhibits a notable wavelength dependence, which is in close agreement with the absorption spectrum of this catalyst, shown in Fig. 16d. This suggests that photoexcited electrons or holes, generated in the vicinity of the gold plasmonic resonance, are impacting the rate of CH_3OH oxidation. The maximum IPCE response (580 nm, Fig. 16c) is slightly red-shifted from that of the UV-Vis spectrum measured for the Au/TiO_2 powder (547 nm, Fig. 16d). This is in agreement with theoretical predictions of corresponding peak positions (565 and 560 nm for hot electron generation rate and absorption maximum of Au/TiO_2 in Fig. 16e and f, respectively), assuming that IPCE can be directly correlated to the rate of generation of over-barrier hot electrons. Red shifts between IPCEs and extinction spectra have been observed before by other researchers [8], and justified theoretically [43].

Interestingly, the theoretically predicted plasmon resonances for TiO_2-supported 50 nm Au and 30 nm TiN NPs in Fig. 16f are red-shifted compared to their NPs solution counterparts (Fig. 11f, e, respectively). This is due to a higher dielectric function of the TiO_2 support compared to water, resulting in screening the plasmonic fields. For Au NPs, a theoretically predicted red shift of 30 nm is in a relatively good agreement with the experimental value of 17 nm. For TiN NPs, a larger difference between the theory (*ca* 80 nm) and experiment (12 nm) is observed. A greater value of the theoretical red shift vs the experimental one is due to the fact that experimental Au and TiN NPs are not completely embedded into TiO_2 media, but exposed to H_2O as well.

From the theoretical results shown in Figures 16e, f, one can make a few important observations. Similar to what have been observed in Figures 11e, f, the calculated plasmon peaks of the TiN NPs incorporated in TiO_2 matrix are red-shifted and broadened in comparison to those of Au NPs. The production of hot electrons in 50 nm spherical Au NPs, as expected, is much more efficient than in 30 nm TiN cubes (Fig. 16e). This is due to the relatively large field enhancements generated by the former material which led Au to become the most commonly studied material in plasmonics. The TiN NPs, on the other hand, show a weaker and broader plasmonic response which are reflected in the predicted hot carrier generation rates.

Indeed, the TiN/TiO_2 films (Fig. 16c) exhibit a much weaker response to visible light in the course of photoelectrochemical CH_3OH oxidation compared to Au/TiO_2. However, in addition to lower rate of hot carrier generation, it can be due to hot electron-hole recombination at the interface that forms Ohmic junction.

We observe a significant increase in the photocurrent when positive bias is applied. For instance, under 780 nm irradiation, the TiN/TiO_2 film held at 0.2 V, produces an anodic photocurrent on the order of 50 nA. The IPCEs calculated for TiN/TiO_2 and TiO_2 films held at 0.2 and 0.4 V are shown in Fig. 17. All the IPCE vs wavelength curves shown in Fig. 17 have rising branches below 631 nm, and flat regions at $\lambda >$ 631 nm, in the area, where the TiN plasmonic resonance is observed (see Fig. 11b). Although IPCEs of TiN/TiO_2 films in this region grow vs TiO_2 as potential increases from 0.2 to 0.4 V, no wavelength dependence is observed. The lack of photocurrent enhancement due to the plasmonic effect may be due to (1) imperfections of the TiN/TiO_2 interface, outlined above, and (2) weaker and broader plasmonic resonances of 30 nm TiN NPs vs state-of-the-art 50 nm Au NPs, resulting in lower rates of hot carriers generation.

The major effect of visible light on IPCE in Fig. 17 is observed at $\lambda <$ 630 nm, i.e. in the region dominated by N(p) $\rightarrow$Ti(d) interband transitions in TiN NPs [8]. Theoretical analysis shows that the threshold energy for interband transitions in TiN NPs lies between 2.06 and 2.64 eV [44, 45] which corresponds to light in the 548-600 nm range. Interestingly, the effect is pronounced only when a potential is applied, with a strong correlation between the strength of the electric field and the IPCE at a given λ. When bias is not applied, the IPCE of the TiN/TiO_2 film is consistent with that of TiO_2, measured with and without applied bias. No significant effect of potential is observed on the IPCE of TiO_2 films at wavelengths between 490 and 631 nm. This is not surprising because sub-gap energy of 2.5 eV (corresponding to λ=490 nm) is insufficient to generate electron-hole pairs in P25 TiO_2 with 3.13±0.03 eV bandgap (based on analysis of Tauc plots [46]). The effect of the electrical field on the photocurrent can be justified by a better separation of holes and cold electrons, generated by interband transitions in TiN NPs. While holes are expected to drive the CH_3OH photooxidation reaction either directly by reacting with CH_3OH or hydroxyl ions adsorbed at the interface, cold electrons are presumably injected into the TiO_2 conduction band, prior to migration to the WE current collector. The presence of 1-2 nm TiO_2 native layer on the surface of TiN NPs is thought to facilitate migration of cold electrons to the TiO_2 matrix [8].

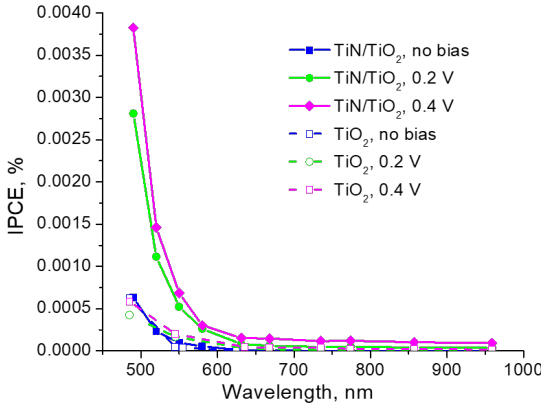

Fig. 17. IPCE vs wavelength for visible light-induced oxidation of CH_3OH on TiN/TiO_2 and TiO_2 films held at potential equal to OCP, 0.2 V and 0.4 V (vs Ag/AgCl) in aqueous solutions of 0.5 M CH_3OH+0.1 M NaOH.

Photoelectrochemical Oxidation Enhanced by Nitride Plasmonics

Refractory nitride plasmonics offer the potential to realize enhanced light-matter interactions for energy harvesting and photo-driven chemistry with materials systems that are thermally rugged, inexpensive, and potentially catalytic. In this portion of the work, we embedded commercial and in-house synthesized titanium nitride (TiN) nanoparticles into matrixes of titanium dioxide (TiO_2) and compared their ability to enhance electrochemical oxidation reactions to that of conventional gold (Au) nanoparticles. Figure 18a compares visible light absorption by Au, 30 nm TiN (PlasmaChem) and in-house produced TiN NPs. Although the photon-to-carrier conversion efficiencies were somewhat low (~10^{-4} %), the reaction rates were enhanced by a factor of 4 in the visible and near-infrared for both Au and TiN compared to a pure TiO_2 control, as shown in Figure 18b. Furthermore, TiN-embedded samples showed an order of magnitude improvement over Au in the near IR region. The spectral dependence of reaction rate enhancement followed the nanoparticle extinction spectra and a linear power-dependence identifies a photo-excited carrier mechanism (i.e., decaying plasmons excite carriers that participate in chemistry rather than heating of the system). Lastly, photo-induced transients of the electrochemical signal are consistent with interfacial defect charging in these heterosystems. Specifically, the TiN/TiO_2 system, which has no Schottky barriers, exhibits a bias-dependent and transient photoelectrochemical response, while the Au/TiO_2 system, which naturally forms a Schottky barrier that immediately separates charged carriers, exhibits a near-instantaneous response.

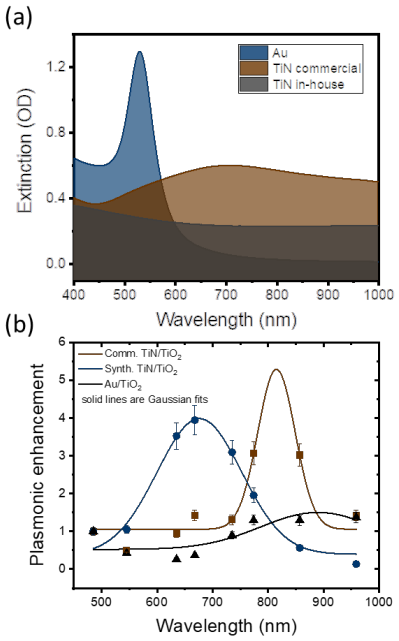

Fig. 18. (a) Extinction spectra (calculated as 1-transmission then converted to optical density, OD) of plasmonic nanoparticles in solution and (b) resulting plasmonic enhancement for methanol electro-oxidation for each nanoparticle system. In general, enhancements matched spectral response of the nanoparticle system.

Photoelectrochemical Methanol Oxidation under Visible and UV Excitation of TiO_2-supported TiN and ZrN Plasmonic Nanoparticles

Herein, both experimental and computational approaches are used in order to optimize the performance of TiO_2-supported TiN and ZrN NPs towards photoelectrochemical CH_3OH oxidation under visible excitation. Methanol photoelectrochemical oxidation was selected as a model reaction in this work. Prior to moving to more sophisticated reactions of plasmon-driven oxidation of large organic molecules, we attempted to confirm the feasibility of plasmon-driven photocatalysis by TiO_2-supported ZrN and TiN nanoparticles in a simple, well-characterized system. The choice of this redox reaction stems from its well-studied mechanism, the simplicity of identification of the three reaction products, and the fact that methanol is more easily oxidized than water. In our previous work [2], we compared TiN/TiO_2 and Au/TiO_2 photocatalysts in their activity for CH_3OH photoelectrochemical oxidation testing both visible and UV excitation. This chapter extends the analysis to ZrN/TiO_2.

Since the optical and photocatalytic properties of TiN and ZrN are highly dependent on their metallicity and defect structure, we use in-house synthesized ZrN NPs and characterize their optical, structural, and compositional properties prior to the evaluation of broadband visible- and visible + UV-excited CH_3OH photooxidation. Experimental data and theoretical simulations reveal mechanistic differences between TiN and ZrN photo-induced effects and reveal the roles of surface composition and agglomeration on the interaction between photogenerated carriers at the plasmonic NP/semiconductor interface.

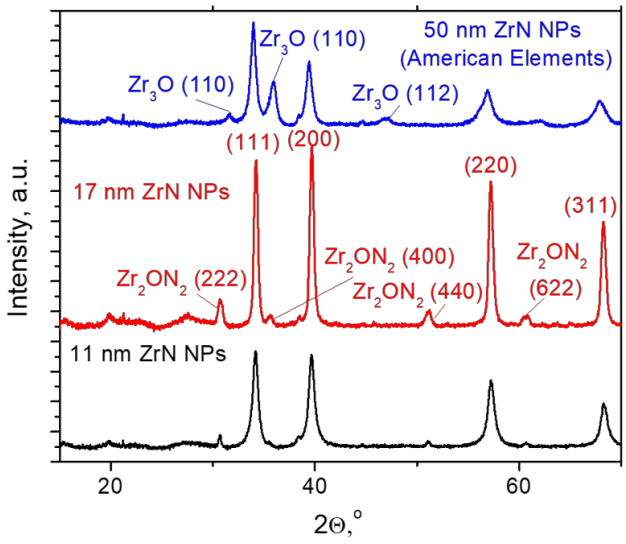

Fig. 19. PXRD patterns of 11nm, 17 nm, and commercial "50 nm" ZrN nanoparticles. ZrN (3-65-9415), Zr_2ON_2 (00-87-173), and Zr_3O (1-89-2339) JCPDF cards were used for reflections assignment.

First, crystal structure, composition, morphology, and optical properties of in-house synthesized ZrN powders were compared to those of a commercial material in order to select the best candidate for the photocalytic activity evaluation. Figure 19 shows PXRD patterns of the three materials: in-house synthesized ZrN NPs obtained by ammonolysis at 900 and 1050°C (black and red curves, respectively), and 50 nm commercial ZrN NPs. The PXRD patterns for the three materials are dominated by the cubic ZrN phase. In addition, minor contributions from cubic Zr_2ON_2 and hexagonal Zr_3O were observed in the diffraction patterns of the in-house and commercial materials, respectively. As expected, ZrN NPs synthesized at a lower temperature exhibit a smaller crystallite size (11 nm, Table 3) compared to the higher-temperature sample (17 nm). Surprisingly, the diffraction peaks for the nominally 50 nm commercially sourced ZrN NPs are broad and weak, suggesting a crystallite size smaller than the 50 nm size reported by the vendor. Indeed, analysis of the PXRD peak width yields a crystallite size of 14 nm.

Table 3. Surface elemental composition by XPS, BET surface area and crystallite size by PXRD for in-house synthesized and commercial ZrN nanoparticles.

	Zr	N	O	C	Zr/N ratio	BET surface area, m^2/g	Crystallite size by PXRD, nm
	at%						
In-house synthesized #1	38.0	14.4	38.8	8.8	2.6	16.8	11
In-house synthesized #2	18.7	15.5	31.0	34.8	1.2	9.6	17
50 nm ZrN (American Elements)	19.0	3.8	58.3	17.9	5	17.4	14

The crystallinity of ZrN NPs, along with their morphologies, was further evaluated by TEM analysis. Figure 20 shows that the in-house samples consist of particles with cubic and pseudo-spherical shapes. The crystallites appear fused together in chains and larger agglomerates, making it difficult to measure the size of individual crystallites. Measurement of the sample with PXRD-based crystallite size of 11 nm gave an average particle side length/diameter of 19.04 ± 6.60 nm, while the sample with 17 nm crystallites exhibits particles diameters of 23.56 ± 9.55 nm. These measurements are likely biased due to the smaller particles being obscured inside of the agglomerates. Sample crystallinity was visualized via high resolution TEM and selected area electron diffraction patterns. Lattice spacings for the 11 and 17 nm ZrN NPs were determined by analysis of the diffraction patterns shown in Fig. 20 (c and f), and are a good match to cubic ZrN with a lattice parameter of 0.456 nm, which is in agreement with the structure determined

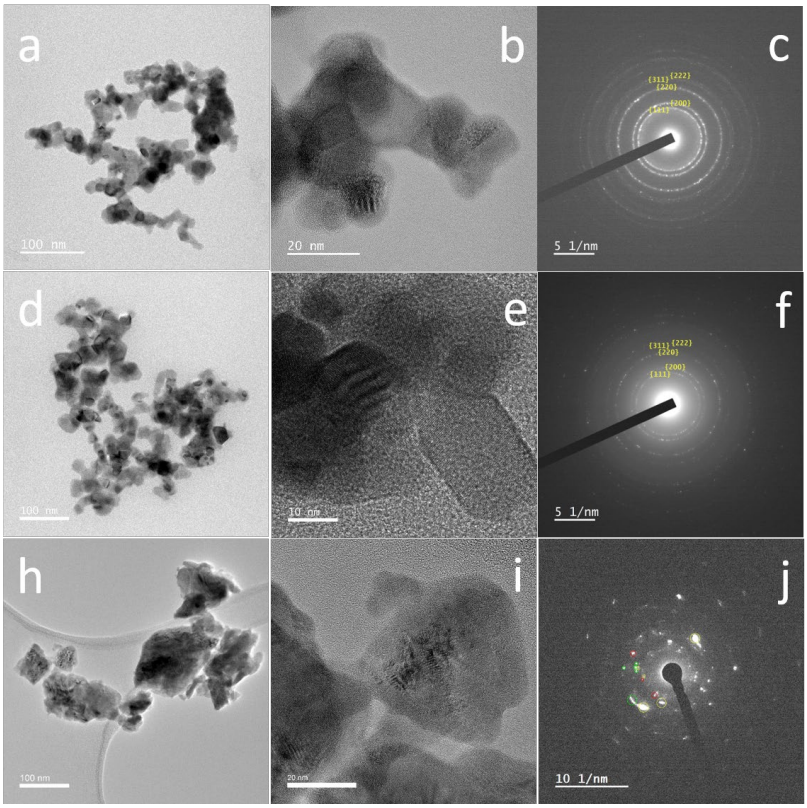

Fig. 20. TEM images and selected area electron diffraction patterns of (a-c) 11 nm ZrN; (d-f) 17 nm ZrN NPs and (h-j) 50 nm ZrN NPs. For c and f the diffraction rings are labeled by which family of cubic ZrN planes they correspond to. For j reflections are circled with green if they match a ZrN lattice spacing, red if they match Zr_3O, and yellow if they match both structures.

by XRD (Figure 19). Note the 1 nm shell around a larger NP in Fig. 20e that is likely evidence of the formation of an oxide layer on the surface of the ZrN NPs. Shells of between 1 and 3 nm were observed on the majority of particles imaged. This observation is consistent with the results of the XPS analysis (discussed below). Unlike the in-house synthesized ZrN NPs, the commercial ZrN NPs (Fig. 20h-i) have no well-defined shape. Their sizes range from 10 to 100 nm, and the crystallinity is not as well defined in comparison to the in-house synthesized NPs. While the diffraction patterns of the in-house produced particles (Fig. 20c, f) consist of rings due to the large number of randomly oriented, individual crystallites contained in the agglomerates being imaged, the diffraction image for the commercial material (Fig. 20j) is composed of non-uniformly distributed reflections. This may be due to the sampling of fewer crystallites that are mono- or nearly mono-crystalline (resulting in diffraction spots rather than rings) along with the strong presence of an oxide phase. The lattice spacings determined from the diffraction patterns match ZrN and Zr_3O, in good agreement with the PXRD.

One advantage, however, of the commercial NPs, is that they do not appear as agglomerated as the in-house produced NPs. This observation is supported by a surface areas measured for the samples via BET isotherms (see Table 3). The surface area of the commercial NPs exceeds both of the in-house samples despite its larger average particle size (as observed by TEM). The experimentally determined BET surface area for the commercial NPs, 17.4 m^2/g, is close to the theoretical expectation for 50 nm particles, 16.9 m^2/g. This suggests that the commercial ZrN NPs are well dispersed, and on average are smaller than 50 nm. For the in-house ZrN particles, we find the expected trend with the sample containing the smaller 11 nm crystallites exhibiting a higher surface area than the 17 nm NPs (16.8 vs 9.6 m^2/g, respectively). However, the experimental values are lower than expected for ideal 11 and 17 nm spheres (76.9 and 49.8 m^2/g, respectively). Agglomeration of the in-house synthesized particles likely reduces their available surface area.

The surface composition of the ZrN materials was analyzed by XPS (see Table 3 and Fig. 21). High resolution photoemission Zr3d core level spectra shown in Fig. 21 exhibit a complex shape with two (commercial ZrN NPs, Fig. 21a) or three (17 and 11 nm in-house NPs, Fig. 21b,c) peaks at 180, 182.3, and 184.8 eV. The spectra can be fit with two $3d_{5/2}$ and $3d_3/2$ lower and higher energy doublets corresponding to Zr-N and Zr-O bond energies, respectively [10]. The $3d_{5/2}$ component observed at 182.15 eV is close to 182 eV reported in Ref. [5] for Zr-O bond, and corresponding component at *ca.* 180 eV is specific for Zr-N bond. The FWHM of Zr-O peaks in Fig.21 (a-c) is broader than 1.4 eV measured for commercial ZrO_2 [5], which may indicate the presence of ZrO_xN_y. Comparison of the Zr3d spectra for three types of NPs shows, that the spectrum of commercial NPs lacks a peak at 180 eV, which suggests that for these NPs, the majority of the surface is oxidized. Although the 11 and 17 nm ZrN NPs are oxidized to a lesser extent, based on the fitting analysis *ca.* 70% of Zr atoms on the surface are bound to oxygen, and only 30% are involved in formation of Zr-N bond. To evaluate the contribution from Zr-O-N bonds [5], the N1s core level spectra were examined, which were fit with three components attributed to N-Zr (397.3 eV) peak, and lower and higher energy N-Zr-O peaks centered at 396.1 eV and ~400 eV [47], respectively, as shown in Fig. 21(d-f). Interestingly, the lower

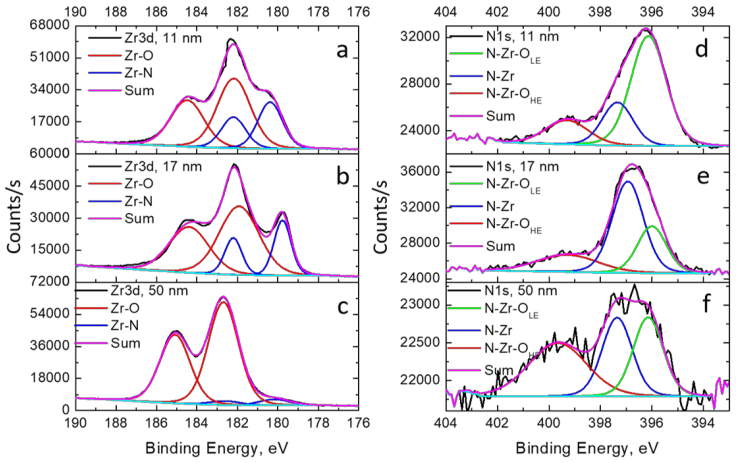

Fig. 21. High resolution photoemission Zr3d, and N1s core level spectra of 11 nm, 17 nm and 50 nm ZrN NPs. N-Zr-O_{LE} and N-Zr-O_{HE} denote lower and high energy N-Zr-O peaks, respectively.

energy N-Zr-O component in the spectrum of 11 nm ZrN NPs (Fig. 21d) has higher intensity than that of N-Zr indicating higher contribution of the former bonds on the surface. On the contrary, the contribution of N-Zr bonds prevails on the surface of 17 nm ZrN NPs. Although the intensity of the N1s feature for the commercial ZrN NPs is weak because of significant surface oxidation, both N-Zr and N-Zr-O components can be identified and quantified. As one would expect, oxynitride bonds prevail in the spectrum of the commercial NPs. The higher energy peak makes the greatest contribution in the N1s spectrum of commercial NPs as compared to the in-house made NPs. In agreement with fitting analysis, an analysis of the survey spectra shows that the lowest Zr/N ratio (or the greatest amount of ZrN on the surface) of 1.2 is measured for the 17 nm ZrN NPs, as compared to 2.6 and 5 for the 11 nm and commercial NPs, respectively (see Table 3).

Based on results from XPS and TEM analyses one can conclude that the extent of oxidation of the ZrN NPs increases in the following order: 17 nm NPs < 11 nm NPs < commercial NPs. This trend is not surprising when comparing 11nm and 17 nm ZrN NPs, since smaller nanoparticles should be more susceptible to oxidation. One would expect that the commercial NPs (nominally 50 nm) would be oxidized to a lesser extent as compared to the smaller 17 nm NPs. This unusual behavior possibly stems from the differences in methods used for their synthesis and processing.

The optical properties of ZrN NPs were characterized by UV-Vis spectroscopy. Extinction spectra of aqueous suspensions of the three materials (normalized to response at 350 nm) are shown in Fig. 22a. Broad maxima centered at 914 nm (or 1.36 eV, with 1.93 eV fwhm) and 600 nm (2.07 eV, with 1.28 eV FWHM) are observed for in-house 11 nm and commercial 50 nm NPs, respectively. The extinction response for the 17 nm NPs is somewhat different: instead of an absorption maximum it has a plateau at $\lambda > 600$ nm.

Electromagnetic modeling was used to determine whether the experimentally measured spectral features observed for ZrN NPs were consistent with those expected for ideal nanocubes. Simulations predict sharp LSPRs for the three materials (Fig. 22b), which shift to the red with increasing NP size. In addition, a broadening of the LSPR is expected as the size of the nanocubes increases from 17 to 50 nm. Surprisingly, the best agreement in terms of LSPR position is observed for the most oxidized, but the least agglomerated, commercial 50 nm ZrN NPs (experimental and computed peak positions differ by ~30 nm). However, the experimental LSPR is much broader, which is likely due to particle size polydispersity and oxidation.

The effect of surface oxidation was theoretically examined by modeling of extinctions of 11, 17, and 50 nm ZrN nanocubes in the presence of ZrO_2 shells. For simplicity, shells of the same 1.5 nm thickness were used for modeling of both 11 and 17 nm nanocubes. This is in agreement with the average oxide layer thickness obtained by TEM for in-house made 17 nm ZrN NPs. For 50 nm NPs, a 5 nm shell was envisioned based on XPS penetration depth (5 nm). The absence of a Zr-N feature in the Zr3d core level spectra in Fig. 22c suggests that the thickness of ZrO_2/ZrO_xN_y is equal to, or greater than, the XPS penetration depth. In agreement with the previous report [5], the presence of an oxide layer leads to LSPR broadening and red-shifting, as shown in Fig. 22 b. The thicker 5 nm oxide layer on 50 nm ZrN nanocubes produces stronger 80 nm red shift as compared to that of 11 and 17 nm NPs with 1.5 nm shells (71 and 54 nm, respectively). Considering the smaller ZrN NPs (11 nm and 17 nm), the calculated red shift is larger for the smallest size (11 nm) since the relative volume of the oxide shell is higher for this particle. Interestingly, after incorporating an oxide shell, a similar change in the FWHM is observed for three types of NPs (0.45 eV/0.6 eV for both 11 and 17 nm NPs before/after adding oxide shell vs 0.4 eV/0.55 eV for 50 nm NPs). Similar trends in the presence of an oxide layer have been observed for 8 nm ZrN nanoparticles synthesized by low-temperature plasma processing and attributed to the screening of the electromagnetic field by the ZrO_2 layer, which has a higher refractive index compared to air or H_2O [10]. Note that the 8 nm NPs were modeled as core-shell NPs with 1.24 nm ZrO_2 shell and a 4 nm mixed core comprising 90% ZrN and 10% ZrO_2. The effects of the oxide layer help in gaining an understanding as to why the rising branch of UV-Vis spectrum of the 11 nm NPs ($500 \text{ nm} < \lambda < 940$ nm) is red-shifted in comparison to the corresponding branch of the 17 nm NPs' spectrum ($425 \text{ nm} < \lambda < 660$ nm). Small NPs have greater susceptibility to oxidation as compared to larger NPs. To conclude, the presence of an oxide layer cannot fully explain the

absence of a plasmonic maximum for the 17 nm ZrN NPs. The reason may instead lie in the polydispersity of shapes and sizes of individual NPs and their significant agglomeration. It is known that the plasmon spectral position is very sensitive to the particle shape and aggregation [48].

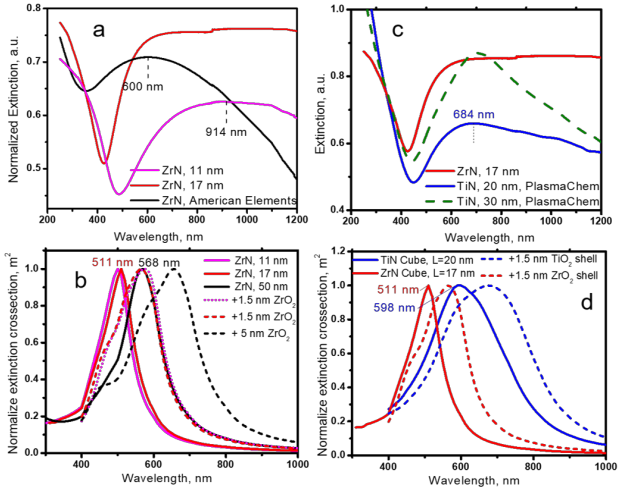

Fig. 22. (a) Normalized at 350 nm extinctions of in-house synthesized 11 and 17 nm ZrN NPs and ZrN NPs from American Elements dispersed in H_2O; (b) computed extinctions of 11, 17, and 50 nm ZrN nanocubes (solid lines) and the same materials surrounded by ZrO_2 shells (dashed lines) in H_2O; (c) normalized at 350 nm extinctions of 17 nm ZrN NPs, and commercial TiN NPs (20 and 30 nm); (d) computed extinctions of 17 nm ZrN vs. 20 nm TiN nanocubes (solid lines), and the same materials in the presence of 1.5 nm oxide shells (dashed lines); ε_0=1.8 (water).

In spite of the presence of a plateau instead of a sharp absorption maximum in the UV-Vis spectrum shown in Fig. 22, the 17 nm ZrN NPs were selected for their further photoelectrochemical evaluation due to their broad optical response (which may lead to a more efficient absorption over the entire visible range), more defined cubic morphology, and lower level of surface oxidation. Prior to electrochemical evaluation, the visible light absorption of the 17 nm ZrN NPs was compared to that of the 20 nm commercial TiN NPs (Plasma Chem) to obtain additional insights on the effect of NPs' surface oxidation, morphology and agglomeration on visible light absorption. The commercial 20 nm TiN NPs were extensively characterized in our previous work [2]. Surface oxidation of the two materials can be compared via analysis of high resolution core level Zr3d, Ti2p, N1s and O1s XPS spectra (Figs. 21 b, e and S1). Similar to the ZrN samples, the surface of the 20 nm TiN NPs is also oxidized. More detailed analysis by XPS points to a similar extent of surface oxidation for 17 nm ZrN vs 20 nm TiN NPs. As such, the red shift and the absence of a maximum in the extinction plot of 17 nm ZrN NPs are most likely related to the formation of fused/chained particles and/or the presence of the Zr_2ON_2 phase inside ZrN crystallites, rather than surface oxidation.

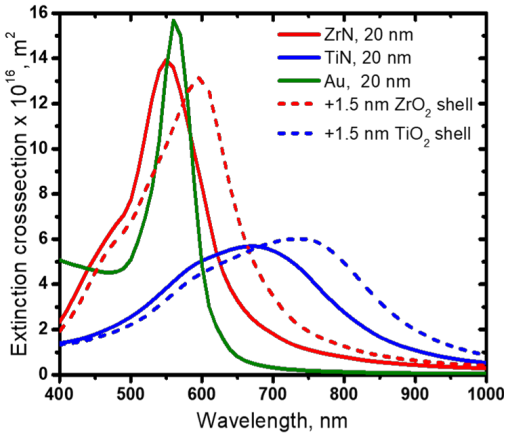

Fig. 23. Simulated extinctions for 20 nm ZrN, TiN and Au nanocubes (solid lines) incorporated into TiO_2 matrix. Dashed lines denote 20 nm ZrN and TiN nanocubes surrounded by 1.5 nm oxide shells; ε_0=2.5 (TiO_2 support).

To better understand the effect of the NPs' agglomeration and overall crystallite inhomogeneity on visible light absorption, we compared experimental and calculated extinction spectra of these materials (Fig. 22c, d). A better agreement between experimental and simulated extinction peak positions and widths is found for the less agglomerated, single phase commercial 20 nm TiN NPs. The morphology and agglomeration of the commercially sourced 20 nm TiN NPs was investigated in our previous work[2]. The optical extinctions of ZrN and TiN are asymmetric with extended broadening to the red. This is consistent with some degree of agglomeration, which forms long quasi-particles with red-shifted resonances along the long axis of the agglomerate. The simulated spectrum of ZrN NPs is shifted to higher energies vs that of TiN, which qualitatively agrees with the

experimental observations. The addition of 1.5 nm oxide shells to ZrN and TiN NPs does not change the arrangement of the extinction spectra. However, a larger LSPR red shift is predicted for oxidized TiN vs ZrN nanocubes (84 nm vs 54 nm, respectively).

Next, the effect of the TiO_2 matrix on the extinctions of 20 nm TiN and ZrN nanocubes was theoretically investigated. Figure 23 shows extinctions of TiO_2-supported TiN and ZrN nanocubes. Similar to the aqueous suspensions of ZrN and TiN nanocubes, a sharp blue-shifted LSPR maximum (red-shifted compared to LSPR in H_2O) is predicted for ZrN/TiO_2 vs TiN/TiO_2. For comparison, the optical properties of 20 nm Au nanocubes incorporated into a TiO_2 matrix are displayed in Fig. 23. One can see that ideal ZrN nanocubes exhibit optical properties comparable to strongly plasmonic Au. Including a 1.5 nm oxide shell leads to red-shifting of LSPR of ZrN/TiO_2 vs that of Au/TiO_2. Note the smaller predicted LSPR shift in the presence of TiO_2 matrix as compared to H_2O (47 nm vs 54 nm for oxidized 17 nm ZrN in TiO_2 matrix vs H_2O, and 69 nm vs 84 nm for oxidized 20 nm TiN NPs, respectively).

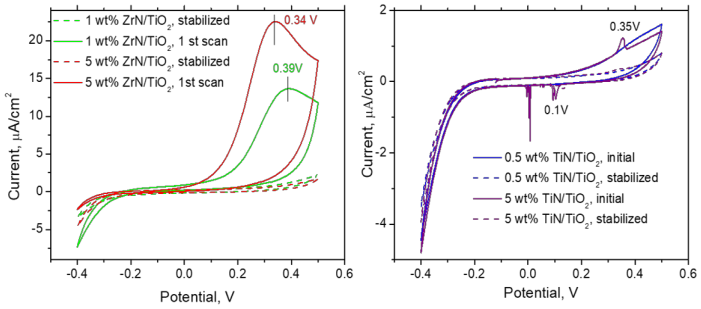

Fig. 24. CV curves of ZrN/TiO_2 and TiN/TiO_2 thin films recorded in aqueous solutions of 0.5M CH_3OH+0.1M KOH at a scan rate of 10 mV/s. Only fist and stabilized scans are shown.

Following optical characterization, the electrochemical stability of ZrN and TiN NPs incorporated into a TiO_2 NP matrix was characterized by cyclic voltammetry (CV). Here, 30 nm TiN NPs supported on TiO_2 were used as a baseline because of their superior optical performance (sharper and stronger LSPR, as shown in Fig. 22c) and a more pronounced cubic morphology compared to the 20 nm TiN NPs [2]. Figure 24 compares initial and stabilized CV curves recorded on ZrN/TiO_2 and TiN/TiO_2 films of two different loadings immersed in 0.5M CH_3OH+0.1M KOH aqueous solution. The initial CV curves measured on ZrN/TiO_2 films demonstrate strong loading-dependent oxidation peaks. After several successive cycles, the peaks vanish and the CV curves acquire a consistent shape at significantly lower currents on the order of 100 nA/cm^2. Because of the strong dependence of the initial currents on the ZrN loading, we presume that ZrN is oxidized to ZrN_xO_y and ZrO_2, which passivates the surface, thus protecting it from further oxidation. Although, to our knowledge, the electrochemical oxidation of ZrN nanoparticles has not previously been investigated, there are a few reports in the literature focused on electrochemical oxidation of ZrN films in phthalate buffer (pH=5) [47]. Careful XPS analysis of the film surface composition revealed that electrochemical oxidation occurred in two steps. In the first step, at potentials below 0.7 V vs standard hydrogen electrode (SHE), ZrN is oxidized to oxynitride/oxide mixture. At more positive potentials, oxide formation is coupled to evolution of molecular nitrogen which remains partially trapped within the oxide layer. The thickness of the ZrO_2 layer grew linearly with potential from *ca*. 0.1 V and 1.8 V. Oxidation of ZrN NPs in our experiments most likely falls in the second region, as it occurs at potentials more positive than 0 V vs Ag/AgCl or 0.99 V vs SHE.

Contrary to the performance of ZrN/TiO_2 films, no high anodic currents are observed during initial scans of the TiN/TiO_2 films of two different loadings. Instead, the current increases gradually at potentials more positive than 0.1 V in the same manner for both loadings. This observation confirms the higher resistance to oxidation of TiN nanoparticles, as compared to ZrN. The same trend was reported by Milosev at al.[49] for TiN films as compared to ZrN. However, at more positive potentials TiN films were found to be susceptible to electrochemical oxidation following the same mechanism as was outlined for ZrN.

Figure 25 shows the photocurrents generated by ZrN/TiO_2 and TiN/TiO_2 films of two different loadings under visible (Fig. 25a-c) and broadband visible + UV (Fig. 25d) excitation. The photocurrents of

the neat TiO_2 are included as a reference. Under visible illumination, both ZrN/TiO_2 and TiN/TiO_2 films exhibit photocurrents that exceed that of neat TiO_2, leading to the conclusion that ZrN and TiN NPs serve as photosensitizers for TiO_2. All photocurrents increase with increased potential due to enhanced photogenerated charge separation in the presence of an applied bias [8]. The presence of 1 wt% ZrN and 0.5 wt% TiN increase photocatalytic activity of neat TiO_2 at 0.2 V by a factor of 3 and 2.1, respectively. We suggest the photocatalytic activity observed for TiN/TiO_2 is likely due to interband transitions in TiN nanoparticles at $\lambda < 600$ nm [2]. The nature of photocurrent enhancement by ZrN NPs, however, is unlikely to be due to carriers generated within the ZrN (via intra- or interband transitions), since transport of this charge would be severely reduced due to the dielectric shell of ZrO_2, with a 5 eV bandgap [50], surrounding ZrN/ZrN_xO_y core. Instead, the photocurrent enhancement could be due to either (1) a photothermal effect [51] or (2) photooxidation of remaining ZrO_xN_y to ZrO_2. The efficiency of heat generation by plasmonic NPs, among other factors, depends on the NP shape [52]. Elongated shapes of fused/chained ZrN NPs (Fig. 2 d) may enhance photothermal efficiency, as nanoparticles with elongated morphology are known to be more efficient heat sources compared to spherical NPs [52]. The processes that presumably occur at the TiN/TiO_2 and ZrN/TiO_2 interfaces under visible excitation are illustrated in Fig. 26 a, b.

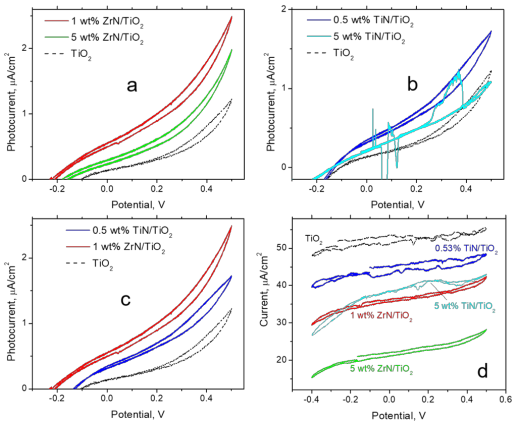

Fig. 25. Photocurrents measured on thin films of (a) 1 wt% and 5 wt% ZrN on TiO_2; (b) 0.5 wt% and 5 wt% TiN on TiO_2; (c) 0.5 wt% TiN/TiO_2 and 1 wt% ZrN/TiO_2; and (d) four materials under (a-c) visible and (d) combined visible + UV excitation in aqueous solutions of 0.5M CH_3OH+0.1M KOH at a scan rate of 10 mV/s. Photocurrents measured on TiO_2 films are shown as a reference. Scan rate 10 mV/s.

Another possible mechanism of photocurrent enhancement at the ZrN/TiO_2 interface may involve the photo-oxidation of ZrO_xN_y to ZrO_2. However, in this case one would expect to observe an increase in the photocurrent with an increase in ZrN loading (or surface area) but this contradicts the observed experimental trend (Fig. 25a). A decrease in photocurrent with an increase in loading is observed both for ZrN and TiN NPs (Fig. 25a, b). The effect of loading of plasmonic NPs on the photocatalyst performance has been extensively explored in the literature [19]. Typically, the optimal loading falls within the 1.5 – 2 wt% range. At higher loadings, plasmonic NPs can block TiO_2 active sites and/or serve as electron/hole recombination centers [19]. Both factors lead to a decrease in the efficiency of the photocatalytic processes. This may be the reason for the observed decrease in photocurrent with increase in ZrN and TiN loadings in our study. At lower loadings (1 wt% ZrN, 0.5 wt % TiN NPs), the photocurrent generated by ZrN/TiO_2 is greater than that of TiN/TiO_2, (Fig. 25c). However, because of the differences in the loadings, morphology, and surface oxidation conditions of TiN and ZrN NPs, it is difficult to elucidate the reason for the superior performance of ZrN/TiO_2 photocatalyst.

To obtain additional information on the interaction of metallic NPs and the semiconductor in the hybrid photocatalysts, the effect of UV light on their photocatalytic activities was examined. Photocurrents generated by ZrN/TiO_2 and TiN/TiO_2 films illuminated by broadband visible + UV light are shown in Fig. 25d. The greatest photocurrent is observed for neat TiO_2 films, while ZrN and TiN NPs cause photocurrent inhibition, which becomes more pronounced at higher NPs loadings. Interestingly, this trend is opposite to that observed under visible excitation (Fig. 25 a-c). We discuss below the processes occurring at the plasmonic NP/semiconductor interface under UV + visible excitations to find an underlying mechanistic rationale. Because the photon energies utilized in our visible + UV experiments (1.24 to 3.45 eV or 1000 to 360 nm) extend beyond the bandgap of TiO_2 (3.13 ±0.03 eV), band to band generation of electrons and holes in the semiconductor occurs and could dominate the photocatalytic process. Metallic NPs with Fermi energies below the conduction band of the semiconductor (e.g. Au) may serve as a sink for photogenerated

electrons generated in the TiO_2 [19]. This may lead to a current decrease if electrons become trapped inside metallic NPs and are thus eliminated from photocatalytic process [53]. However, the flow of photogenerated electrons from the TiO_2 conduction band to metallic NPs under UV excitation may be counterbalanced by an opposite flow of hot electrons generated by plasmonic NPs under visible excitation. Thus, plasmonic NPs that form a Schottky barrier with TiO_2 are expected to inhibit current either due to promotion of electron-hole recombination or the trapping of photoelectrons [19]. The former mechanism does not apply to TiN NPs incorporated into a TiO_2 matrix because of the absence of a Schottky barrier at the TiN/TiO_2 interface [8]. However, TiN NPs can serve as traps for both photogenerated electrons and holes, as shown in Fig. 26 c. Although ZrN NPs may form a Schottky barrier with TiO_2 (E_F=4.41 eV vs 4.0 eV for TiN) [9], migration of photogenerated electrons to/from ZrN NPs and TiO_2 is inhibited (or forbidden) in the presence of a mixed/dielectric oxide layer (Fig. 26 d). Therefore, the recombination mechanism is not applicable to the ZrN/TiO_2 interface. Instead, it is proposed that photoexcited electrons from the TiO_2 conduction band can be trapped by surface defects in TiO_2, assuming that such defects were formed while incorporating the ZrN NPs into the TiO_2 matrix. Finally, both TiN and ZrN NPs can inhibit TiO_2 photocatalytic activity by blocking TiO_2 active sites. The last effect likely plays an important role in the inhibition of TiO_2 photocatalytic activity under combined visible + UV excitation, as this effect leads to the inhibition of TiO_2 activity with an increase in loading of ZrN and TiN NPs in the same manner as shown in Fig. 25d.

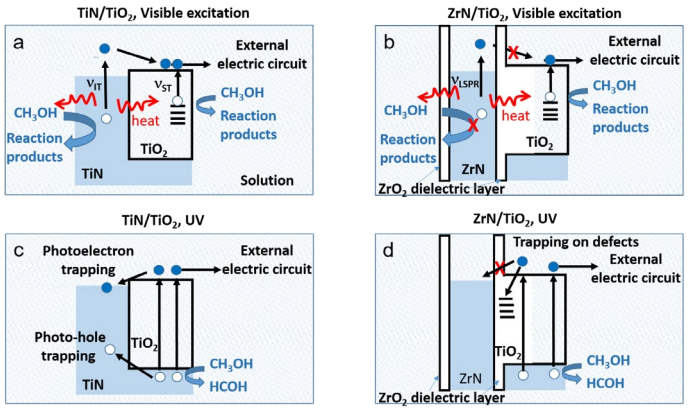

Fig. 26. Illustration of processes occurring at the (a,c) TiN/TiO_2 and (b,d) ZrN/TiO_2 interfaces under (a, b) visible and (c, d) UV excitations. (a) Photogenerated by interband transitions in TiN NPs (IT) cold electrons migrate to external electrical circuit after being injected into TiO_2 conduction band. Holes drives CH_3OH oxidation either directly reacting with CH_3OH molecules or indirectly via OH radicals. Localized heat produced by photoexcitation, can also promote reaction rate. In parallel, photoexcited electrons from TiO_2 trapped states migrate to external electric circuit, while holes drives CH_3OH oxidation. (b) Photogenerated electrons and holes at LSPR frequencies are excluded from the photoelectrochemical process. Only localized heat can promote reaction rate. (c) Photogenerated holes in TiO_2 valence band drive CH_3OH oxidation under UV excitation. Photoexcited electrons and photo-holes can be trapped by TiN leading to photocurrent inhibition. (d) Contrary to (c), photoexcited electrons from TiO_2 conduction band can be trapped only on TiO_2 defects

TiN/Semiconductor Interface Design

The unique combination of optical, electrical, and refractory properties of refractory nitrides has led to use in resonant optical applications where thermal stability enables entirely new applications such as photothermal transducers. TiN, in particular, has attracted attention owing to optical properties that can closely mimic those of elemental gold and a composition that make it potentially compatible for contacts on semiconducting nitrides.

Important work has been carried out evaluating the interfacial properties in TiN/GaN systems as a function of multicomponent layer composition, annealing conditions, and semiconductor doping. Results have indicated that either pure Ti or TiN can form ohmic contacts to n-GaN, aided by the similarity in their work function and electron affinity, but that the details of specific resistance and interfacial composition depend on annealing conditions and the heterolayer film structure. On the other hand, TiN does not form an ohmic contact to p-GaN, likely due to band alignment issues. Obviously, rectifying or ohmic responses are critical to charge transport in electronic and optoelectronic devices. Similarly, while it has long been appreciated that interfacing a plasmonic resonator with a semiconductor can result in enhanced lifetime and collection of electrons and holes generated via plasmon decay, the electronic structure of a metal/semiconductor interface can dictate this charge separation and collection efficiency. TiN plays a unique role in this context. Since its optical response can resemble that of gold's, one can implement a variety of plasmonic structures (cubes, disks, ridges, planar films) that offer optical response comparable to that of gold and the temperature and physical robustness of a refractory material. This combination has made TiN an appealing candidate for photothermal applications or technologies that require large amounts of inexpensive plasmonic material.

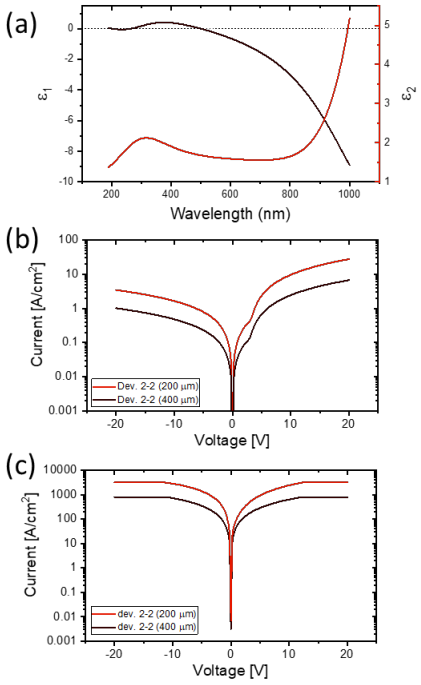

Fig. 27. (a) Measured optical response of sputtered TiN on GaN. These optical properties allow for prediction of plasmonic resonances. (b) and (c) show current-voltage response of TiN contacts on p- and n-type GaN, respectively and demonstrate rectifying behavior for the p-type sample and an ohmic contact on n-GaN. Schottky barrier measurements is a courtesy of Dr. S. Maximenko, Code 6818. 100 nm TiN films were prepared by magnetron sputtering by Prof. V. Shalaev's group from Purdue University, IN

It is with these qualities, challenges, and potential applications in mind that we examined the optical response and Schottky barrier properties of the TiN/GaN interface for both p- and n-doped GaN and without any post-deposition annealing. All of these characteristics play important roles in plasmonically-enhanced photocarrier generation and collection. We found that TiN sputtered on both n- and p-type GaN displayed the desired optical properties for plasmonic applications (see Fig. 27a). While this is a positive result indicting the possible use of GaN as a collector of plasmonically generated hot carriers, the interfacial properties produced two very different conditions. On p-type GaN, a distinct Schottky barrier was formed with a barrier height of ~0.5 eV which will enable effective separation between photogenerated electrons and holes. On the other hand, no barrier was found for TiN on n-GaN (see Fig. 27b, c). While the lack of carrier separation in this system will likely reduce hot carrier collection efficiencies, it enables a bias-dependent response whereby charges of a desired type (e.g., electrons) could be directed to transport into the semiconductor or remain in the plasmonic material. The specific application of interest would determine which condition is most desirable.

Visible Light Driven Oxidation of Harmful 2-Chloroethyl Ethyl Sulfide Using Other Nitride Materials

Additional nitride materials have been considered for potential application of visible light driven oxidation of 2-chloroethyl ethyl sulfide (2-CEES). Four TiN-GaN materials were assessed to determine capability of visible light driven oxidation reactivity. Each material was assessed for 24 hours under visible light illumination with corresponding control samples kept in the dark. An overlay of the 2-CEES peak in the chromatographs for both light and dark are shown in Fig. 28 below.

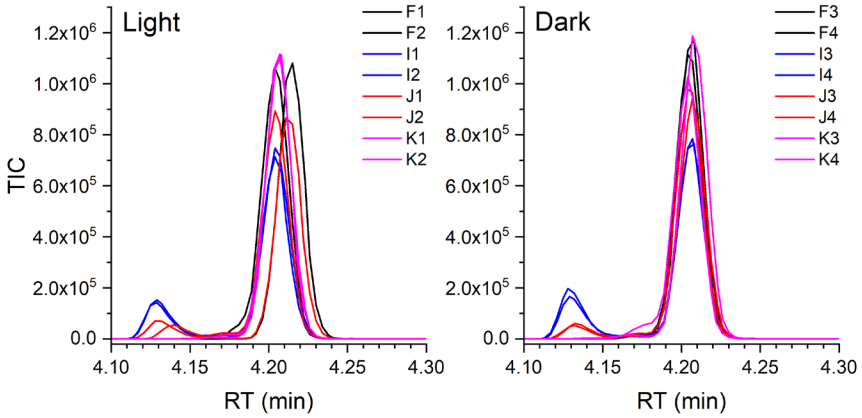

Fig. 28 — Chromatographic analysis of the 2-CEES peak from TiN-GaN materials challenges.

The GC-MS analysis shows that 2-CEES (Retention time (RT) – 4.2 min) is the major chemical species found within the extract from the 24-hour challenges. An additional peak centered at RT 4.13 min for materials I and J is indicative of C-Cl hydrolysis to give 2-ethylthio ethanol as a minor byproduct. Analysis of the chromatographs in the RT region from 6.0 to 9.0 min (Fig. 29) reveals formation of minor concentration of the sulfoxide oxidation byproduct at a RT of 8.8 min for the TiN-GaN materials F and K. Additional hydrolysis byproduct 1,2-bis(ethylthio) ethane was also observed at a RT of 8.3 min. Overall, minimal reactivity with the TiN-GaN materials was observed over 24 hours. However, two different reactivity routes were observed and were selective based upon the materials utilized. TiN-GaN materials I and J appear to promote hydrolysis while materials F and K appear to promote oxidation reactivity.

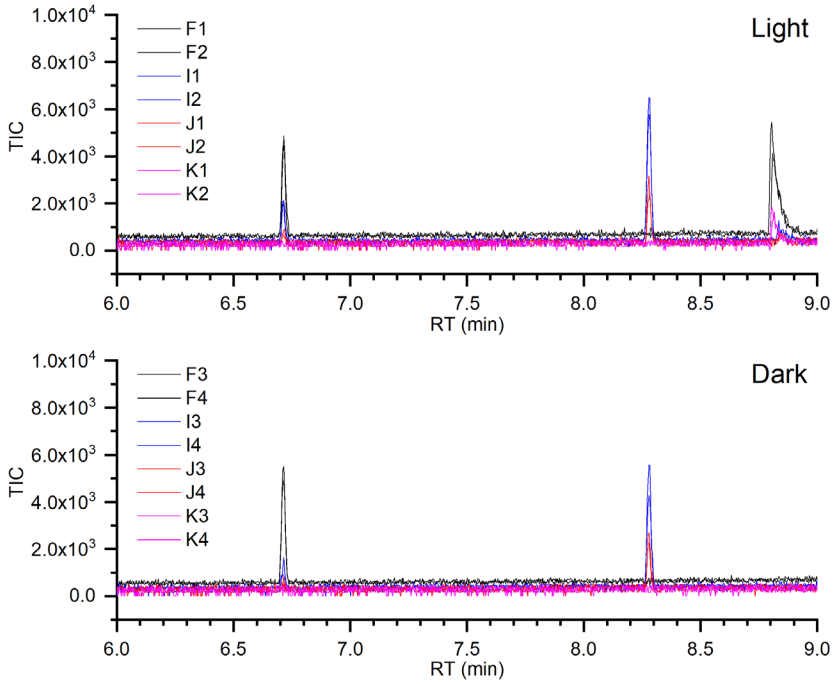

Fig. 29 — Chromatographic analysis for oxidation byproduct peaks from TiN-GaN materials challenges.

Additional TiN-oxide materials were also assessed for their photochemical reactivity with 2-CEES. TiN supported on ZnO, amorphous TiO_2 and NiO were assessed. The assessment of the TiN/ZnO material is shown in Fig. 30 below. The major reaction pathway observed was the hydrolysis of the C-Cl bond to generate 2-ethylthio ethanol under both light and dark conditions with minor formation of 1,2-bis(ethylthio) ethane. When the TiN/ZnO samples were exposed to visible light, a minor amount of oxidation byproduct diethyl disulfide is potentially formed and co-elutes with 2-ethylthio ethanol altering the mass fragmentation pattern observed for the peak at RT 3.704 min (Fig. 30).

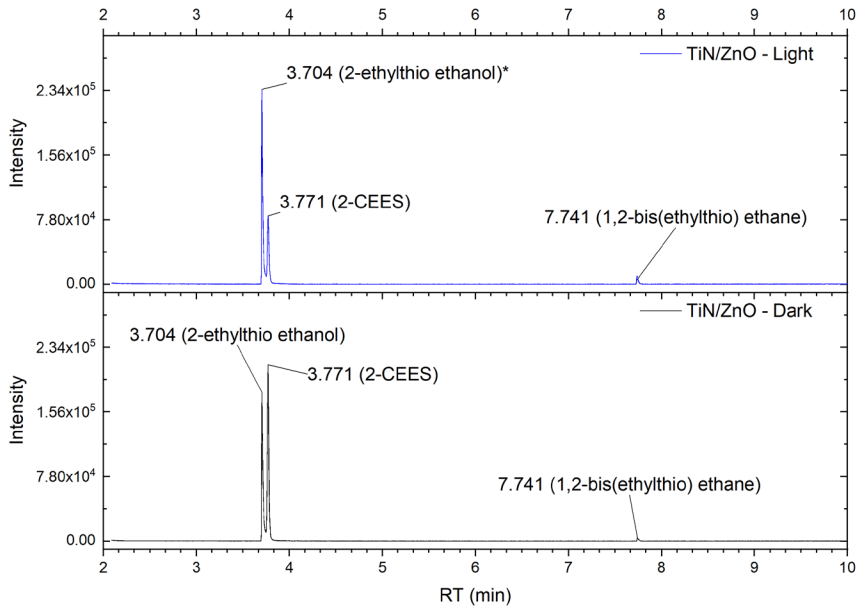

Fig. 30 — Chromatographic analysis for oxidation byproduct peaks from TiN-ZnO materials challenges.

The head to tail comparison of the mass fragmentation patters from the peak at RT 3.704 min for the samples TiN/ZnO exposed to light and when kept in the dark is shown in Fig. 31 below. The minor additional fragments with m/z of 122, 94, and 66 indicate the potential co-elution of diethyl disulfide, which is not observed in the mass fragmentation patterns for the same peak when the material was kept in the dark. The formation of diethyl disulfide corresponds to the potential cleavage of a C-S bond via the oxidation route described in the literature [54].

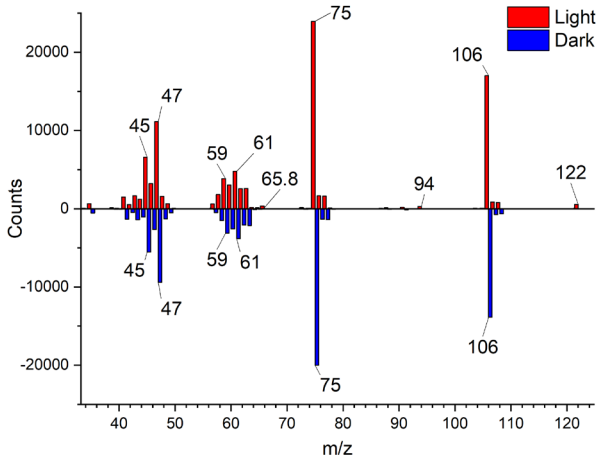

Fig. 31 — Head to tail analysis of mass fragmentation patters of the byproduct peak (RT 3.704 min) from TiN-ZnO materials challenges.

Analysis TiN on amorphous TiO_2 was also consistent with directing the reactivity of 2-CEES toward hydrolysis of the C-Cl bond to form 2-ethylthio ethanol regardless of the exposure conditions. Chromatographic analysis of the TiN/amorphous TiO_2 are shown in Fig. 32 below show no indication of photochemical driven oxidation.

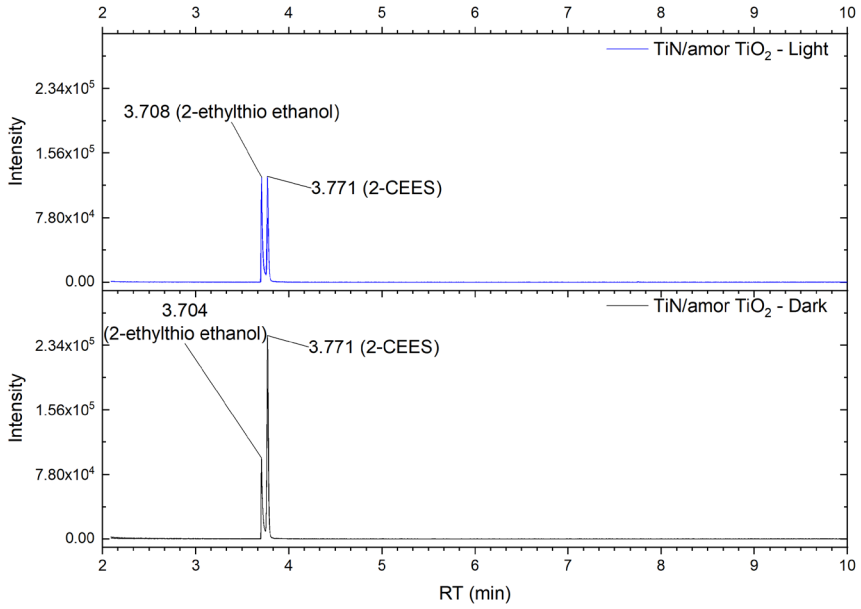

Fig. 32 — Chromatographic analysis for oxidation byproduct peaks from TiN-amorphous TiO_2 materials challenges.

Altering the TiN oxide support to NiO showed minor improvement into the hydrolysis of the C-Cl bond of 2-CEES and the potential formation to diethyl disulfide however 2-CEES was still a major

component of the extract as shown in the GC-MS chromatographs in Fig. 33. The incorporation of NiO as the support for TiN did promote the minor formation of diethyl disulfide even when the material was not exposed to visible light, which potentially indicates a different oxidation pathway for the NiO material.

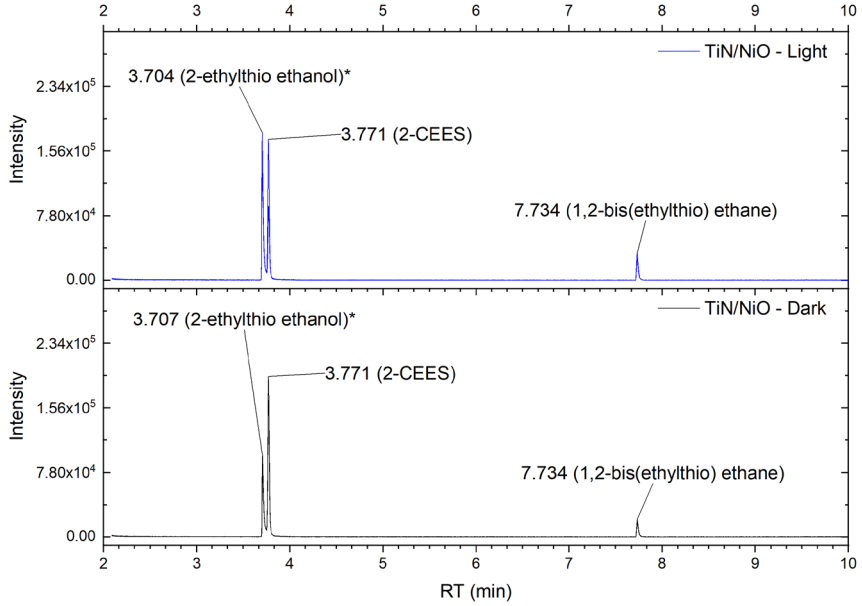

Fig. 33 — Chromatographic analysis for oxidation byproduct peaks from TiN-NiO materials challenges.

Alternative nitride samples Mo_2N, NbN/Al_2O_3, and ZrN/TiO_2 were also assessed to determine the potential photochemical driven reactivity with surface residing 2-CEES. Unfortunately, photochemical oxidation was not observed to be the major reaction pathway for the three samples. Analysis of Mo_2N extraction appeared to show no reactivity based upon the only product within the chromatographs being that of 2-CEES (Fig. 34).

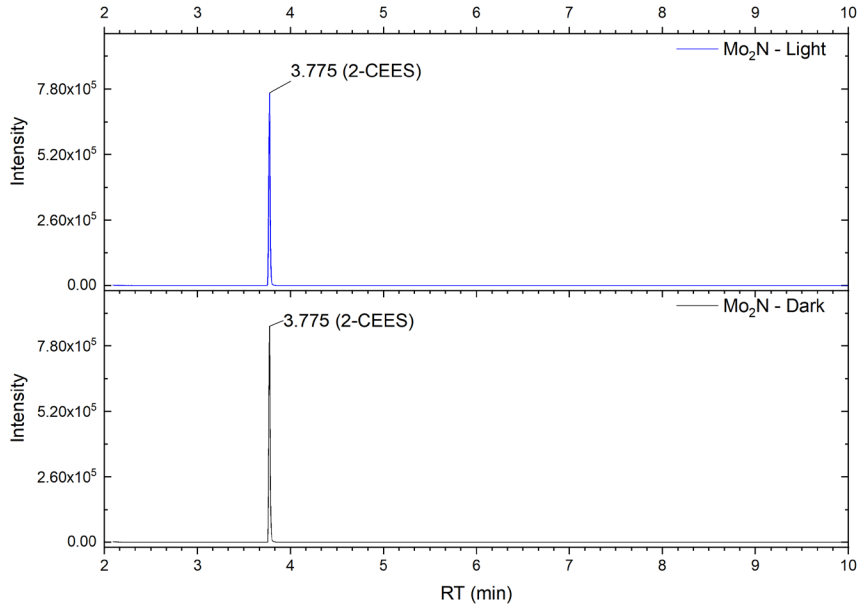

Fig. 34 — Chromatographic analysis for oxidation byproduct peaks from Mo_2N materials challenges.

The NbN/Al_2O_3 material appears to display the most promising reactivity toward 2-CEES with hydrolysis of most of the deposited 2-CEES over 24 hours. This reactivity however appears to occur when the samples are kept in the dark as well and no oxidation was observed (Fig. 35).

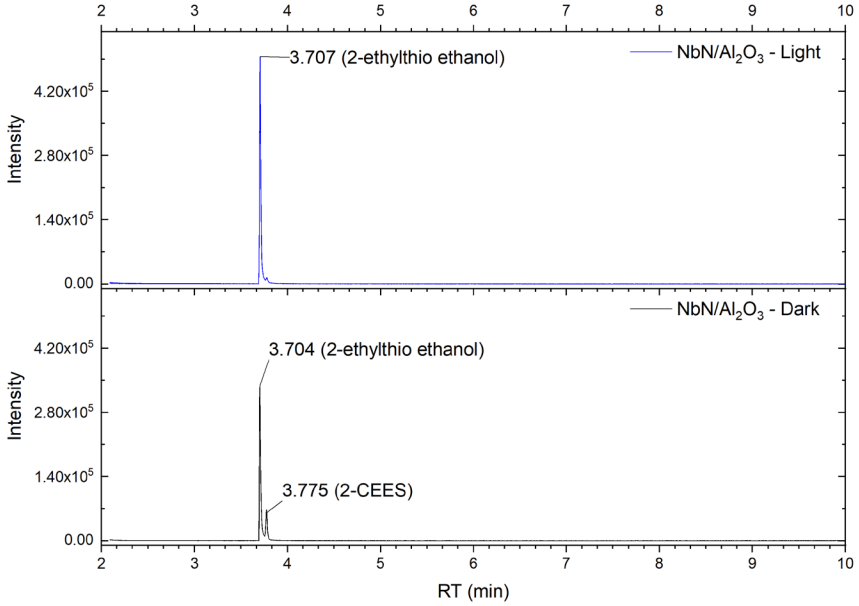

Fig. 35 — Chromatographic analysis for oxidation byproduct peaks from $NbN\text{-}Al_2O_3$ materials challenges.

The final sample assessed was that of ZrN supported onto TiO_2. The analysis shows that the major component extracted from the surface was 2-CEES with minor hydrolysis occurring in both the light and dark samples (Fig. 36). Additionally when exposed to visible light the potential formation of diethyl disulfide was observed however, both byproducts were minor in comparison to the extracted 2-CEES.

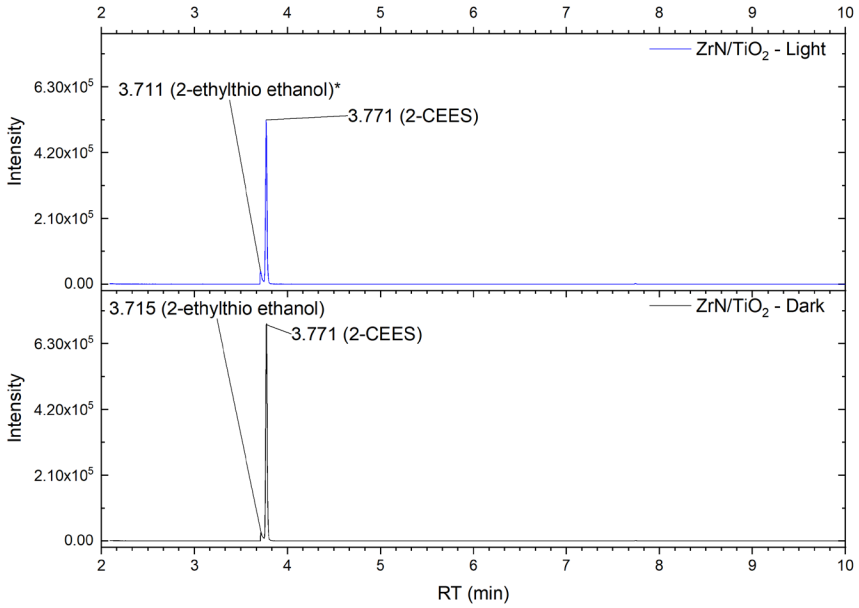

Fig. 36 — Chromatographic analysis for oxidation byproduct peaks from $ZrN\text{-}TiO_2$ materials challenges.

Visible Light Driven Oxidation of Harmful 2-Chloroethyl Ethyl Sulfide Using SiO_2-TiO_2 Composite Particles and Air

A demonstration of visible light driven aerobic oxidation of 2-chloroethyl ethyl sulfide (2-CEES) using rationally designed hybrid nanostructures has been performed. The hybrid nanostructures were composed of 5 nm TiO_2 nanoparticles or TiO_2 nanosheets supported onto monodispersed SiO_2 Stöber spheres. Excitation of the nanostructures with visible light (λ>400 nm) resulted in oxidation of the thioether sulfur of 2-CEES. The highest reaction rate of 56.2 µmol/g/h (quantum yield of $1.64x10^{-5}$ molecules/photon) was obtained for the SiO_2-TiO_2 5 nm composite in comparison to 16.5 µmol/g/h ($1.20x10^{-5}$ molecules/photon) for the SiO_2-TiO_2 NS composite. Experimental observations combined with modeling revealed that the reactivity of TiO_2 nanostructures is due to surface defects and states. Supporting the TiO_2 nanoparticles onto the SiO_2 Stöber spheres promotes the homogenous distribution of TiO_2 nanoparticles allowing most of the active surface to remain available.

Fig 37 below illustrates the general scheme for the generation of the hybrid nanostructures. Mono dispersed silica particles with an average particle size of 421.57 ± 10.83 nm were first decorated with a layer of cationic polyelectrolyte, poly(allylamine hydrochloride) (PAH) via electrostatic interaction with the negatively charged native silica spheres synthesized via the Stöber method [55]. After adsorption of PAH the surface charge of the silica particles was positive. Following PAH adsorption, the controlled deposition of negative charge 5 nm TiO_2 nanoparticles or TiO_2 nanosheets onto the surface of the positively charged SiO_2-PAH composites was carried out to give the resultant composites shown in Fig. 37c and d.

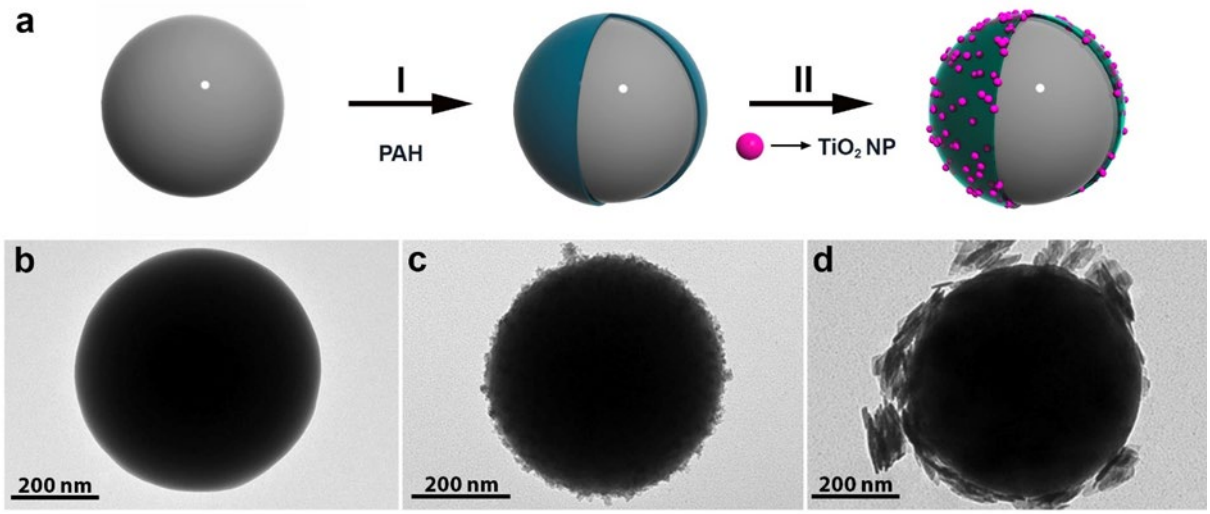

Fig. 37 — Synthesis strategy schematic for the SiO_2-TiO_2 composites (a). Representative TEM images of, synthesized colloidal SiO_2 articles (b), SiO_2-coated with -5nm TiO_2 NP (c) and TiO_2 NS.

Analysis of 2-CEES challenges for the composite materials and corresponding neat TiO_2 particles are shown in Fig. 38 and 39. Reduction of the 2-CEES peak is clearly shown when the composites and the neat TiO_2 nanoparticles are exposed to visible light. Additionally, byproducts of thioether sulfur oxidation were readily observed in the chromatographs in addition to the reduction in the concentration of 2-CEES. Note the retention time changes for 2-CEES and the oxidation products are due to capillary column length changes and instrument maintenance. The observation of oxidation at the thioether sulfur in Fig. 38 and 39

with visible light is different from what has been previously reported for UV promoted oxidation with TiO_2 materials [54, 56].

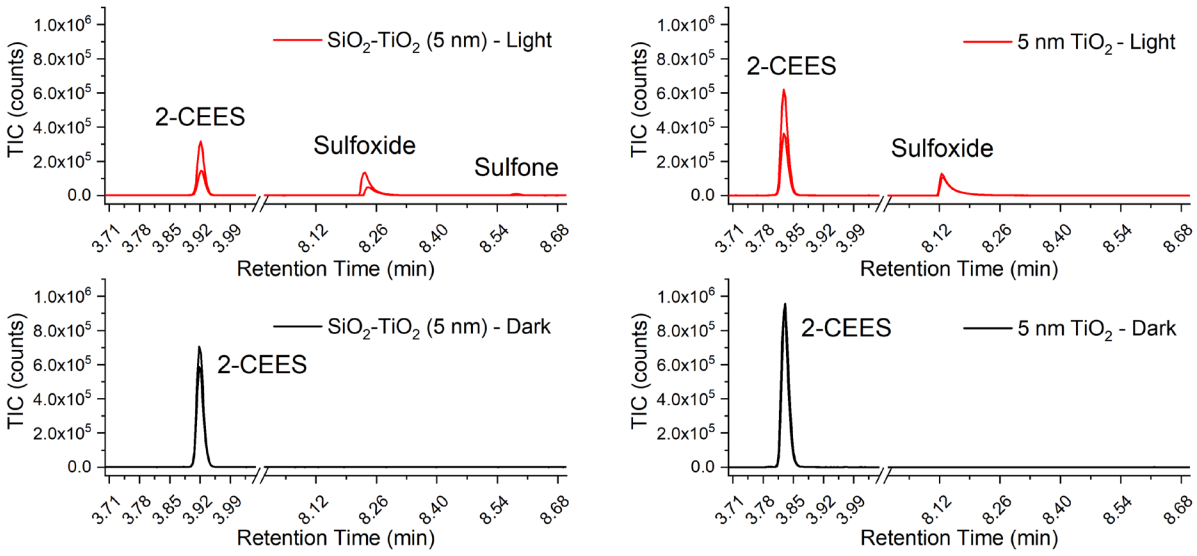

Fig. 38 — GC-MS chromatographs of the SiO_2-TiO_2 (5 nm) composite materials (left column) and neat 5 nm TiO_2 (right column) with exposure to light (top, blue) or kept in the dark (bottom, black) challenged with 2-CEES. Photoactive composite loading was 10 wt% 5 nm TiO_2 /SiO_2 (0.4mg TiO_2 in the film) and 3 mg of neat 5 nm TiO_2 with deposition of 25 µL of 2-CEES stock solution. Reactions were performed at room temperature for 24 hours post CH_2Cl_2 solvent evaporation.

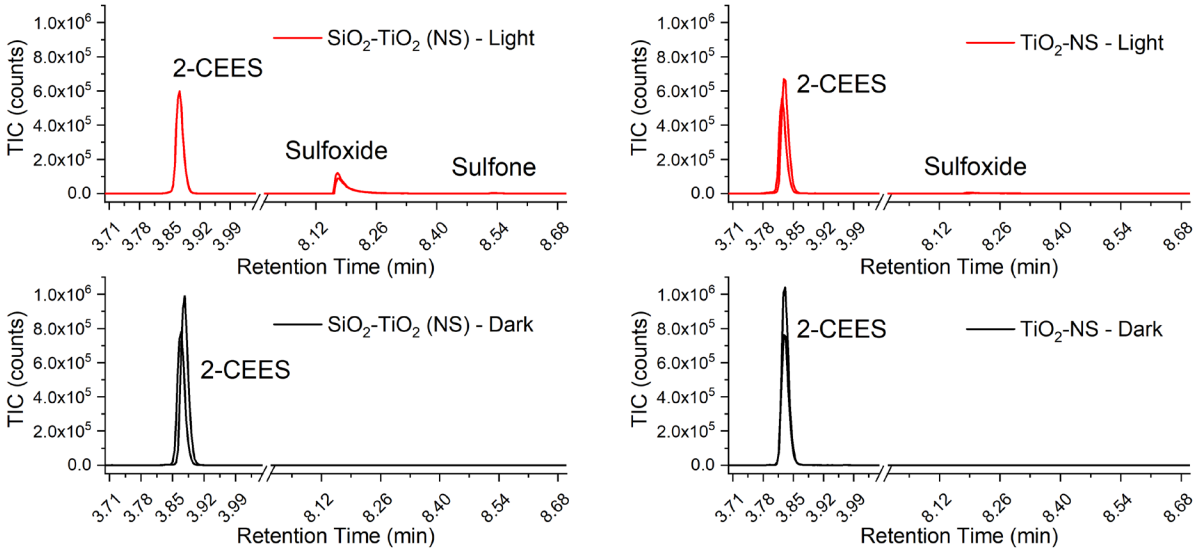

Fig. 39 — GC-MS chromatographs of the SiO_2-TiO_2 (NS) composite materials (left column) and neat TiO_2 NS (right column) with exposure to light (top, blue) or kept in the dark (bottom, black) challenged with 2-CEES. Photoactive composite loading was 30 wt% TiO_2 NS/SiO_2 (1 mg TiO_2 in the film) and 3 mg of neat TiO_2 NS with deposition of 25 µL of 2-CEES stock solution. Reactions were performed at room temperature for 24 hours post CH_2Cl_2 solvent evaporation.

The 2-CEES concentration from the replicate samples for the four materials are shown in Table 4. The concentration of 2-CEES was reduced by 57.8% and 30.5% for the SiO_2-TiO_2 (5 nm) and SiO_2-TiO_2 (NS), respectively, in comparison to the control samples kept in the dark. Percent reductions of 44.5% and 30.1% for the neat 5 nm TiO_2 nanoparticles and TiO_2 nanosheets in comparison to the control samples were observed respectively. The performance differences between the 5 nm TiO_2 nanoparticles in comparison to the TiO_2 nanosheets is believed to be due to the 5 nm-TiO_2 having more defects per one TiO_2 molecule as compared to the case of TiO_2 nanosheets. Similar percent reductions observed from integration of the 2-CEES peak do not take into account the catalyst loading and surface area therefore additional analysis and comparison of the photocatalytic behavior was performed.

Table 4. 2-CEES challenge results for the two SiO_2-TiO_2 composite samples and the corresponding neat TiO_2 particles

	SiO_2-TiO_2 (5 nm) (mol)	**TiO_2 (5 nm) (mol)**	**SiO_2-TiO_2 (NS) (mol)**	**TiO_2 (NS) (mol)**
Light	2.90×10^{-7}	9.18×10^{-7}	9.07×10^{-7}	8.38×10^{-7}
Light	4.98×10^{-7}	5.69×10^{-7}	9.01×10^{-7}	1.00×10^{-6}
Average	*3.94×10^{-7}*	*7.44 x 10-7*	*9.04×10^{-7}*	*9.20×10^{-7}*
(Stdev)	*(1.47×10^{-7})*	*(2.47×10^{-7})*	*(4.44×10^{-9})*	*(1.15×10^{-7})*
Dark	1.01×10^{-6}	1.32×10^{-6}	1.17×10^{-6}	1.48×10^{-6}
Dark	8.53×10^{-7}	1.36×10^{-6}	1.43×10^{-6}	1.15×10^{-6}
Average	*9.34×10^{-7}*	*1.34×10^{-6}*	*1.30×10^{-6}*	*1.32×10^{-6}*
(Stdev)	*(1.14×10^{-7})*	*(3.23×10^{-8})*	*(1.79×10^{-7})*	*(2.32×10^{-7})*

In order to account for mass differences in the photocatalytic experiments a comparison of the reaction rates and space time yields was performed. Mass normalized reactivity shows that both composite materials were more effective than the corresponding unsupported TiO_2 nanoparticles. Based upon the space time yield (per gram basis) the SiO_2-TiO_2 (5 nm) composite is approximately 6.9 times more effective than the corresponding neat TiO_2 particles. Similarly, the SiO_2-TiO_2 (NS) composite was 3.2 times more effective than the corresponding neat TiO_2 nanosheets. Utilization of the SiO_2 Stöber spheres as a support for the TiO_2 nanoparticles allows for maximization of the reactive sites while potentially preventing agglomeration, which is known to hinder photocatalytic reactivity [57]. Comparison of the two composite materials via mass normalized reaction rates show that the SiO_2-TiO_2 (5nm) photocatalyst is more that 3X higher than that of the SiO_2-TiO_2 (NS) however, the theoretical surface area of TiO_2 nanosheets is more than 3X lower in comparison to the 5 nm TiO_2. Unfortunately, the determination of the surface area of the TiO_2 in the composite photocatalyst is not trivial thus limiting the comparison to mass normalized reactivity.

Table 5 — Degradation efficiencies and quantum yields of the investigated SiO_2-TiO_2 composites and neat TiO_2 material photocatalysts for 2-CEES degradation under visible excitation ($\lambda > 400$ nm) after 24 h irradiation

Material	E_g (eV)	TiO_2 mass (mg)	Theoretical surface area (m^2/g)	Degradation efficiency (%)	Reaction rate (μmol/g/h)	QY (molecules/ photon)	Space time yield (molecules/ photon/g)
SiO_2-TiO_2 (5nm)	3.58	0.4	-	57.8	56.2	1.64×10^{-5}	4.10×10^{-2}
SiO_2-TiO_2 (NS)	3.39	1	-	30.5	16.5	1.2×10^{-5}	1.20×10^{-2}
TiO_2 (5nm)	3.31	3	283.8	44.1	8.1	1.77×10^{-5}	5.93×10^{-3}
TiO_2 (NS)	3.27	3.2	83.6	30.0	5.1	1.20×10^{-5}	3.75×10^{-3}
P25 TiO_2	3.16	7	56.7	14.9	1.8	9.26×10^{-6}	1.32×10^{-3}

The observed oxidation of 2-CEES into sulfoxide likely involves a two-step mechanism. The generation of electrons and holes from the TiO_2 surface traps under visible light excitation would be the first step. The generated holes could react with the lone pair of electrons on the sulfur of 2-CEES producing sulfur radical cation which has been proven during photocatalytic oxidation of sulfides in a prior work [58-60]. In conjunction, the photo-excited electrons may react with molecular oxygen producing superoxide radical anion $O_2^{\cdot-}$ [61]. Subsequent reaction between sulfur radical cation and superoxide radical anion would result in the formation of sulfoxide following the steps outlined in the literature [61] This reaction mechanism is further informed by Oae et al. [62] who showed neither sulfide nor sulfoxide reacted with superoxide alone when generated from potassium superoxide precursor without the formation of the sulfur radical cation. Martyaonov [54] further states that interaction of the superoxide anion with thioether cation should yield sulfoxide and sulfone oxidation products.

Assessment of the visible light absorption for the composite materials was performed using UV-Vis spectroscopy (Fig. 40). The normalized UV−visible spectra show an absorption band for 5 nm TiO_2 nanoparticles and nanosheets immobilized on SiO_2 spheres within the visible region ($\lambda > 400$ nm) which is not present in the spectrum of commercial 25 nm TiO_2 nanoparticles (Fig. 40a). Further insight into the intriguing behavior of TiO_2 nanoparticles and nanosheets was obtained through analysis of extinction spectra of aqueous suspensions measured in transmission mode, both before and after immobilization on SiO_2 (Fig. 40b). As expected, the 5 nm TiO_2 nanoparticles dispersed in water, do not absorb visible light. Additionally, the extinction of the SiO_2-TiO_2 (5 nm) composite is greater than that of the SiO_2 particles alone. The greatest extinction was measured for TiO_2 nanosheets in the aqueous solution. However, the SiO_2-TiO_2 (NS) composite extinction spectrum was similar to that of the SiO_2 particles alone (Fig. 40b). The observations from the extinction spectra suggest that scattering makes a large contribution to the extinction of non-transparent solutions.

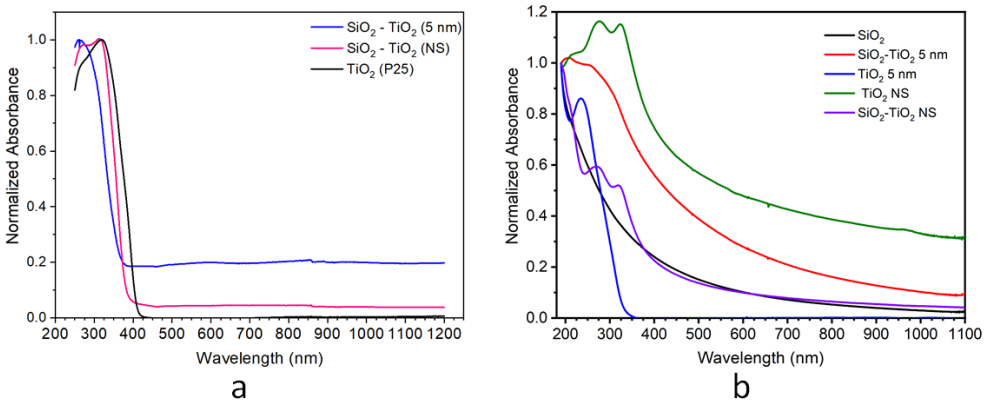

Fig. 40 — (a) UV-Vis spectra of solid samples of the individual materials and the SiO_2-TiO_2 composites (b) normalized UV-Vis spectra of aqueous suspensions of 5 nm TiO_2, TiO_2 NS, SiO_2 NPs, SiO_2-TiO_2 (5 nm) and SiO_2-TiO_2 (NS) composites.

The optical behavior was further assessed through computational modeling using Mie theory of the extinction spectra of 5 nm TiO_2, 421 nm SiO_2 nanoparticles and TiO_2 nanosheets in water. Modeling of the individual SiO_2 and TiO_2 particles (Fig. 41a) provided the following observations. First, a significant contribution to extinction in the visible is due to strong scattering from the 421-nm-SiO_2 particles. Second, the TiO_2 nanoparticles were modeled used the bulk dielectric function [63, 64] and, therefore, the computed absorption of the TiO_2 nanoparticles is practically equal to zero in the visible region (Fig. 41a). This is expected for TiO_2 particles with small number of surface and bulk defects. Interestingly, the experiments with the SiO_2-TiO_2 (5 nm) composite performed in air showed significant absorption in the visible. This can be attributed to the formation of surface defects in TiO_2 particles after they are exposed to air and treated in air at elevated temperatures. The defect-induced absorption in the TiO_2 component in the visible is thought to play an important role in the surface photochemistry reported above.

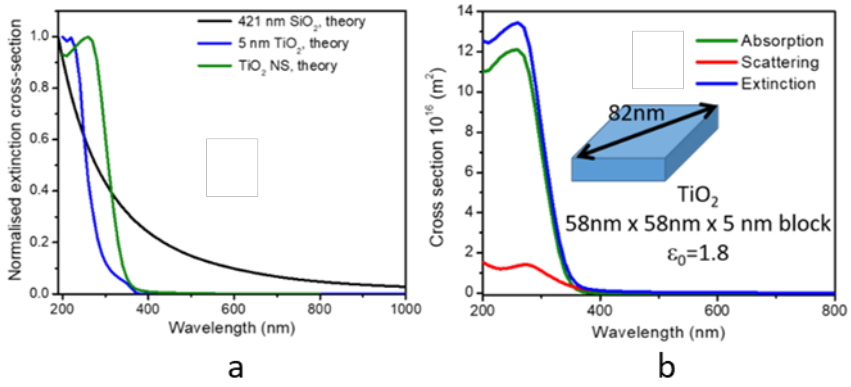

Fig. 41 — (a) computed extinctions of 5 nm TiO_2, TiO_2 NS and SiO_2 NPs; (b) computed extinction for TiO_2 NS with component scattering and absorption curves. The bulk dielectric constants were taken from Refs. [63, 64].

Overall, the TiO_2 nanoparticles and nanosheets rely on surface defects and trapped states to promote visible light driven oxidation. Additionally, the SiO_2 particle can help as absorbing media for 2-CEES favoring their chemical transformation. No significant visible light driven oxidation was observed for corresponding 25 nm TiO_2 particles under identical conditions indicating the importance of composite

photocatalyst design and suggests particle size effect (due to observed reactivity from the neat 5 nm TiO_2 nanoparticles and nanosheets).

Visible Light Induced Reactivity of Plasmonic Gold Nanoparticles Incorporated into TiO_2 matrix towards 2-Chloroethyl Ethyl Sulfide

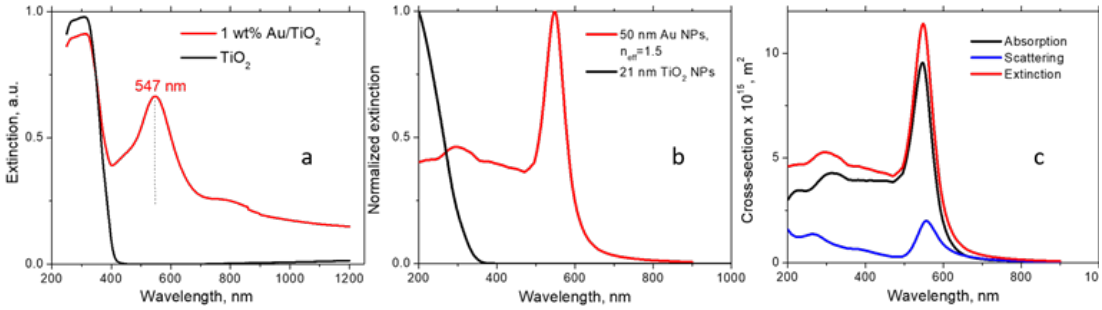

Fig. 42. (**a**) UV–Vis spectra of 1 wt% Au/TiO_2 and TiO_2 powders in the KBr matrix; (**b**) extinctions of the components of the powder calculated by COMSOL. The Au NP extinction is presented for the effective media; (**c**) the structure of the extinction cross section of the 50 nm Au NP, including scattering and absorption.

Figure 42a shows UV–Vis spectra of Au/TiO_2 and TiO_2 powders. The spectrum of Au/TiO_2 exhibits a sharp maximum in the visible region at 547 nm due to LSPR. At $\lambda < 400$ nm, the TiO_2 absorption band is observed. In Figure 42b, the optical calculations of the TiO_2 and Au NPs incorporated into the TiO_2+KBr matrix are presented. The TiO_2 extinction is mostly due to absorption since the scattering from a small semiconductor NP is typically weak. Simultaneously, the extinction of the Au NPs includes both scattering and absorption components, as shown in Figure 42c. Although absorption dominates for 50 nm Au NPs, the contribution of scattering is not negligible. The calculated position of the LSPR peak in Figure 1b depends on the NP size and matrix dielectric constant.

The morphology of the Au/TiO_2 photocatalyst was examined by TEM, as shown in Figure 43. The photocatalyst consists of spherical monodisperse 50 nm Au nanoparticles and 10–25 nm crystalline TiO_2 NPs of mostly spherical shapes that enclose Au NPs. Au NPs are evenly distributed in the TiO_2 matrix. A close inspection of the Au-TiO_2 interface reveals close contact between the plasmonic NP and semiconducting support, which is important for successful injection of photogenerated hot electrons from the plasmonic NPs into a semiconducting support, as well as for the rapid heat transfer from the photoexcited Au NPs. To confirm that the Au NP surface is not oxidized, the Au surface speciation was examined by XPS. XPS analysis revealed the presence of Au 4f photoelectron lines, centered at 83.7 and 87.3 eV. These lines can be fitted by a doublet ($4f_{7/2}$ and $4f_{5/2}$, respectively, FWHM = 1.36), corresponding to metallic Au [65].

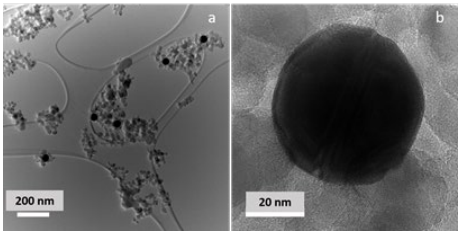

Fig. 43. (a) Low- and (b) high-resolution images of 1 wt% Au/TiO_2 photocatalyst

Prior to the assessment of the photocatalytic activity of the Au/TiO_2 photocatalyst towards 2-CEES decomposition under visible excitation, the activity of the photocatalyst was evaluated in the dark. For this, 2-CEES vapor was introduced in the DiffusIR environmental cell filled with He for 2 h, and the series of consecutive DRIFTS spectra were recorded (125 spectra total, 58.85 sec/spectrum). Figures 44–46 (top panels) compare spectral development during CEES dosing for Au/TiO_2 and TiO_2 photocatalysts in the

Table 6. IR band and mode assignment for 2-CEES adsorbed on Au/TiO_2 and TiO_2 photocatalysts

Vibration Mode	IR Frequency, cm^{-1}, Au/TiO_2	IR Frequency, cm^{-1}, TiO_2	Literature
$\nu(CH_2)_{as}$	2980	2971, 2976	2965, 2971, 2956
$\nu(CH_3)_{as}$	2936	2935	2933, 2917
$\nu(CH_2)_{as}$, overtones	2879	2879	2877, 2911, 2897, 2855
$\delta(CH_2)_{as}$ bent	1457, 1468	1456	1456, 1484
(CH_2) scissor	1418	1426, 1411	1433, 1460
$\delta(CH_3)_s$ bent	1376, 1388	-	1381, 1407
(CH_2)wag	1241, 1272	1267	1267, 1299, 1266, 1294
$S(CH_2)$wag	1217	-	1219, 1218

three different regions. Difference spectra were presented to facilitate comparison with the background measured on a clean surface prior to the 2-CEES introduction. In the first region, we focus on the surface specific stretching vibrations of OH groups in isolated Ti-OH (~3700 cm^{-1}) moieties, as well as binding (1620–1660 cm^{-1}) and stretching OH vibrations (3592 cm^{-1}) in Ti-H_2O species, while in the second and the third regions fingerprint and aliphatic vibrational modes of the 2-CEES molecules are presented. Loss of OH vibration during 2-CEES dosing in the first region displayed in Figure 44a, b is attributed to 2-CEES adsorption on the Au/TiO_2 and TiO_2 surfaces. The OH absorbance decreases with time as more 2-CEES molecules diffuse through the photocatalyst pores and adsorb on the surface. Previous reports indicate that 2-CEES adsorbs on Ti-OH by forming hydrogen bonding via both the chlorine and sulfur moieties [66]. The region at $\lambda < 1750$ cm^{-1} in Figure 3a,b looks somewhat different for Au/TiO_2 versus TiO_2. While two clearly distinguishable bands at 1624 and 1655 cm^{-1} are observed for TiO_2, three broad bands (at 1581, 1634, and 1657 cm^{-1}) are displayed for Au/TiO_2. This may be due to bond energies at the Au/TiO_2 surface being affected by the presence of Au at the interface with TiO_2.

The absorption of 2-CEES on the surface is confirmed by the increases in intensities of CH_2, CH_3, $S(CH_2)$, and C-C band as 2-CEES dosing progresses, as shown in Figures 45 and 46a,b. Band assignments in the aliphatic and fingerprint regions are provided in Table 6.

The bands at 1311, 1180, and 1144 cm^{-1} in Figure 45a, which are not included in Table 6, may be assigned to the formation of C-O bonds due to 2-CEES hydrolysis, as C-O moieties exhibit stretching frequencies in the region between 1100 and 1200 cm^{-1} [67]. Formation of 2-ethylthio ethanol by replacement of Cl species in 2-CEES molecules by OH groups in the dark on P25 TiO_2 in the air has been demonstrated by GC–MS in our previous work [7]. We attribute the peak at 1311 cm^{-1} to C-O bond formation as well because of the similar pattern of spectral development. The dynamics of the development of the bands at the three frequencies suggests the time lag between 2-CEES adsorption and hydrolysis. Note that the blue region is located at the bottom of the three bands assigned to C-O moieties, contrary to other peaks. The fastest saturation is observed for the bands centered at 1272, 1241 ((CH_2)wag), and 1217 cm^{-1} ($S(CH_2)$wag). Interestingly, the peaks at 1241 cm^{-1} and 1217 cm^{-1} decrease in magnitude after fast saturation. This may be related to the formation of hydrogen bonds between sulfur atoms and the surface OH groups. In addition, 2-CEES is expected to physisorb on the surface of Au NPs via the sulfur atom [68]. In spite of Au strong affinity for sulfur, alkylsulfides (such as diethylsulfide), and Cl-substituted alkylsulfides (such as 2-CEES) adsorb reversibly on Au. A comparison of the spectral features of the Au/TiO_2 and TiO_2 surfaces shows similarity in the aliphatic region and distinction in the fingerprint region (Figures 45a,b and 46a,b, respectively). The most significant difference in the fingerprint region is the absence of vibrational modes below 1267 cm^{-1} and the decrease in the magnitude of the vibrational mode at 1334 cm^{-1} as 2-CEES dosing progresses. The absence of bands below 1267 cm^{-1} implies that the TiO_2 surface is less reactive, in comparison to Au/TiO_2, while the band at 1334 cm^{-1} may be related to the desorption of impurities from the TiO_2 surface as 2-CEES adsorbs on the surface.

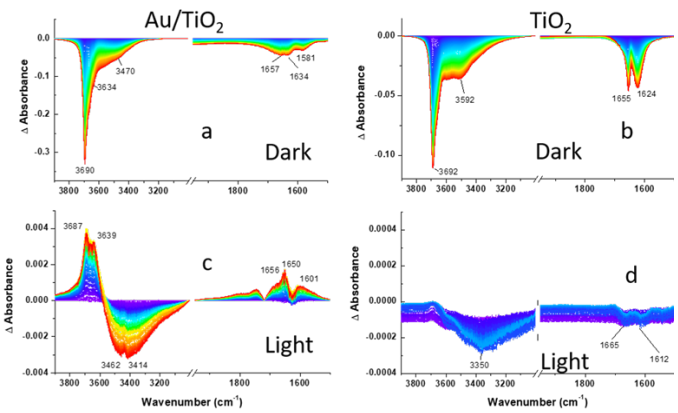

Fig. 44. DRIFTS difference spectra of (**a**,**c**) Au/TiO_2 and (**b**,**d**) TiO_2 photocatalysts recorded during 2-CEES dosing in anaerobic conditions: (**a**,**b**)-dark; (**c**,**d**)-under visible light excitation following He purge. OH region is shown. Spectra in the dark are calculated by subtraction of the background spectrum recorded on a clean surface. The last spectrum measured in the dark under He purge was used as a background for the spectra measured under visible light excitation.

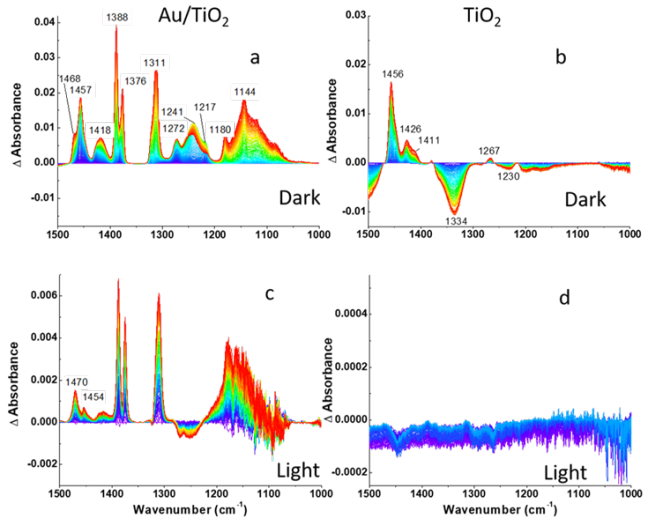

Fig. 45. DRIFTS difference spectra of (a,c) Au/TiO_2 and (b,d) TiO_2 photocatalysts recorded during 2-CEES dosing in anaerobic conditions: (a,b)-dark, (c,d)-under visible light excitation following He purge. Fingerprint region is shown.

Visible light exposure leads to partial 2-CEES desorption, evident by the increase in the intensity of the bands assigned to the isolated Ti-OH (3687 and 3639 cm^{-1}) and binding OH vibrational modes of water (1656, 1650, and 1601 cm^{-1}) in Figure 44c. Surprisingly, this is accompanied by the partial loss of the H_2O stretching vibrations (3462 and 3414 cm^{-1}). It should be noted that the effect is small, as peak intensities in Figure 3c are an order of magnitude lower in comparison to Figure 44a.

Moreover, the 2-CEES partial desorption from the surface is consistent with a decrease in the magnitude of (CH_2)wag (1272 and 1241 cm^{-1}) and $S(CH_2)$wag (1217 cm^{-1}) vibrational modes in Figure 45c. The remaining vibrations grow in magnitude likely due to continuous 2-CEES diffusion into the catalyst pores.

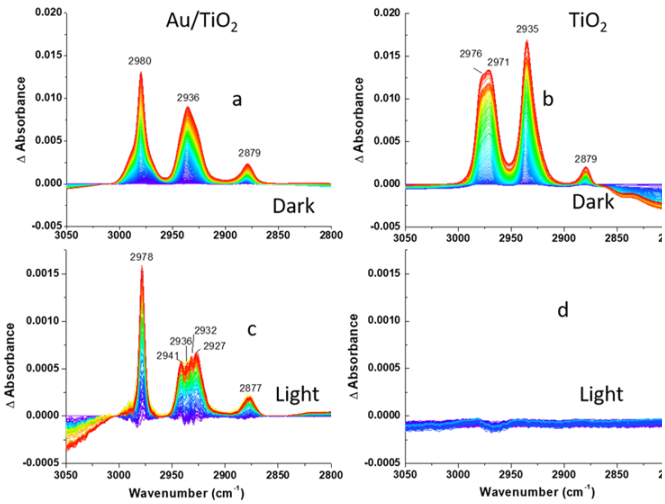

Fig. 46. DRIFTS difference spectra of (a,c) Au/TiO_2 and (b,d) TiO_2 photocatalysts recorded during 2-CEES dosing in anaerobic conditions: (a,b)-dark, (c,d)-under visible light excitation following He purge. Aliphatic region is shown.

Figure 46c shows the same trend of growth in magnitude for the three bands displayed in Figure 46a. However, a much narrower $\nu(CH_2)_{as}$ band (2978 cm^{-1}) is observed as a result of visible light excitation. Furthermore, instead of a broad $\nu(CH_s)_{as}$ band at 2936 cm^{-1}, four bands (2941, 2936, 2932, 2927 cm^{-1}) appear, as can be seen in Figure 5c. Comparison of visible light effect at the two interfaces (see Figures 44d and 46d) shows more significant changes at the Au/TiO_2 interface. The only noticeable effect at the TiO_2 surface is related to a loss of OH stretching vibrational modes at 3350 cm^{-1}, as can be seen in Figure 44d. Therefore, plasmonic Au NPs promote 2-CEES partial desorption from the surface. As we mentioned earlier, Au NPs excited with visible light can create photochemistry in two ways. Absorption in an NP leads to the generation of heat and creates phototemperature, and we believe that this photothermal mechanism is the likely reason for the desorption of 2-CEES in our experiments. Another mechanism involves the generation of hot electrons, which can be injected into the TiO_2 particles. Since our Au NPs are relatively large (50 nm), the photothermal mechanism is expected to dominate. The estimated internal efficiency for the over-barrier hot-electron generation in our Au NPs is ~4% [69], whereas the photothermal conversion efficiency for our NPs at the plasmon peak (the ratio between the absorption and extinction in Figure 42c) is high at ~77%. Therefore, the photothermal heating effect likely prevails. Although both mechanisms are expected to lead to an increase in the photochemical reaction rate on the TiO_2 surface, it is important to observe some photocatalytic activity of neat TiO_2 as a control prior to incorporating Au NPs. However, for just TiO_2 we do not observe noticeable photochemistry. Therefore, we surmise that the heat generated by photo-excited Au NPs promotes 2-CEES desorption instead of promoting reaction rate. Overall, the observed photothermal effect is small, likely due to a low loading of Au nanoparticles. The question arises whether the photocurrent enhancement for CH_3OH oxidation by 50 nm Au NPs observed in Ref. [4] was due to the photothermal effect or injection of hot electrons into the TiO_2 support. Although the heat contribution cannot be ignored, we presume that the over-barrier hot-electron injection in the setting of Ref. [4] played a main role in promoting reaction rate because of a faster heat transfer rate at the photocatalyst/solution vs. photocatalyst/gas interface.

No effect of visible light was observed under aerobic conditions, likely due to a higher rate of 2-CEES hydrolysis in the dark in the presence of oxygen.

Surface and Structural Dependent Reactivity of TiO_2 Nanostructures under Relevant Conditions

Titanium oxide materials provide a robust platform for the development of reactive materials for a variety of applications. The structure, morphology, and the surface chemistry play important roles in the overall reactivity of materials such as TiO_2. Analysis of titanium oxide materials synthesized using different reaction routes showed significant heterogeneous reactivity for both photochemical oxidation ($\lambda > 400$ nm) and direct hydrolysis of 2-chloroethyl ethyl sulfide (2-CEES). Titanium oxides (TiO_2-PA1 and TiO_2-PA2) synthesized via acidic hydrothermal reactions of $TiCl_4$ in the presence of phosphonic acids (PAs) displayed enhanced photochemical oxidation in comparison to an analogous TiO_2 material synthesized without PA (TiO_2-0) and commercial P25 TiO_2. Alternatively, nanowire $H_2Ti_2O_5 \cdot H_2O$ synthesized by alkaline hydrothermal reaction was capable of efficient hydrolysis of the carbon-chlorine (C-Cl) bond of 2-CEES regardless of visible light excitation.

The preliminary 24-hour 2-CEES challenges for the four synthesized materials under either visible light excitation (red curves) or when the samples are kept in the dark (black curves) are shown in Fig. 47. TiO_2-0 appears to show minimal reactivity under both conditions with no detectable oxidation or hydrolysis products in the chromatographs. TiO_2-PA1 and TiO_2-PA2 displayed visible light driven oxidation of 2-CEES via direct oxidation of the thioether sulfur and the generation of both 2-CEES sulfoxide and sulfone with no detectible 2-CEES remaining after 24 hours. In contrast, when TiO_2-PA1 and TiO_2-PA2 were left in the dark, no oxidation of the thioether sulfur was observed and only 2-CEES was detected in the GC-MS. Additionally, complete removal of 2-CEES via hydrolysis of the C-Cl bond to generate 2-ethylthio ethanol independent of visible light excitation was observed for the $H_2Ti_2O_5 \cdot H_2O$ synthesized nanowires.

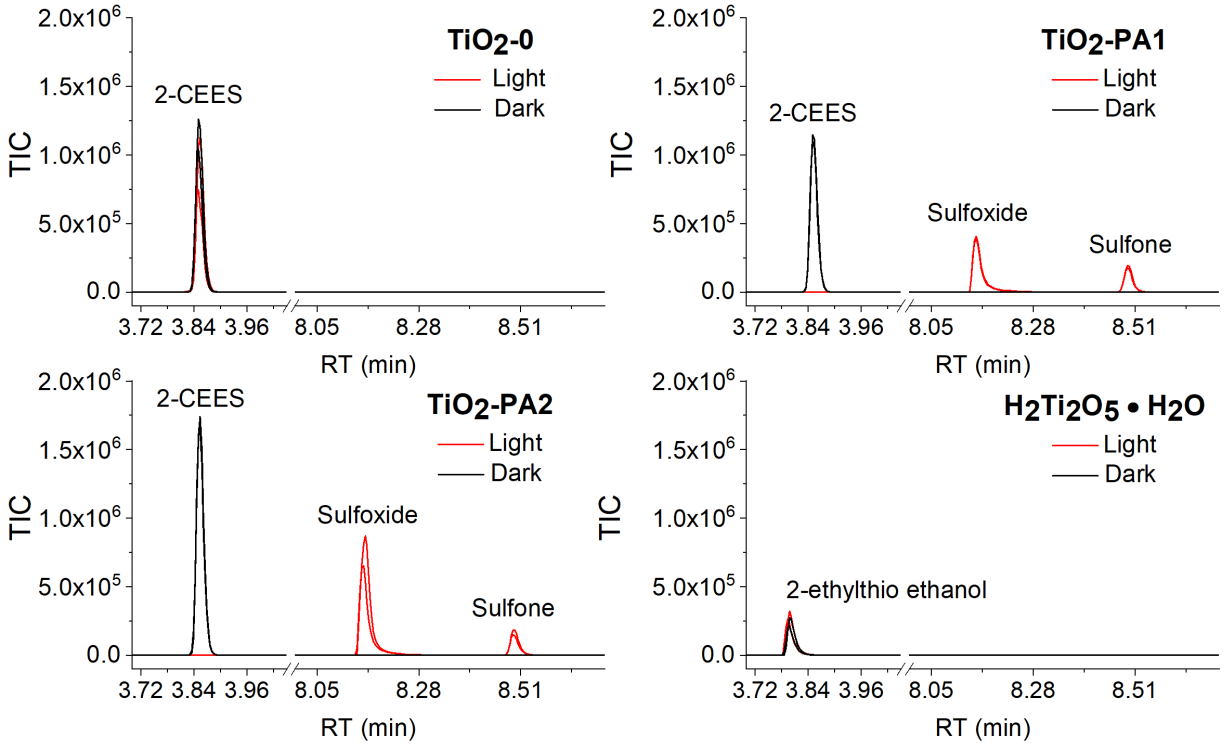

Fig. 47— GC-MS chromatographs of 2-CEES 24 hour challenge assessments. 7 mg of each TiO_2 and $H_2Ti_2O_5 \cdot H_2O$ samples were assessed under both light and dark conditions. Challenges were performed with 25 µL of 2-CEES stock solution (19.25 µL, 1.65×10^{-4} mol) in 2 mL of CH_2Cl_2.

The complete transformation of 2-CEES (2.07 x 10^{-6} mol) in 24 hours resulted in further analysis of TiO_2-PA1, TiO_2-PA2 and $H_2Ti_2O_5 \cdot H_2O$ to determine the rates based upon shorter exposure durations. Challenges to determine the reaction rates were conducted following the same deposition and extraction procedure but reactions were terminated and extracted at one, four and eight hour time intervals to assess the degradation of 2-CEES and byproduct formation. Fig. 48 displays the time trial chromatographic analysis for the decomposition of 2-CEES for TiO_2-PA1, TiO_2-PA2 and $H_2Ti_2O_5 \cdot H_2O$. Within four hours of deposition, 2-CEES was no longer detected within the chromatographs and only the oxidation and hydrolysis products were observed. Photochemical oxidation reaction rates of 99 and 168 µmol/g/h (quantum yields of 5.07 x 10^{-4} and 8.58 x 10^{-4} molecules/photon) were calculated for TiO_2-PA1 and TiO_2-PA2, respectively. While the hydrolysis reaction rate for the nanowire $H_2Ti_2O_5 \cdot H_2O$ was calculated to be 279.2 µmol/g/h.

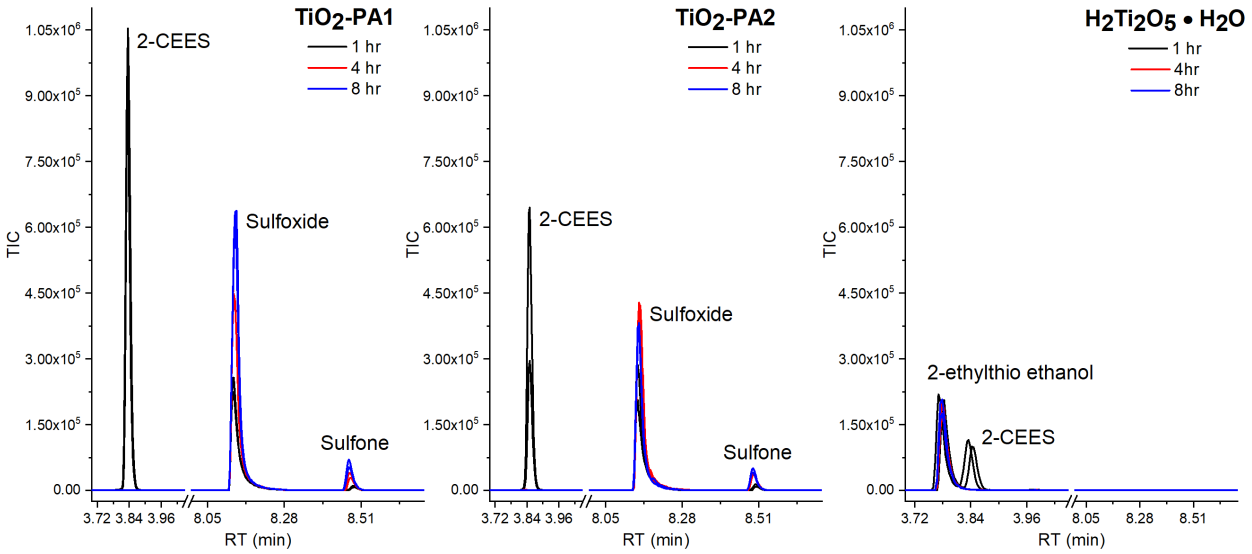

Fig. 48 — GC-MS analysis of time trails for 2-CEES oxidation and hydrolysis. 7 mg of each of the TiO_2 and $H_2Ti_2O_5 \cdot H_2O$ samples were assessed under visible light excitation at 1, 4 and 8 hours. Challenges were performed with 25 µL of 2-CEES stock solution (19.25 µL, 1.65x10^{-4} mol) in 2 mL of CH_2Cl_2.

The significant reactivity observed for these materials resulted in assessments of the surface chemistry and nanostructure to understand the reactivity. The acidic hydrothermal reactions of $TiCl_4$ with and without phosphonic acids produced TiO_2 nanomaterials (TiO_2-0, TiO_2-PA1, TiO_2-PA2) shown in Fig. 49a-c. The incorporation of the two alkylphosophonic acids ($C_{14}H_{29}PO_3H_2$ and $C_9H_{19}PO_3H_2$) produced TiO_2-PA1 and TiO_2-PA2 materials shown in Fig. 49b and c, respectively. The addition of the phosphonic acids resulted in modified TiO_2 nanoscale morphologies in comparison to the TiO_2-0 material shown in Fig. 49a, which did not include a phosphonic acid. Alternatively, the alkaline hydrothermal treatment of P25 TiO_2 produced long nanowires of $H_2Ti_2O_5 \cdot H_2O$ (Fig. 49d) with high a BET surface area of 207.4 m^2/g.

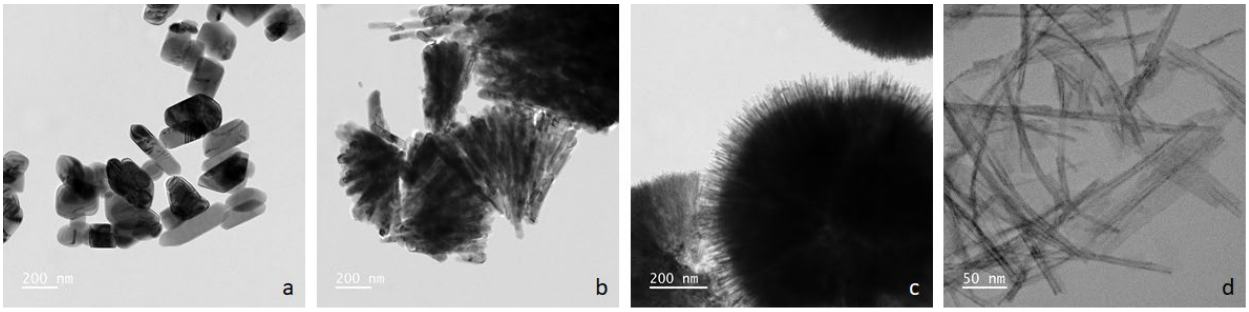

Fig. 49 — Bright field TEM images of synthesized titanium oxide nanomaterials a (TiO_2-0), b (TiO_2-PA1), c (TiO_2-PA2) and d ($H_2Ti_2O_5 \cdot H_2O$).

Characterization of the TiO_2 nanomaterials reveal that TiO_2-0 was comprised of Rutile phase short nanorod morphologies with nanorod diameters on the order of 100-120 nm. Alkylphosphonic acids incorporation into the hydrothermal synthesis resulted in the formation of Rutile phase nanorod bundles (TiO_2-PA1) with nanorod diameters on the order of 30 nm and mixed Rutile and Anatase phase nanoflowers (TiO_2-PA2) comprised mostly of particles that appear roughly spherical and are made up of fine 8-10 nm diameter nanorods radiating out from a central point. In addition, TiO_2-PA2 contained two other distinct morphologies: agglomerated nanorods and agglomerated semi-spherical nanoparticles not shown in Fig. 49. The morphology modification to the TiO_2 particles resulted in a significant increase to the BET surface area for TiO_2-PA1 and TiO_2-PA2 (20 and 71.4 m^2/g, respectively) in comparison to TiO_2-0 (2.6m^2/g).

Modification of metal oxides with alkylphosphonic acids usually leads to formation of self-assembled monolayers on the surface [70-78]. Analysis of the surface composition of the TiO_2 materials was performed with XPS shown in Fig. 50. The XPS results show the typical Ti2p photoelectron lines centered at 458.9 and 464.7 eV which can be assigned to a Ti2p doublet (2p3/2 and 2p1/2, respectively), corresponding to Ti^{4+} in TiO_2 [65]. The O1s core level spectra are dominated by a peak centered at 530.3 eV, specific for Ti-O binding energy in TiO_2 with additional peaks at 532.2 eV and 533.3 eV in Fig. 50 for TiO_2-PA1 and TiO_2-PA2 were assigned to P=O and P-OH bonds. The larger peak centered at 531.4 eV in the spectra for TiO_2-PA1 and TiO_2-PA2 is due to Ti-O-P bond formation [79]. Additionally, the positions of the P2p doublet (2p3/2 and 2p1/2) photoelectron lines for TiO_2-PA1 and TiO_2-PA2 are shifted by 0.8 eV to lower binding energies which implies that phosphorus is less oxidized which is consistent with Ti-O-P bond formation in comparison to neat phosphonic acids.

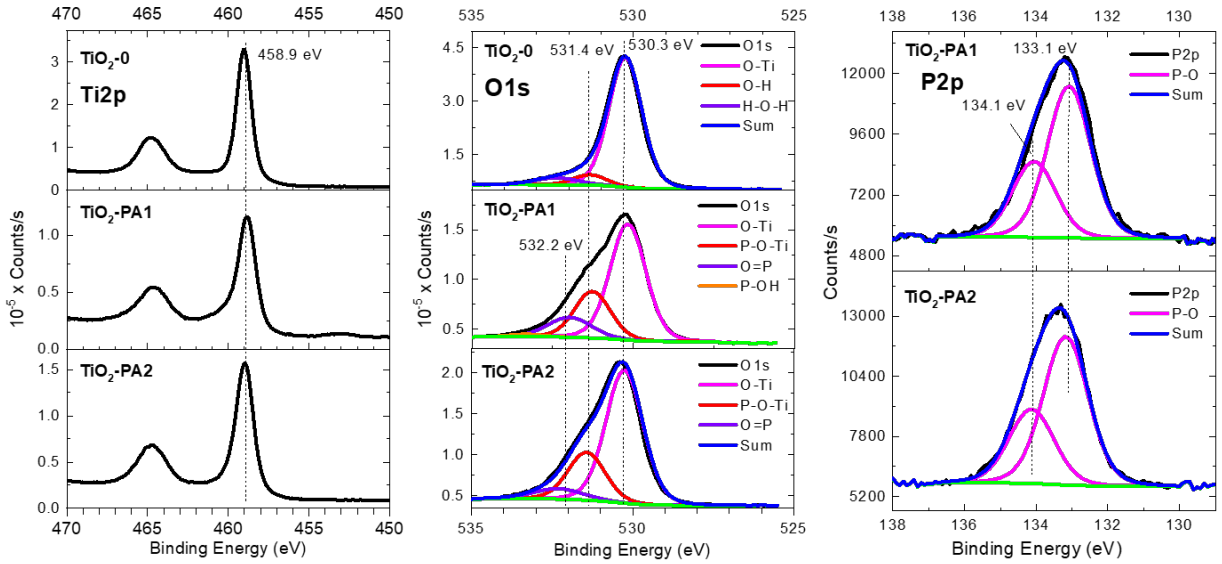

Fig. 50 — High resolution Ti2p, and O1s core level spectra collected from materials TiO_2-0, TiO_2-PA1 and TiO_2-PA2 and P2p core level spectra of TiO_2-PA1 and TiO_2-PA2, modified by $C_{14}H_{29}CO_3H_2$ and $C_9H_{19}CO_3H_2$ phosphonic acids, respectively.

An array of factors are considered in the assessment of the phosphonic acid modified TiO_2 materials. The photochemical oxidation reactivity driven by visible light excitation may arise from the formation of the surface bound phosphonic acid species and the resulting TiO_2 particle structures. Surface bound phosphonic acids to TiO_2 have been shown to induce a surface dipole due to greater electron withdrawing capabilities of the phosphonate group, which can potentially influence charge separation of photoexcited electrons and holes [76]. Charge transfer from surface bound ligands to semiconducting TiO_2 has been shown through various surface bound species that would directly influence the photochemical reactivity [80, 81]. Additionally, surface hydroxyl group functionalities, which are known to bind 2-CEES to TiO_2 through the S and Cl interactions, are blocked therefore reactivity would be directed toward photochemical oxidation [35, 66, 71, 78, 82]. Structurally, the incorporation of alkylphosphonic acids promotes the formation of nanorod and nanowire assemblies with increased surface area and consequently a greater number of active sites. Other factors include increased light absorption efficiency from the nanostructure assemblies in comparison to individual nanoparticles due to multiple reflections and scattering of the light [83] and improved separation and utilization of photogenerated carriers in nanorods of smaller diameter [84]. Comparison of the photocatalytic activity between TiO_2-PA2 relative to TiO_2-PA1 can be attributed to increase in the surface area (71.4 vs 20 m2/g, Table 1), shorter distances to the surface, as well as enhanced charge separation at Anatase/Rutile junctions [85].

In contrast, the synthesized nanowire $H_2Ti_2O_5 \cdot H_2O$ promotes the hydrolysis of 2-CEES. The proposed structure of $H_2Ti_2O_5 \cdot H_2O$ by Tsai and Teng [86] with anionic nature of the TiO_6 octahedra and the presence of OH^- in addition to the H^+ ions within the material has the potential to promote hydrolysis of the C-Cl bond. The proposed hydrolysis mechanism of 2-CEES is believed to proceed through the formation of a cyclic sulfonium cation followed by nucleophilic attack resulting in formation of 2-ethylthio ethanol [87]. Therefore, the structure along with the enhanced surface area of 207.4 m^2/g from the $H_2Ti_2O_5 \cdot H_2O$ nanowire morphology allows for enhanced heterogeneous hydrolysis of the C-Cl bond of 2-CEES.

CONCLUSIONS

Refractory transition metal nitrides represent a new group of plasmonic materials that offer advantages of low cost, chemical inertness, high mechanical durability and thermal stability. RTMN nanoparticles can be synthesized by ammonolysis of $MCl_3(THF)_3$ (M=Ti, V, Cr) and $Zr(NMe_2)_4$ precursors [1]. A novel method has been developed for growing well-dispersed TiN nanoparticles inside a non-reactive porous Al_2O_3 (TiN/Al_2O_3). In-house made TiN, VN and CrN nanoparticles exhibited weak LSPR in comparison to commercial TiN (Plasma Chem) most likely due to NPs' oxidation and agglomeration. On the contrary, in-house made ZrN nanoparticles outperformed commercial material produced by American Elements. A method has been proposed for synthesis of TiN-Au core-shell nanoparticles with an ultra-thin (monolayer or less) Au shell.

Compared to Au nanoparticles, the best performing TiN NPs show red-shifted and broadened plasmon peaks that semi-quantitatively agree with the results of electromagnetic simulations [2]. A weaker and broader plasmonic response of TiN NPs vs Au is reflected in the predicted lower hot carrier generation rates. ZrN NPs are expected to establish a much sharper, blue-shifted LSPR in comparison to TiN, reminiscent to that of Au NPs, and respectively, higher hot carrier generation rates. However, these theoretical predicitons can be hardly observed in practice due to the nearly unavoidable oxidation and agglomeration of ZrN NPs, synthesized at elevated temperatures. Optical absorption maxima of the in-house made ZrN materials appeared broader and red-shifted as compared to theoretical predictions, which remained true even after the oxide layer was taken into account in electromagnetic simulations [4].

Contrary to Au/TiO_2, potential bias is required for initiation of photo-induced CH_3OH oxidation at the TiN/TiO_2 interface that forms an ohmic junction [2, 3]. However, even in the presence of applied bias, no (or weak) plasmonic effect is observed. The photocatalytic process is believed to be driven by holes generated by interband transition of TiN NPs at $\lambda < 630$ nm. Although the ZrN/TiO_2 photocatalyst also promote TiO_2 activity towards CH_3OH photoelectrochemical oxidation under visible excitation, the mechanism of enhancement appears to be different for the two nitrides. The photocurrent enhancement observed for ZrN NP is assigned to a photothermal effect, since charge transport from the NP should be drastically inhibited due to the dielectric ZrO_2 shell.

The performance of both TiN/TiO_2 and ZrN/TiO_2 photocatalysts is hampered by the strong oxygen affinity of Ti and Zr. A protective metallic shell that inhibits oxidation could potentially address this issue. Another way to utilize the promising plasmonic properties of TiN and ZrN NPs would be to apply them to reductive processes, coupled to a *p*-type semiconductor. An example of a *p*-type semiconductor that can be coupled with TiN NPs is GaN. The advantage of using *p*-type GaN is that no potential bias would be required to drive photoelectrochemical reaction at the TiN/*p*-GaN interface that forms a Schottky barrier. The latter fact was demonstrated in this program.

Unlike TiN, Au forms a Schottky barrier with TiO_2, and Au/TiO_2 photocatalyst can promote photocatalytic reactions at the photocatalyst/air interface. This material was used to determine the mechanism of the effect of visible light on photooxidation of the Navy-relevant organic molecule 2-CEES. We (in collaboration with co-authors from US Army DEVCOM CBC) demonstrated that under anaerobic conditions, 2-CEES partially desorbs from the Au/TiO_2 surface likely due to a photothermal effect, induced by photo-excited plasmonic Au nanoparticles [5].

To optimize photocatalytic activity of the semiconducting TiO_2 support, materials with different morphology have been synthesized and investigated [6, 7]. We found that the semiconductor's morphology does play an important role in visible-light driven potocatalysts's reactivity. 5 nm TiO_2 NPs and TiO_2 nanosheets supported on monodisperse SiO_2 Stöber spheres were capable of photooxidation of 2-CEES to 2-chloroethyl ethyl sulfoxide under visible excitation. The higher photocatalytic activity of TiO_2 nanoparticles and nanosheets in comparison to commercial P25 TiO_2 was assigned to surface defects and

trapped states that promoted visible light absorption. Modeling results confirmed that the experimental absorption of TiO_2 nanoparticles and nanosheets in the visible was due to the surface defects.

Even higher photocatalytic 2-CEES oxidation rates were demonstrated by hierarchical TiO_2 structures, comprising (1) assemblies of nanorods, and (2) nanoflowers that appear roughly spherical and made up of fine 8-10 nm diameter nanowires radiating out from a central point [6]. These materials were synthesized in the presence of long-chain alkylphosphonic acids. Their high photocatalytic activity and selectivity towards 2-CEES photooxidation (mostly to sulfoxide) was assigned to (1) better light absorption by assemblies of nanowires and nanorods in comparison to individual nanorods, (2) improved separation of photogenerated carriers in thinner nanorods and nanowires and at Anatase/Rutile junctions, (3) high surface area, and (4) the exclusion of surface OH groups due to the formation surface functionalization with alkyl phosphonic acids via Ti-O-P bonds on the TiO_2. These materials can be used as a platform for modification by plasmonic nanoparticles in the future.

Some of the materials synthesized within this program, demonstrated activity towards hydrolysis of 2-CEES and Demeton-S (nerve agent VX simulant) in the dark. Nanowire-form $H_2Ti_2O_5 \cdot H_2O$ was found to be capable of highly efficient hydrolysis of the carbon-chlorine (C-Cl) bond of 2-CEES [6]. On the other hand, high surface area TiN NPs and TiN NPs incorporated into porous γ-Al_2O_3 pellets, promoted hydrolysis of Demeton-S via P-S bond cleavage [1].

REFERENCES

[1] A.P. Purdy, O.A. Baturina, B.S. Simpkins, S. Giles, T. Brintlinger, J. Wynne, SN Applied Sciences, 2 (2020) 888.

[2] O.A. Baturina, A. Epshteyn, B. Simpkins, N. Bhattarai, T.H. Brintlinger, Journal of the Electrochemical Sociaty, 166 (2019) H485

[3] B.S. Simpkins, A. Purdy, A. Epshteyn, O. Baturina, J. Phys. Chem. C, 123 (2019) 13863
.
[4] O.A. Baturina, A. Epshteyn, A.C. Leff, A.P. Purdy, T. Brintlinger, B.S. Simpkins, E.Y. Santiago, A.O. Govorov, Journal of the Electrochemical Society, 168 (2021) 016503

[5] W. Gordon, A. Balboa, S. Giles, A. Epshteyn, O. Avalos-Ovando, A. Govorov, M. McEntee, O. Baturina, Crystals, 11 (2021).

[6] S.L. Giles, A.M. Kastl, A.P. Purdy, A.C. Leff, O.A. Baturina, ACS Applied Materials & Interfaces, submitted in September 2021.

[7] S.L. Giles, A. Sousa-Castillo, E.Y. Santiago, A.P. Purdy, M.A. Correa-Duarte, A.O. Govorov, O.A. Baturina, Colloid Interface Sci. Commun., 41 (2021) 100362.

[8] A. Naldoni, U. Guler, Z.X. Wang, M. Marelli, F. Malara, X.G. Meng, L.V. Besteiro, A.O. Govorov, A.V. Kildishev, A. Boltasseva, V.M. Shalaev, Adv. Opt. Mater., 5 (2017).

[9] T. Liu, L.V. Besteiro, Z. Wang, A.O. Govorov, Faraday Discuss., 214 (2019) 199

[10] S. Exarhos, A. Alvarez-Barragan, E. Aytan, A.A. Balandin, L. Mangolini, ACS Energy Lett., 3 (2018) 2349.

[11] S. Naya, M. Teranishi, T. Isobe, H. Tada, Chem Commun, 46 (2010) 815.

[12] S. Higashimoto, Catalysts, 9 (2019).

[13] E. Kowalska, R. Abe, B. Ohtani, Chem Commun, (2009) 241.

[14] S. Naya, A. Inoue, H. Tada, J. Am. Chem. Soc., 132 (2010) 6292.

[15] D.W. Wang, S.C. Pillai, S.H. Ho, J.B. Zeng, Y. Li, D.D. Dionysiou, Appl. Catal. B-Environ., 237 (2018) 721.

[16] A. Gelle, T. Jin, L. de la Garza, G.D. Price, L.V. Besteiro, A. Moores, Chem. Rev., 120 (2020) 986.
[17] Y. Ide, M. Matsuoka, M. Ogawa, J. Am. Chem. Soc., 132 (2010) 16762.

[18] Z.K. Zheng, B.B. Huang, X.Y. Qin, X.Y. Zhang, Y. Dai, M.H. Whangbo, J. Mater. Chem., 21 (2011) 9079.

[19] A. Primo, A. Corma, H. Garcia, PCCP, 13 (2011) 886.

[20] S. Neatu, B. Cojocaru, V.I. Parvulescu, V. Somoghi, M. Alvaro, H. Garcia, J. Mater. Chem., 20 (2010) 4050.

[21] W. Herwig, H.H. Zeiss, J. Org. Chem., 23 (1958) 1404.

[22] L.E. Manzer, Inorg. Synth., 21 (1982) 135.

[23] N.A. Jones, S.T. Liddle, C. Wilson, P.L. Arnold, Organometallics, 26 (2007) 755.

[24] M.H. Chisholm, C.E. Hammond, J.C. Huffman, Polyhedron, 7 (1988) 2515.

[25] M. Repoux, Surface and Interface Analysis, 18 (1992) 567.

[26] Y.S. Femenias, U. Angst, F. Caruso, B. Elsener, Materials and Structures, 49 (2016) 2637.

[27] A.A. Barragan, N.V. Ilawe, L. Zhong, B.M. Wong, L. Mangolini, J. Phys. Chem. C, 121 (2017) 2316.

[28] S.L. Giles, J.G. Lundin, R.B. Balow, P.E. Pehrsson, J.H. Wynne, Applied Catalysis a-General, 542 (2017) 306.

[29] R.B. Balow, S.L. Giles, C.L. McGann, G.C. Daniels, J.G. Lundin, P.E. Pehrsson, J.H. Wynne, Industrial & Engineering Chemistry Research, 57 (2018) 8630.

[30] C.L. McGann, G.C. Daniels, S.L. Giles, R.B. Balow, J.L. Miranda-Zayas, J.G. Lundin, J.H. Wynne, Macromol. Rapid Commun., 39 (2018).

[31] Y.C. Yang, J.A. Baker, J.R. Ward, Chem. Rev., 92 (1992) 1729.

[32] G.W. Wagner, Y.C. Yang, Industrial & Engineering Chemistry Research, 41 (2002) 1925.

[33] S.S. Talmage, A.P. Watson, V. Hauschild, N.B. Munro, J. King, Current Organic Chemistry, 11 (2007) 285.

[34] G.W. Wagner, D.C. Sorrick, L.R. Procell, M.D. Brickhouse, I.F. Mcvey, L.I. Schwartz, Langmuir, 23 (2007) 1178.

[35] T.J. Bandosz, M. Laskoski, J. Mahle, G. Mogilevsky, G.W. Peterson, J.A. Rossin, G.W. Wagner, J. Phys. Chem. C, 116 (2012) 11606.

[36] G.W. Wagner, L.R. Procell, R.J. O'Connor, S. Munavalli, C.L. Carnes, P.N. Kapoor, K.J. Klabunde, J. Am. Chem. Soc., 123 (2001) 1636.

[37] K.R. Brown, D.G. Walter, M.J. Natan, Chemistry of Materials, 12 (2000) 306.

[38] S.J. Oldenburg, R.D. Averitt, S.L. Westcott, N.J. Halas, Chemical Physics Letters, 288 (1998) 243.

[39] R.G. Chaudhuri, S. Paria, Chem. Rev., 112 (2012) 2373.

[40] P. Patsalas, N. Kalfagiannis, S. Kassavetis, Mater., 8 (2015) 3128.

[41] U. Guler, A.V. Kildishev, A. Boltasseva, V.M. Shalaev, Faraday Discussions, 178 (2015) 71.

[42] D.L. Jiang, H.J. Zhao, Z.B. Jia, J.L. Cao, R. John, J. Photochem. Photobiol. A, 144 (2001) 197.

[43] H. Zhang, A.O. Govorov, J. Phys. Chem. C, 118 (2014) 7606.

[44] S.M. Edlou, J.C. Simons, OPTICAL AND ELECTRICAL-PROPERTIES OF REACTIVELY SPUTTERED TIN, ZRN, AND HFN THIN-FILMS, 1994.

[45] G.V. Naik, J.L. Schroeder, X.J. Ni, A.V. Kildishev, T.D. Sands, A. Boltasseva, Opt. Mater. Express, 2 (2012) 478.

[46] O. Stenzel, The Physics of Thin Films Optical Spectra, Springer-Verlag, Berlin, 2005.

[47] I. Milosev, H.H. Strehblow, M. Gaberscek, B. Navinsek, Surface and Interface Analysis, 24 (1996) 448

[48] S.A. Maier, Plasmonics: Fundamentals and Applications, Springer Science+Business Media LLC, New York, 2007.

[49] I. Milosev, H.H. Strehblow, B. Navinsek, Thin Solid Films, 303 (1997) 246.

[50] C. Gionco, A. Battiato, E. Vittone, M.C. Paganini, E. Giamello, Journal of Solid State Chemistry, 201 (2013) 222.

[51] A.O. Govorov, H.H. Richardson, Nano Today, 2 (2007) 30.

[52] G. Baffou, R. Quidant, C. Girard, Appl Phys Lett, 94 (2009).

[53] L.J. Brennan, F. Purcell-Milton, A.S. Salmeron, H. Zhang, A.O. Govorov, A.V. Fedorov, Y.K. Gun'ko, Nanoscale Res. Lett., 10 (2015) 1.

[54] I.N. Martyanov, K.J. Klabunde, Environ. Sci. Technol., 37 (2003) 3448.

[55] W. Stober, A. Fink, E. Bohn, J. Colloid Interface Sci., 26 (1968) 62.

[56] D.A. Panayotov, D.K. Paul, J.T. Yates, J. Phys. Chem. B, 107 (2003) 10571.

[57] G. Li, L. Lv, H.T. Fan, J.Y. Ma, Y.Q. Li, Y. Wan, X.S. Zhao, J. Colloid Interface Sci., 348 (2010) 342.

[58] M.A. Fox, Y.S. Kim, A.A. Abdelwahab, M. Dulay, Catalysis Letters, 5 (1990) 369.

[59] N. Soggiu, H. Cardy, J.L.H. Jiwan, I. Leray, J.P. Soumillion, S. Lacombe, Journal of Photochemistry and Photobiology a-Chemistry, 124 (1999) 1.

[60] E. Baciocchi, C. Crescenzi, O. Lanzalunga, Tetrahedron, 53 (1997) 4469.

[61] C. Ye, Y.B. Zhang, A.S. Ding, Y. Hu, H. Guo, Scientific Reports, 8 (2018).

[62] S. Oae, T. Takata, Y.H. Kim, Tetrahedron, 37 (1981) 37.

[63] T. Siefke, S. Kroker, K. Pfeiffer, O. Puffky, K. Dietrich, D. Franta, I. Ohlidal, A. Szeghalmi, E.B. Kley, A. Tunnermann, Adv. Opt. Mater., 4 (2016) 1780.

[64] I.H. Malitson, Journal of the Optical Society of America, 55 (1965) 1205.

[65] J.F. Moulder, W.F. Stickle, P.E. Sobol, K.D. Bomben, Handbook of X-Ray Photoelectron Spectroscopy, Perkin Elmer Corporation, Eden Prairie, MN, 1992.

[66] D. Panayotov, J.T. Yates, J. Phys. Chem. B, 107 (2003) 10560.

[67] T.L. Thompson, D.A. Panayotov, J.T. Yates, J. Phys. Chem. B, 108 (2004) 16825.

[68] D.B. Pedersen, S. Duncan, J. Phys. Chem. A, 109 (2005) 11172.

[69] E.Y. Santiago, L.V. Besteiro, X.T. Kong, M.A. Correa-Duarte, Z.M. Wang, A.O. Govorov, Acs Photonics, 7 (2020) 2807.

[70] M.A. Neouze, U. Schubert, Monatsh. Chem., 139 (2008) 183.

[71] L.D. Ellis, J. Ballesteros-Soberanas, D.K. Schwartz, J.W. Medlin, Applied Catalysis a-General, 571 (2019) 102.

[72] I. Rehor, V. Kubicek, J. Kotek, P. Hermann, J. Szakova, I. Lukes, Eur. J. Inorg. Chem., (2011) 1981.

[73] P.H. Mutin, V. Lafond, A.F. Popa, M. Granier, L. Markey, A. Dereux, Chemistry of Materials, 16 (2004) 5670.

[74] M. Tassi, A. Roevens, G. Reekmans, M. Vanhamel, V. Meynen, J. D'Haen, P. Adriaensens, R. Carleer, Adv. Powder Technol., 28 (2017) 236.

[75] J.B. Rivest, G. Li, I.D. Sharp, J.B. Neaton, D.J. Milliron, Journal of Physical Chemistry Letters, 5 (2014) 2450.

[76] R. Wick-Joliat, T. Musso, R.R. Prabhakar, J. Lockinger, S. Siol, W. Cui, L. Severy, T. Moehl, J. Suh, J. Hutter, M. Iannuzzi, S.D. Tilley, Energy Environ. Sci., 12 (2019) 1901.

[77] A.H. Jenkins, C.B. Musgrave, J.W. Medlin, Acs Applied Materials & Interfaces, 11 (2019) 41289.

[78] J. Ballesteros-Soberanas, L.D. Ellis, J.W. Medlin, ACS Catal., 9 (2019) 7808.

[79] M. Wagstaffe, A.G. Thomas, M.J. Jackman, M. Torres-Molina, K.L. Syres, K. Handrup, J. Phys. Chem. C, 120 (2016) 1693.

[80] I.A. Jankovic, Z.V. Saponjic, M.I. Comor, J.M. Nedeljlkovic, J. Phys. Chem. C, 113 (2009) 12645.

[81] T. Rajh, J.M. Nedeljkovic, L.X. Chen, O. Poluektov, M.C. Thurnauer, J. Phys. Chem. B, 103 (1999) 3515.

[82] G.W. Wagner, Q. Chen, Y. Wu, J. Phys. Chem. C, 112 (2008) 11901.

[83] Y. Qiu, F. Ouyang, Applied Surface Science, 403 (2017) 691.

[84] K. Shankar, J.I. Basham, N.K. Allam, O.K. Varghese, G.K. Mor, X.J. Feng, M. Paulose, J.A. Seabold, K.S. Choi, C.A. Grimes, J. Phys. Chem. C, 113 (2009) 6327.

[85] J. Zhang, Q. Xu, Z. Feng, M. Li, C. Li, Angew. Chem. Int. Ed., 47 (2008) 1766.

[86] C.C. Tsai, H.S. Teng, Chemistry of Materials, 18 (2006) 367.

[87] S.Y. Bae, M.D. Winemiller, J. Org. Chem., 78 (2013) 6457.